

## **General Disclaimer**

### **One or more of the Following Statements may affect this Document**

- This document has been reproduced from the best copy furnished by the organizational source. It is being released in the interest of making available as much information as possible.
- This document may contain data, which exceeds the sheet parameters. It was furnished in this condition by the organizational source and is the best copy available.
- This document may contain tone-on-tone or color graphs, charts and/or pictures, which have been reproduced in black and white.
- This document is paginated as submitted by the original source.
- Portions of this document are not fully legible due to the historical nature of some of the material. However, it is the best reproduction available from the original submission.

# NASA CR-175249

## RESEARCH AND DEVELOPMENT TECHNICAL REPORT

### V-BAND IMPATT TRANSMITTER

(NASA-CR-175249) V-BAND IMPATT TRANSMITTER  
Final Report, Aug. 1981 - Jun. 1983 (Hughes  
Aircraft Co.) 159 p HC A08/MF A01 CSCL 09A

N84-27976

Unclas  
G3/33 13982

HUGHES AIRCRAFT COMPANY  
Electron Dynamics Division  
3100 West Lomita Boulevard  
Torrance, California 90505

JUNE 1983



FINAL REPORT FOR PERIOD AUGUST 1981 - JUNE 1983

#### DISTRIBUTION STATEMENT

Distribution limited to U.S. Government Agencies only (Test and Evaluation),  
June 1983. Other requests for this document must be referred to NASA-  
Goddard Space Flight Center, Greenbelt, MD 20771, ATTN: Code 727.

PREPARED FOR:

NASA-GODDARD SPACE FLIGHT CENTER  
Greenbelt, MD 20771



output stage. Output power of 4 watts CW across a 2.5 GHz band centered at 60 GHz was achieved with an input power of 4 mW. Dynamic range of the amplifier chain is in excess of 7 dB. This marks the first time ever that high power double drift IMPATT diodes are successfully used in a broadband stable amplifier. Other achievements on the program included: (1) Development of a single diode one watt stable amplifier over a bandwidth greater than 2.5 GHz (2) Development of a high power (>1 watt) stable amplifier capable of operating in either the constant current or constant voltage mode and verification of the advantages of the latter mode of operation (3) A theoretical analysis, verified by experiment that defined the performance requirements of circulators/isolators for reflection amplifiers and (4) Development of a 10-channel modulator with built-in test equipment (BITE) specifically protective circuitry, failure monitoring and mode of failure indicated.

## TABLE OF CONTENTS

<u>Section</u>		<u>Page</u>
1.0	INTRODUCTION	1-1
2.0	DESIGN, PROCESSING, EVALUATION AND RELIABILITY OF SILICON IMPATTS.	2-1
2.1	Silicon Double-Drift IMPATT Doping Profile Design	2-1
2.2	Silicon Epitaxial Material Growth	2-8
2.3	Material Evaluation	2-13
2.4	Processing of Epitaxial Material Into IMPATT Diodes	2-15
2.4.1	Low-Temperature Diffusion	2-15
2.4.2	Substrate Thinning	2-19
2.4.3	Wafer Metallization	2-19
2.4.4	Etching of the Wafer into Pill Diodes	2-20
2.5	Diode Packaging	2-20
2.6	Thermal Analysis	2-24
2.7	Thermal Characterization	2-30
2.8	Silicon IMPATT Reliability	2-37
2.8.1	Step-Stress Testing	2-38
2.8.2	Constant-Stress Testing	2-39
3.0	COMPONENT TECHNOLOGY FOR IMPATT AMPLIFIERS	3-1
3.1	Coaxially-Coupled, Reduced-Height Waveguide Circuit	3-1
3.2	Ferrite Components for IMPATT Reflection Amplifiers	3-6
3.2.1	Effect of Finite Return Loss of a Circulator on an Injection Locked Oscillator	3-7
3.3	Hybrid Couplers	3-16
3.4	10-Channel Current Regulator	3-27
3.4.1	Protection Circuits	3-32
3.4.2	Monitor Circuits	3-35
3.5	Test Equipment	3-35
3.5.1	High Power Swept Frequency Source	3-35
3.5.2	Downconverter	3-39

## TABLE OF CONTENTS (CONTINUED)

<u>Section</u>	<u>Page</u>
4.0 SINGLE STAGE IMPATT AMPLIFIERS	4-1
4.1 Low Power IMPATT Amplifiers	4-5
4.2 Medium Power IMPATT Amplifiers	4-6
4.3 High-Power IMPATT Amplifiers	4-10
5.0 POWER COMBINER	5-1
6.0 TRANSMITTER PERFORMANCE	6-1
7.0 STUDY OF CONSTANT-VOLTAGE VERSUS CONSTANT-CURRENT IMPATT BIASING	7-1
8.0 SUMMARY AND RECOMMENDATIONS	8-1
8.1 Summary	8-1
8.2 Recommended Future Work	8-2
 <u>Addendum</u>	
PHASE CHARACTERIZATION OF THE V-BAND IMPATT TRANSMITTER	1

# LIST OF ILLUSTRATIONS

<u>Figure</u>		<u>Page</u>
1.0-1	V-band transmitter with the integral 10-channel current regulator.	1-3
1.0-2	A high power (>1 watt) stable IMPATT amplifier capable of operating in either the constant-voltage or constant-current mode by switching the bias supply into either state.	1-4
2.1-1	Uniformly-doped, symmetric double-drift doping profile and its DC electric field distribution.	2-4
2.1-2	DC E-field versus distance for V-band double-drift silicon IMPATT.	2-6
2.1-3	Small-signal RF parameters for V-band double-drift silicon IMPATT diodes.	2-7
2.2-1	Effects of doping profile on avalanche region width (shaded region in electric field profile).	2-9
2.2-2	Schematic diagram of horizontal silicon epitaxial reactor.	2-11
2.2-3	Details of gas flow controls for multilayer epitaxial reactor.	2-12
2.3-1	$N_D$ and $N_{eff}$ as determined by C-V profiling, for a C-band silicon double-drift IMPATT.	2-16
2.4-1	Schematic of diffusion furnace.	2-18
2.5-1	Sequence of fabrication for ceramic ring "mini-pill" package.	2-23
2.6-1	Thermal model for the pulsed silicon double-drift IMPATT.	2-27
2.6-2	Simplified thermal model used for the calculation of the CW thermal resistance of the 44 GHz silicon double-drift IMPATT.	2-29
2.6-3	CW thermal resistance versus junction diameter calculated for the thermal model of Figure 2.6-2.	2-31
2.7-1	Test setup for DC parameters required for the measurement of thermal resistance of an IMPATT diode	2-34

# LIST OF ILLUSTRATIONS (CONTINUED)

<u>Figure</u>		<u>Page</u>
2.7-2	Test setup for pulse parameters required for the measurement of thermal resistance of an IMPATT diode.	2-35
2.8-1	Combined histograms of step-stress test results.	2-40
2.8-2	Log-normal plots of cumulative failure distributions.	2-42
2.8-3	Estimated MTF vs junction temperature of silicon double-drift IMPATT diodes.	2-44
2.8-4	IMPATT diode life test station.	2-45
2.8-5	IMPATT diode life test station.	2-46
3.1-1	Scale drawing of the single-diode V-band free-running and injection-locked oscillator circuit.	3-3
3.1-2	Developmental version of the single-diode free-running and injection-locked oscillator circuit.	3-4
3.1-3	Exploded view of the developmental version of the single-diode free-running and injection-locked oscillator circuit.	
3.2-1	Configuration for a one-port reflection amplifier injection-locked oscillator working into a three-port circulator.	3-9
3.2-2	Diagrams showing the vector addition of the amplitude of the intended input signal $I$ and the constant-amplitude reflector $R \cdot O$ to produce the actual input signal amplitude $V$ .	3-11
3.2-3	Plots of the upper and lower limits of the required locking range for a reflection amplifier ILO as a function of the isolation of a power combiner hybrid.	3-12
3.2-4	Plots of the upper and lower limits of the phase error of a reflection amplifier due to isolation in a hybrid power combiner (a) 1 dB gain, (b) 10 dB gain.	3-14



## LIST OF ILLUSTRATIONS (CONTINUED)

<u>Figure</u>	<u>Page</u>
3.2-5      Power combining loss for a two-module power combiner versus phase mismatch of the two modules.	3-15
3.3-1      Schematic diagram of a two-module hybrid-coupled combiner.	3-17
3.3-2      Output characteristics of 3 dB hybrid-coupled combiner.	3-19
3.3-3      Power combining efficiency of 3 dB hybrid-coupled combiner.	
3.3-4      Two possible schemes utilizing 90-degree, short-slot hybrid couplers for module-level power combining a pair of reflection amplifier-modules.	3-25
3.3-5      Configuration for the module-level power combining of a pair of matched IMPATT reflection amplifier modules using a 180-degree hybrid coupler (Magic Tee) and a quarter-wave length of line.	3-28
3.3-6      Configuration for the module-level power combining of four matched IMPATT reflection amplifier modules using three 180-degree hybrid couplers (Magic Tees) and a quarter-wave length of line.	3-29
3.3-7      Power output versus frequency of the two-module module-level power combiner based upon the configuration shown in Figure 3.3-5.	3-30
3.3-8      Output power versus frequency of the four-module module-level power combiner which is being developed to form the output stage of the solid state V-band transmitter.	3-31
3.4-1      Schematic diagram of basic circuitry required to operate the LM 117 regulator IC in the constant-current mode.	3-32
3.4-2      Schematic drawing of the 10-channel current regulator for the transmitter.	3-34

# LIST OF ILLUSTRATIONS (CONTINUED)

<u>Figure</u>		<u>Page</u>
3.5-1	Block diagram of V-band waveguide amplifier RF test station not including provisions for phase measurements.	3-36
3.5-2	Multilevel sweep oscillator block diagram for IMPATT characterization.	3-38
3.5-3	Down converter for characterization of noise and spurious output.	3-40
4.0-1	Reflection amplifier modes of operation.	4-2
4.1.1	Response of low power 60 GHz wideband stable amplifier stage employing a single-drift silicon IMPATT diode.	4-7
4.1-2	Low power IMPATT stable amp, with double peak response.	4-8
4.1-3	Driver first stage.	4-9
4.2-1	Response of medium power (0.5 watt) 60 GHz wideband stable amplifier stage employing a double-drift silicon IMPATT diode.	4-11
4.3-1	Output response of a one watt V-band amplifier operating in the triggered oscillator mode.	4-13
5.0-1	Assembled V-band four module combiner using 3 Magic Tees.	5-3
5.0-2	Four-watt V-band transmitter response.	5-4
6.0-1	Block diagram of the six-stage V-band solid state transmitter.	6-2
6.0-2	V-band power combiner amp #1.	6-3
6.0-3	V-band power combiner amplifier #2.	6-4
6.0-4	V-band power combiner amplifier #3.	6-5
6.0-5	V-band power combiner amplifier #4.	6-6
6.0-6	V-band power combiner amp 1 and 2 two diode module.	6-7
6.0-7	V-band power combiner amplifier #3 and 4 two diode module.	6-8

# LIST OF ILLUSTRATIONS (CONTINUED)

<u>Figure</u>		<u>Page</u>
6.0-8	Four-watt V-band transmitter response.	6-9
6.0-9	Driver fifth-stage two diode power combiner.	6-11
6.0-10	Driver third stage.	6-12
6.0-11	Driver first stage.	6-14
6.0-12	Driver second stage.	6-15
6.0-13	Driver fourth stage.	6-16
6.0-14	V-band transmitter output.	6-18
6.0-15	V-band transmitter with 4 watt output power across a 2.5 GHz band, and 30 dB gain.	6-19
7.0-1	DC bias current versus RF input drive power for a constant-voltage biased V-band, stable, silicon double drift IMPATT amplifier stage.	7-2
7.0-2	Gain versus RF input drive power for three frequencies and for both constant-voltage (CV) and constant-current (CI) conditions of biasing for a V-band, stable, silicon double-drift IMPATT amplifier stage.	7-3
7.0-3	RF output power versus frequency $F_o$ -constant current 1 watt V-band stable amplifier.	7-4
7.0-4	Power output versus frequency for constant voltage 1 watt stable V-band amplifier.	7-6
7.0-5	A high power (>1 watt) stable IMPATT amplifier capable of operating in either the constant-voltage or constant-current mode by switching the bias supply into either states.	7-7
7.0-6	Constant-I, Constant-V Bias Regulator Schematic.	7-8

## 1.0 INTRODUCTION

This report describes the development of a six-stage wideband V-band solid state transmitter. This work was performed under an 18-month program funded jointly by NASA Goddard Space Flight Center and by USAF Space Division under Contract No. NAS5-26727. The duration of this program was from September 21, 1981, through March 21, 1983. Basic goals for this work were to develop driver stages for the transmitter to operate from the milliwatt power level; a 1.0-watt single-IMPATT device amplifier module; and a module-level power combining scheme utilizing four of these 1.0-watt modules. Also, these items were to be integrated to comprise a transmitter having 4.0-watts minimum output power and 30 dB minimum gain over the 59.0 to 61.5 GHz frequency band. An additional task for this program was to perform a study of constant-current versus constant-voltage biasing of a 1.0-watt stable IMPATT amplifier stage similar to the amplifier module developed for use in output stage of the transmitter.

The performance goals of the transmitter and the actual performance achieved under this program are shown in Table 1.0-1. The goals for the gain and bandwidth of the transmitter were met fully, and except for the insertion loss of, and a slight additional degradation caused by, the output isolator, the power output goal also was met.

All stages of this transmitter employ double-drift silicon IMPATT devices mounted on diamond heatsinking. The entire transmitter is fabricated from components of metallic waveguide, and each IMPATT device operates in a coaxially-coupled, reduced-height waveguide circuit. At the end of this development program, this transmitter was delivered to NASA Goddard. A photograph of the transmitter, including a ten-channel current regulator unit which allows operation of the transmitter from a single power supply, is shown in Figure 1.0-1. A 1.0-watt single-diode high-power amplifier capable of operating both in the constant voltage or current mode also was delivered to NASA. A photograph of the amplifier is shown in Figure 1.0-2.

Prior to the achievements made on this program, there were essentially no reported solid state V-band amplifiers above a few tenths of watts in power

TABLE 1.0-1  
COMPARISON OF PERFORMANCE GOAL AND ACHIEVED RESULT

Parameter	Goal	Achieved
<u>Transmitter</u>		
● Frequency	59.0 - 61.5 GHz	59.0 - 61.5 GHz
● Output Power	4 watts	4 watts (3.3 watt with output isolator)
● Gain	30 db $\pm$ 1.0 db	30 db $\pm$ 1.0 db
● Conversion Efficiency	4%	3.1%
● MTBF (Projected)	$>10^5$ hours	$>10^5$ hours
● Operating Temperature	+18°C to 32°C	+18°C to 32°C
<u>High Power Single diode Amplifier</u>		
● Frequency	59.0 - 61.5 GHz	59.0 - 61.5 GHz
● Output Power	1.0 watts	1.0 watts
● Gain	5 db $\pm$ 0.5 db	6.0 db $\pm$ 0.5 db
● Efficiency	5%	4.3% Power Added
● MTBF	$>10^5$ hours	$>10^5$ hours
● Operating Temperature	+18°C to 32°C	+18°C to 32°C

ORIGINAL PAGE 10  
OF POOR QUALITY

E4148

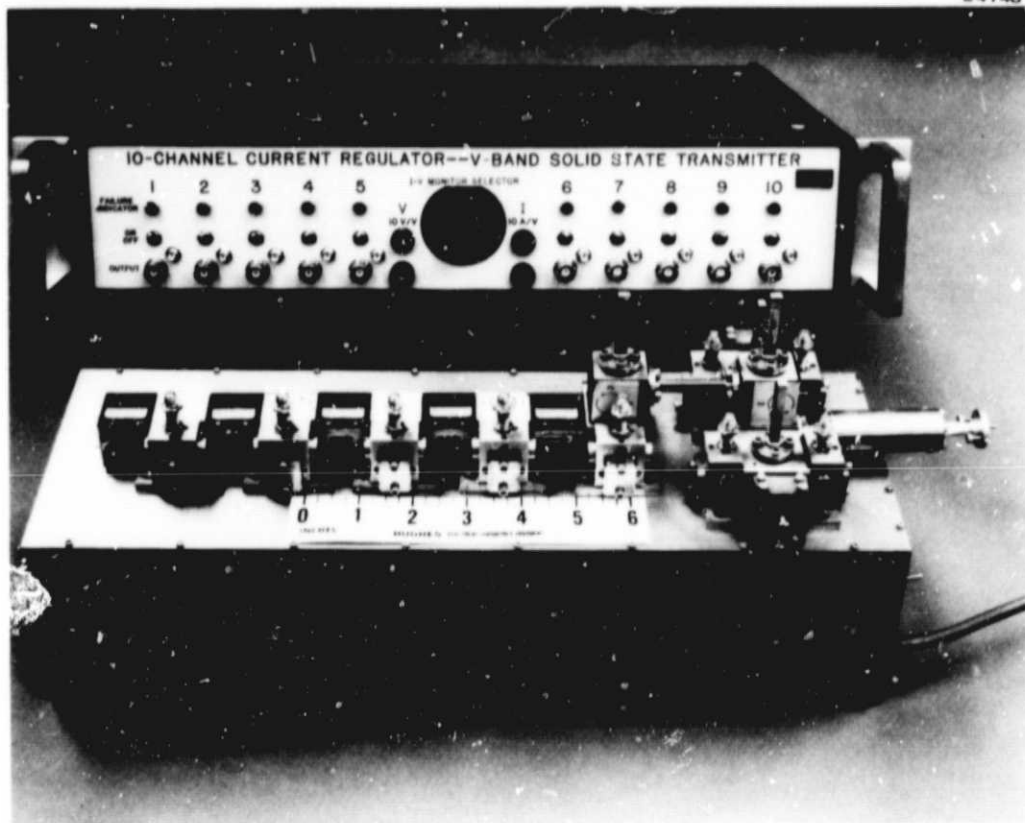


Figure 1.0-1 V-band transmitter with the integral 10-channel current regulator. The transmitter has 30 dB gain and produces 4 watts CW output power over a 2.5 GHz bandwidth.

ORIGINAL PAGE 15  
OF POOR QUALITY

ORIGINAL PAGE IS  
OF POOR QUALITY

E4149

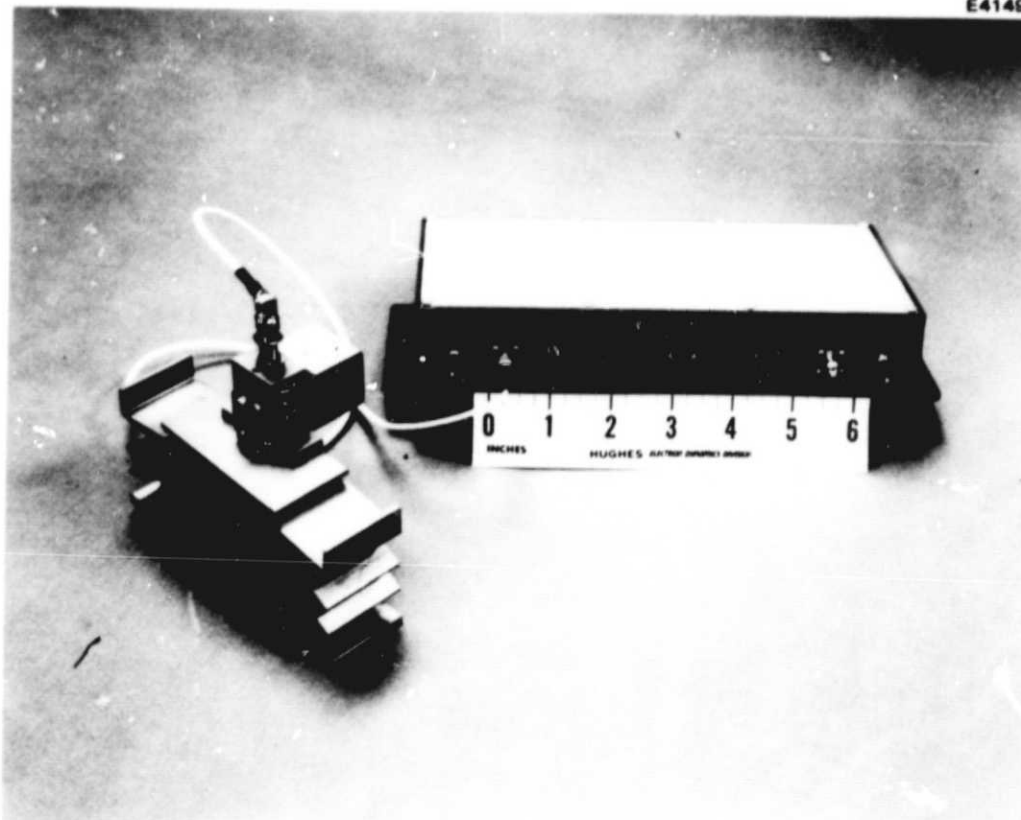


Figure 1.0-2 A high power ( $>1$  watt) stable IMPATT amplifier capable of operating in either the constant-voltage or constant-current mode by switching the bias supply into either state.

level and having a minimum of 2.5 GHz bandwidth. This transmitter represents a significant advancement of the state of the art in the area of wideband, solid state, power combiner millimeter-wave amplifiers, for which there is an incipient and growing demand. This demand is a result of the need for high-reliability, modern satellite communications systems.

The one requirement which made the development of this transmitter a particularly difficult and challenging one was the 2.5 GHz, or 4 percent, bandwidth specification. Experience from this work indicates that obtaining one-half to one-fourth or less of this bandwidth in all types of amplifier stages, (i.e., low-power driver stages, higher-power single-device stages and power combiner stages) can proceed in a relatively straightforward manner. Major difficulty was consistently encountered, however, in efforts to obtain useful operation of these amplifier stages over the full 2.5 GHz bandwidth. The primary problem was the onset of noise and/or spurious oscillations. Although these effects often appeared within only narrow regions within the 2.5 GHz band, their presence still cannot be tolerated. A major part of the effort on this program was concerned with the development of techniques to reduce or eliminate the occurrence of noise and spurious oscillations in these amplifier stages.

While the complete six-stage transmitter represents a significant advancement of the state of the art in this general area, a number of separate major accomplishments were made as part of the development of this unit:

1. A number of cascaded stable amplifier driver stages, each employing a double-drift silicon IMPATT, have been developed which amplify an input signal from the milliwatt level to several hundred milliwatts over the full 59.0 to 61.5 GHz band and with  $\pm 1$  dB gain flatness. Previously wide bandwidth can only be obtained from single drift devices.
2. A 1.0-watt stable reflection amplifier module employing a single double-drift silicon IMPATT on diamond heatsinking has been developed. This module has 3 to 4 dB gain over the 59.0 to 61.5 GHz frequency band and operates with a junction temperature rise of less than



225°C. This module serves as an intermediate driver stage in the transmitter. This same design also is used as a building block in the two-module and four-module module-level power combiner stages, which comprise the fifth and sixth stage of the transmitter, respectively.

3. Novel schemes for the module-level power combining of two and of four wideband one-port IMPATT reflection amplifier modules have been developed. These schemes are based upon the use of wideband matched Magic Tee hybrid couplers and a quarter-wave section of line. Short-slot hybrid couplers, widely used for the module-level power combining of one-port reflection IMPATT amplifier modules, have been demonstrated to have insufficient bandwidth for this wideband power combining application.
4. An item less directly related to the transmitter development effort is the study which was performed on the constant-voltage versus-constant-current biasing of a stable 1.0-watt amplifier module developed under this program. In this study it was found that for these V-band stable amplifiers employing silicon IMPATT devices the constant-voltage biasing mode offers essentially the same type of advantages as has been reported for the 8 GHz GaAs IMPATT amplifiers. However, for the 60 GHz silicon IMPATT amplifiers, the advantages are much smaller in magnitude that they are of little practical advantage. The explanation for this great difference in the magnitude of these advantages between the silicon devices at 60 GHz and of the GaAs devices at 8 GHz is probably related to the wide difference in the DC to RF conversion efficiency between the two devices, 5 to 6 percent for silicon at 60 GHz versus 18 to 20 percent for GaAs at 8 GHz.
5. The problem of the presence of noise and spurious oscillations in the output of the various types of amplifier stages, a common limitation in the development of wideband IMPATT amplifiers, was overcome by developing suitable RF circuits and by operating at sufficiently low gain per stage.

Sections of this report which follow describe in some detail the development work associated with these and with other accomplishments under this program. Sections 2.0 and 3.0 describe the technology of the components utilized within the various stages of the transmitter. One major such component is the V-band silicon double-drift IMPATT device mounted on diamond heatsinking. Section 2.0 deals with the technology of these devices. The remaining components utilized within the various stages of the transmitter are covered in Section 3.0. These components include the coaxially coupled, reduced-height waveguide circuit in which each IMPATT device on the transmitter operates; circulators which are, in fact, an integral part of the single-module IMPATT amplifier stages; and hybrid couplers which are the basis of module-level power combining schemes. Two types of hybrid couplers are discussed: the 90-degree short-slot hybrid coupler and the wideband matched Magic Tee 180-degree hybrid coupler. Both were studied extensively on this program in the effort on module level power combining, but, as will be explained in Section 4, only the Magic Tee coupler was successful in this application.

An integral part of the six-stage solid state V-band transmitter, which was developed under this program, is the ten-channel current regulator designed and fabricated as part of this program. This regulator unit allows operation of the transmitter from a single DC power supply. This regulator unit is shown in the photograph of the transmitter in Figure 1.0-1. The design of this regulator will be described also in Section 3.0.

Section 4.0 of this report describes the development of the single-IMPATT device amplifier stages which are used on the transmitter. These will include such stages ranging from the lowest power stage, which is driven from the milliwatt power level, through the 1.0-watt stable amplifier module which is used in the highest power single device stage, Stage 4, and which is used also as a building block in the two module-level power combiner stages of the transmitter, Stages 5 and 6. Section 5.0 of this report describes the development of the successful wideband module-level power combining scheme by which the 4-watt power output level has been achieved over the 59.0 to 61.5 GHz frequency range. This scheme is based upon the use of wideband matched Magic Tee hybrid couplers. The original approach taken on this program for module-level power combining was based upon the more common approach

utilizing 90-degree short-slot hybrid couplers. This original approach was not successful. The limitations encountered in this original approach will be described. Section 6.0 presents the performance of the complete six-stage solid state V-band transmitter. In Section 7.0 of this report will be presented the results of the study of constant-voltage versus constant-current biasing of a 1-watt stable V-band silicon IMPATT amplifier stage. Finally, a summary of work performed on this program and recommended future work will be presented in Section 8.0.

## 2.0 DESIGN, PROCESSING, EVALUATION AND RELIABILITY OF SILICON IMPATTs

Silicon IMPATT devices were used exclusively in all six stages of the V-band solid state transmitter developed under this program. These IMPATT devices are a fundamental component of the transmitter, and they played a key role toward achieving the final level of performance from the transmitter. However, minimal device development work was performed as part of the effort on this program, because the Statement of Work specified that existing state-of-the-art device technology was to be used in the development of the transmitter. In effect, this program was intended primarily to be one of circuit development. Nevertheless, the actual IMPATT devices used in the final transmitter configuration were all produced from new epitaxial material which was grown and processed entirely during this 18-month development program. This section of the report discusses the device design, the techniques for fabrication of the silicon IMPATT devices, methods of testing the devices and the results of reliability testing of these Hughes double-drift silicon IMPATTs.

### 2.1 SILICON DOUBLE-DRIFT IMPATT DOPING PROFILE DESIGN

Two basic categories of IMPATT diode doping profile designs are the single-drift and double-drift types. Nearly all of the millimeter-wave silicon IMPATT devices designed and fabricated at Hughes have been either single-drift or double-drift devices having flat (uniformly-doped) active regions. The flat profile has been used extensively primarily because it minimizes the complexity of growing the material in an epitaxial reactor.

Once the flat type of profile design is selected for the design of new IMPATT material, it remains to determine design values of the doping density and layer thickness for the single p or n epitaxial layer in single-drift devices, or for both the p and n layers in double-drift devices. There are many analytical approaches by which these design values may be derived for an IMPATT for a given application, such as frequency range, amplifier or oscillator operation, etc. Design approaches range from very complex to relatively simple, as from one based upon a large-signal computer simulation to one based upon simple transit-time considerations. Once these design values are determined, material may be grown, devices may be fabricated and evaluated

and iterations about the original design values may be made until acceptable device performance has been achieved.

Many past R&D programs concerning silicon IMPATT devices have been completed at Hughes. When work began on this program, there were already available at Hughes a wide variety of existing silicon IMPATT devices, both packaged and in chip form, ready for packaging to any desired specification. These included single-drift and double-drift devices of a range of breakdown voltages (i.e., devices of varying doping profiles), most of which were produced to uniform doping profile designs. Most devices were developed on one or more of these past R&D programs at Hughes in the area of V-band silicon IMPATT devices. In the development of the various IMPATT amplifier stages of the transmitter on this program, a wide variety of these existing IMPATT devices was evaluated for each stage to determine the optimum diode parameters for each stage. Effectively, then, the optimum doping profile for the IMPATT devices used in each stage of the transmitter was determined experimentally. Therefore, procedures for the analytical design of the doping profiles of IMPATTs will not be discussed in this section.

This section presents the experimentally selected doping profile and the results of a DC and small-signal analysis of the profiles will be shown. In fact, all of the IMPATT devices selected for operation in each of the six different stages of the transmitter, where these stages vary from the tens of milliwatts output power level in the first stage to the one-watt power level in the final three stages, are all fabricated from epitaxial materials of similar doping profiles. Only the diode area and perhaps the bonding strap configuration differ among some of the devices. This IMPATT material is of the double-drift doping profile design, and it was originally designed and produced for the higher power stages of the amplifier, in which it performed well. However, it was found that this material also performed better than any other material evaluated, including both single-drift and double-drift, in the lowest and medium power stages. The actual performance of this material in the various stages of the transmitter is discussed in Section 4.0 of this report.

The symmetric uniformly doped double-drift IMPATT structure consists of a  $p^+pnn^+$  multilayer doping profile shown schematically in Figure 2.1-1. Also shown in the figure is the form of the DC electric field at avalanche breakdown. The double-drift structure performs better for high-power applications than the more conventional  $p^+nn^+$  single-drift structure, because the RF susceptance per unit area is lower in the double-drift structure. This allows the use of larger area devices while maintaining good impedance matching to the circuit. It is believed that any improvement which might be realized by going to an asymmetrical double-drift design, which might compensate for the unequal ionization rates and drift velocities of electrons and holes, would not justify the effort. Uncertainties in dependence of the electron and hole ionization rate on the electric field and on temperature impose limitations on the accuracy of the analysis of the asymmetrical device, and complexity is added to the epitaxial growth process.

For the uniform, symmetric, double-drift device, only two parameters, doping density and epitaxial layer thickness, are required to specify the processing of the epitaxial material. Of course, the abruptness and quality of the  $p^+p$  and  $n^+n$  interfaces are critical. If these high-low contact junctions are excessively graded, a high parasitic series resistance results, reducing output power and efficiency.

The proper thickness of the epitaxial layer is critical for obtaining high-power operation from the device. The thickness of the p and n epitaxial layers should be such that the space charge region depletes just to the  $p^+p$  and  $nn^+$  interfaces under normal operating conditions of temperature and junction current density. For a layer which is too thick, the resulting undepleted region adds series resistance to the device. A layer which is too thin results in punch-through conditions, increasing the avalanche region width relative to the width of the total depletion layer. This effect lowers IMPATT efficiency.

In addition to a proper design of the junction doping profile for the IMPATT, various other factors are involved in specifying the fabrication of a high performance device. For example, the parasitic resistance of the substrate must be minimized both by minimizing the thickness of the substrate and by maximizing its conductivity. Also, the packaging of the device and the external

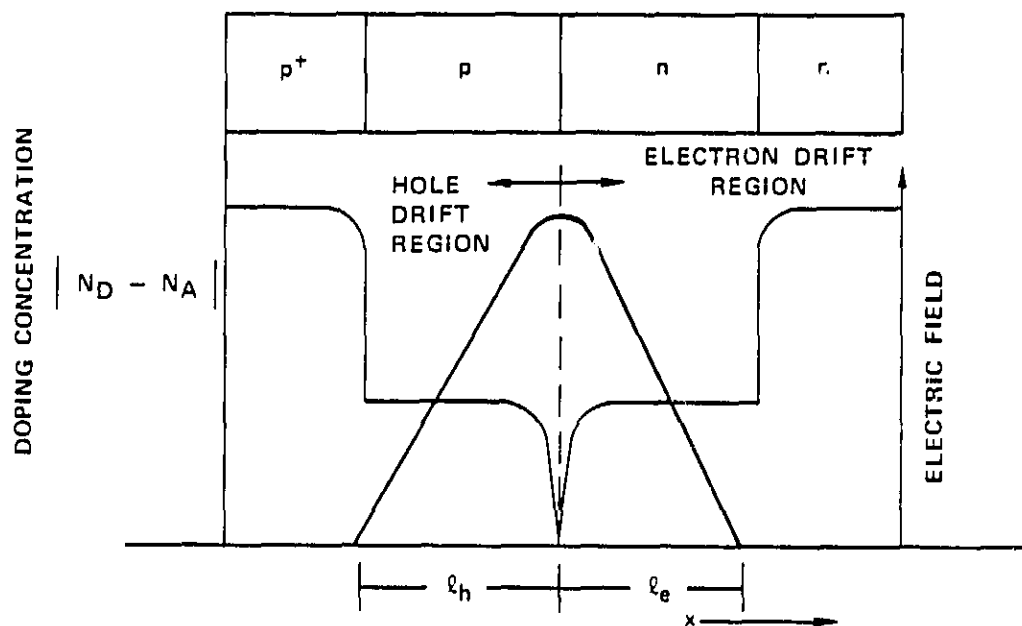


Figure 2.1-1 Uniformly-doped, symmetric double-drift doping profile and its DC electric field distribution.

circuit in which it is used directly influences the performance of the device. These items are discussed in later subsections.

The major parameters describing the wafer of silicon double-drift IMPATT material used in all stages of the V-band transmitter are listed in Table 2.1-1. A computer program developed at Hughes is used for the analysis and design of doping profiles of IMPATT diodes. This program calculates, for a specified doping profile which may be of arbitrary form, and for a specified current density and junction temperature, the one-dimensional DC electric field distribution within the junction under avalanche breakdown. Then, based on a small-signal analysis according to the Misawa<sup>1</sup> theory, the program calculates, as a function of frequency, the small-signal RF conductance and susceptance per unit area and the Q for that doping profile. The results for the doping profile of the device having the parameters listed in Table 2.1-1 appear in Figures 2.1-2 and 2.1-3, which are plots of the DC electric field and the small-signal admittance parameters, respectively. The small-signal admittance parameters are the conductance and susceptance per unit area and the small-signal Q, all three of which are plotted versus a common frequency axis. Note that the absolute value of the small-signal Q of the device versus frequency has its minimum near the desired 60 GHz center frequency of operation. Of course, these curves are somewhat dependent on the actual value of current density for which they are run, and the examples presented in Figures 2.1-2 and 2.1-3 are for only one such value. In the actual transmitter, these devices are operated at different current densities in different stages.

TABLE 2.1-1

PARAMETERS FOR THE UNIFORMLY-DOPED, SYMMETRIC  
DOUBLE-DRIFT REGION SILICON IMPATT MATERIAL USED  
ON THE V-BAND TRANSMITTER

Doping Density ( $N_D = N_A$ )	$8.0 \times 10^{16} \text{ cm}^{-3}$
Epitaxial Layer Thickness ( $A, D$ )	0.6 $\mu\text{m}$ each side
Breakdown Voltage (at 25°C)	21.8 V



$$T_j = \frac{\text{TEMP DEG C}}{250.00} \quad \frac{\text{CURR. DENS.}}{3.000\text{E}4 \text{ A/CM}^2} \quad \frac{\text{VOLTAGE}}{-3.500\text{E}1}$$

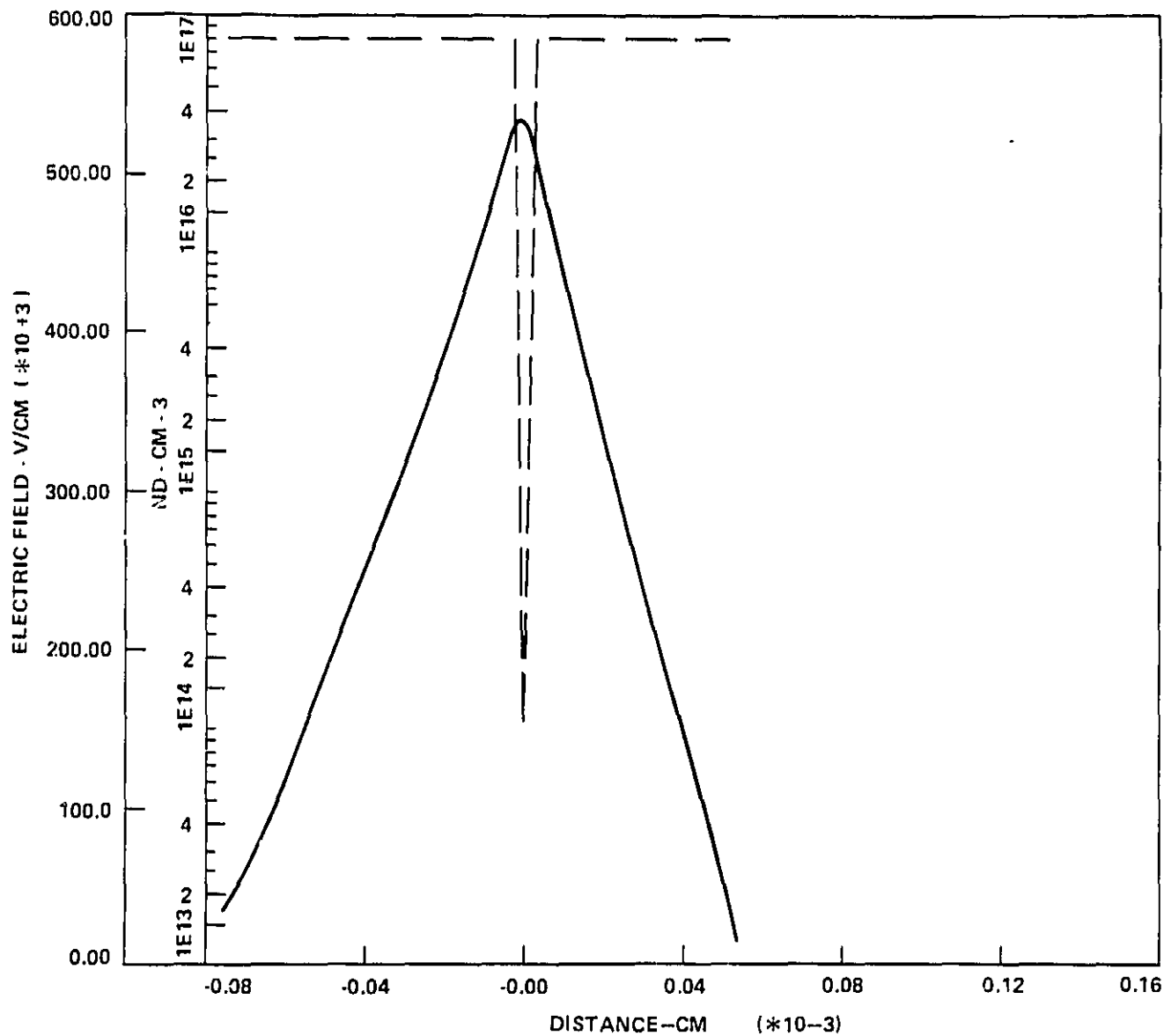


Figure 2.1-2 DC E-field versus distance for V-band double drift silicon IMPATT.

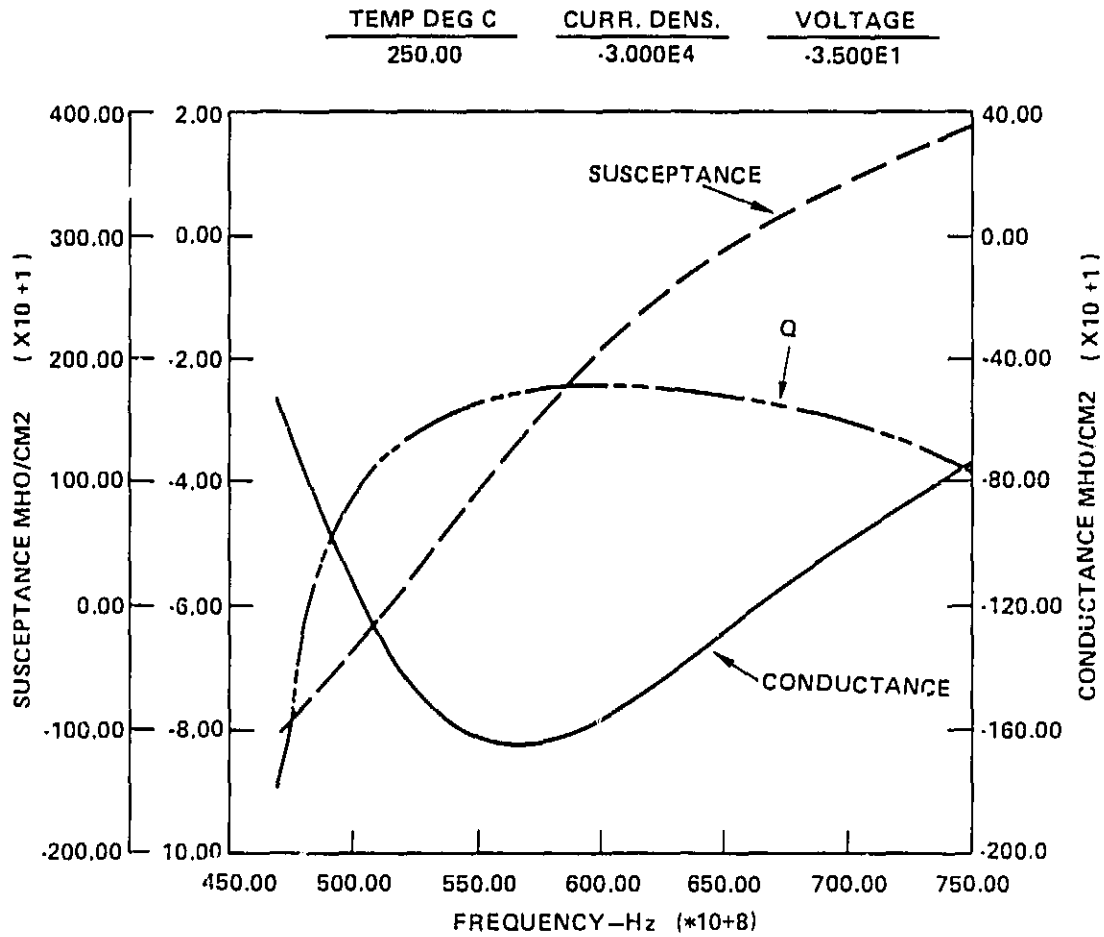


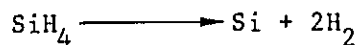
Figure 2.1-3 Small-signal RF parameters for V-band double drift silicon IMPATT diodes.

## 2.2 SILICON EPITAXIAL MATERIAL GROWTH

The growth of high-quality multilayer epitaxial silicon films on low resistivity substrates is the most critical step in the fabrication of high-performance millimeter-wave double-drift IMPATT diodes. The epitaxial growth process must be capable of producing a doping profile which closely approximates the desired design doping profiles for the p and n regions of the diode. The abruptness and quality of the  $p^+-p$ ,  $p-n$ , and  $n-n^+$  interfaces produced in the process must also be acceptable. If the high-low contact junctions are excessively graded, a high parasitic series resistance results which reduces output power and efficiency. In IMPATT diodes for millimeter-wave frequencies, where the overall junction thickness is relatively small, these contact regions are especially critical to the RF performance of the device.

Poor doping profile control can have several detrimental effects on the electric field and current densities of an IMPATT diode biased into avalanche breakdown. Some of these effects are illustrated in Figure 2.2-1. If the p- or n-region doping density is graded on either side of the metallurgical junction (b), the width of the avalanche region will increase. Small- and large-signal analyses of IMPATT operation have shown that, for a greater width of the avalanche region with respect to the total space-charge region width, the negative resistance of the device is reduced, as are the power and efficiency of the device. The avalanche region width also increases if a punch-through condition occurs (d). If the doping density is retrograded as shown in (e) or if there is any excess length of the high resistivity n or p-region (c), then the high parasitic resistance near the  $p^+p$  and/or  $nn^+$  interfaces will also reduce output power and efficiency. Therefore, the double-drift diode should have uniform and abrupt p and n doping profiles with thicknesses such that the space-charge region just depletes to the  $p^+p$  and  $nn^+$  interfaces under normal operating conditions (a).

The process which is used at Hughes for growing high-quality multi-layer epitaxial silicon material employs the pyrolysis of silane through the following simplified reaction:



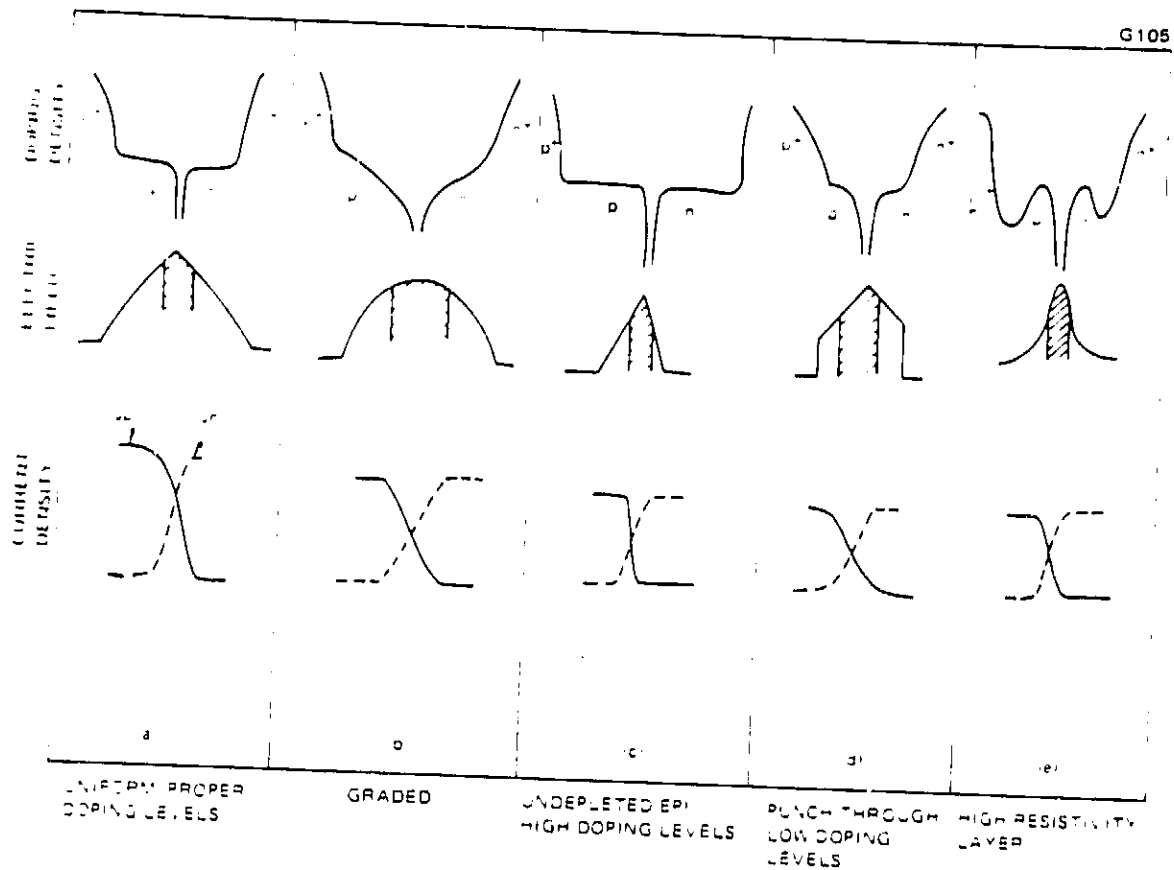


Figure 2.2-1 Effects of doping profile on avalanche region width (shaded region in electric field profile).

The epitaxial layers are grown on 1.25-inch-diameter, low-resistivity ( $<0.002 \Omega\text{-cm}$ ), arsenic-doped,  $\langle 111 \rangle$  oriented  $n^+$  silicon substrates. The above reaction is complete at temperatures above  $800^\circ\text{C}$ , and the growth temperature normally used is  $1000^\circ\text{C}$ . This temperature results in good thickness control and layer reproducibility while limiting the outdiffusion of dopant from the substrate.

The growth rate is normally  $0.5 \mu\text{m/min}$  and is relatively constant over a wide temperature range when using a silane concentration in hydrogen of 0.14 percent and a flow rate of 75 liters/min. The corresponding gas velocity is 20 cm/sec, which is relatively high. This growth scheme provides good thickness uniformity over the length of the susceptor. A 35 kW Radyne horizontal reactor has primarily been used for growing the silicon IMPATT diode material used on this R&D program. The reactor tube is water-cooled to minimize deposition on the tube and to effect a faster cooldown to minimize outdiffusion. The silicon substrate is gas-etched at  $1200^\circ\text{C}$  using HCl for about 10 minutes to remove all surface damage and impurities. The temperature is then reduced to  $1000^\circ\text{C}$  to initiate growth. Unless special precautions are taken, an epilayer grown using silane pyrolysis would have a thin, high resistivity layer at the substrate-epi ( $n^+-n$ ) interface, because the dopant does not sufficiently mix with the silane gas when first introduced into the system. To avoid this dip in the concentration profile the epitaxial reactor has a special modification to allow the gases to bypass the reactor tube to come to equilibrium in a mixing box for a period of time before being introduced into the reactor chamber.

The reactor also has capability for multilayer growth with various doping combinations. Cross-contamination of n and p dopants in the gas handling system is minimized by using separate doping systems. The reaction chamber is flushed with hydrogen between the growth of n- and p-type epitaxial layers to eliminate cross-contamination of dopants in the chamber. This is essential in the development of the double-drift diodes which require double epitaxial layers. A schematic of the horizontal epitaxial reactor is shown in Figure 2.2-2. The reactor has both p- and n-type doping manifolds with many refinements for good gas flow patterns and mixing. Details of the gas handling system designed to accomplish this are shown in Figure 2.2-3. At the end of the growth cycle, the reactor is immediately cooled to  $850^\circ\text{C}$ , and all residual silane gas is flushed out. The tube is then cooled slowly to room temperature.

G4514

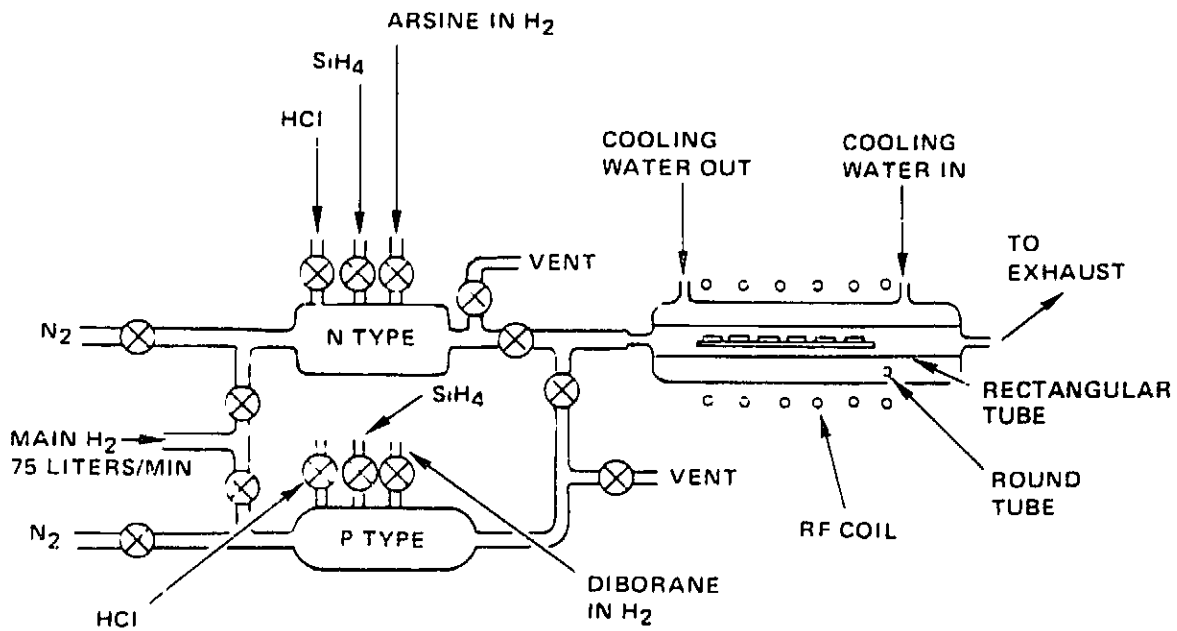


Figure 2.2-2 Schematic diagram of horizontal silicon epitaxial reactor.

G4515

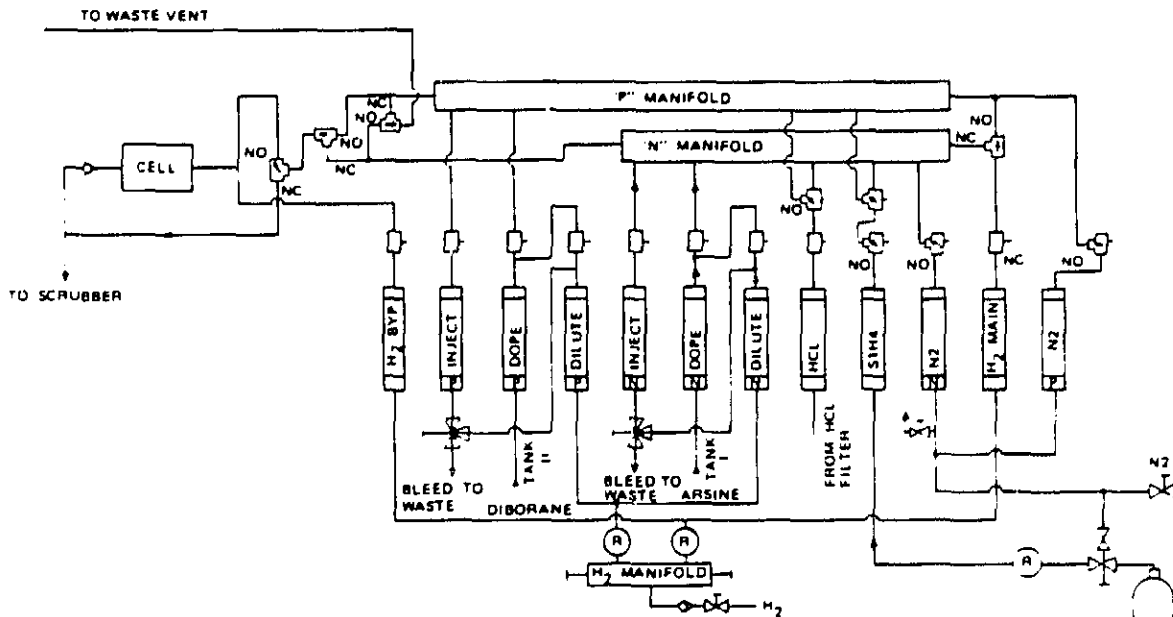


Figure 2.2-3 Details of gas flow controls for multilayer epitaxial reactor.

This procedure minimizes outdiffusion and at the same time avoids crystal damage due to thermal stress.

### 2.3 MATERIAL EVALUATION

While a great deal of effort at Hughes has gone into refining the designs of the horizontal and vertical epitaxial reactors and the procedures by which they are operated, there still exists some degree of uncontrollable run-to-run variation in the epitaxial material that is produced. Therefore, the doping profile of a sample of the epitaxial material produced from each reactor run must be measured by a suitable means to determine whether the material grown during that run conforms adequately to the original target doping profile. Based on the profiling information, a decision is made either that the material is acceptable, in which case the processing of that material into actual IMPATT devices for eventual RF evaluation will proceed, or that the material from the run is to be rejected and its further processing discontinued. In the latter case, the epitaxial material from that run is filed away for possible future use in meeting other requirements.

A suitable profiling technique is also required in a more fundamental application. Before a series of runs is made for growing material to a specific doping profile in the epitaxial reactor, several calibration runs are first made to determine nominal settings of various gas feed valves. In these calibration runs, generally single layers only, are grown of both p and n type doping. A reliable profiling technique is required for evaluating the material produced in these calibration runs.

The profiling technique used routinely for these applications is the standard capacitance versus voltage (C-V) method. On occasion, this measurement is supplemented by secondary ion mass spectroscopy (SIMS) analysis for selected wafers. In this section, only the E-V profiling method will be described.

The C-V profiling method used to determine the doping concentration  $N(x)$  as a function of distance,  $x$ , from a junction or a Schottky barrier contact, is based on the following equation for the doping concentration as a function of the capacitance measured as a function of the bias voltage  $V$ :



$$N(x) = \frac{C^3}{q A^2 \left( \frac{dC}{dV} \right)}^{-1} \quad (2.3-1)$$

and

$$x = \frac{\epsilon A}{C} \quad (2.3-2)$$

where

$C$  = depletion layer capacitance

$q$  = electron charge

$\epsilon$  = permittivity of the semiconductor material

$A$  = the diode junction area.

For a Schottky barrier contact, the doping concentration of the epitaxial layer is measured as a function of distance extending into the layer, while for a p-n junction, the measured data gives an effective doping concentration,  $N_{eff}$ , and a junction depth  $d$ , as follows

$$\frac{1}{N_{eff}} = \frac{1}{N_A} + \frac{1}{N_D} \quad (2.3-3)$$

and

$$d = X_A + X_D \quad (2.3-4)$$

where

$N_A$  = p-type doping concentration

$N_D$  = n-type doping concentration

$X_A$  = depletion width on the n-type side

$X_D$  = depletion width on the p-type side.

For measuring the doping profiles of a double-drift IMPATT diode, it is necessary to perform the C-V measurements on both Mesa and Schottky barrier diodes on a precisely step-etched wafer. Because the avalanche breakdown voltage is a strong function of carrier concentration, the penetration depth to which

the depletion layer can be extended into the epi layer is limited. The step etch procedure extends the range of profiling to cover the total layer thickness.

In actual measurements, the Mesa and Schottky barrier diodes are delineated on different sections of the wafer. On one section of the wafer, mesa diodes are used to measure the  $N_{eff}$  vs  $X$  of the entire p-n junction structure, while on the other section Schottky barrier diodes are made on the step-etched portion of the wafer to define the n-side profile of the junction. By knowing the n-side profile, the p-side profile can be reconstructed by using Equations (2.3-3) and (2.3-4).

Plots of  $N_D$  and  $N_{eff}$  versus thickness for a test wafer of the V-band silicon double-drift IMPATT as determined by an MDC automatic C-V profiler are shown in Figure 2.3-1. The thickness indicated for  $N_D$  is the measured thickness of the depleted material in the n-type region which is etched sufficiently to ensure punch-through of the depletion regions to the substrate. An allowance has been made to include the diffused  $p^+$  region, which is estimated to be about 0.15  $\mu$ m. The thickness corresponding to the  $N_{eff}$  profile is the total thickness of depleted material in both the p and n-type regions.

## 2.4 PROCESSING OF EPITAXIAL MATERIAL INTO IMPATT DIODES

When the profiling of one of the five wafers grown in the horizontal reactor indicates that the material is acceptable up to that point, the material can then be processed into individual pill diodes ready for packaging followed by RF evaluation. Normally, one wafer at a time is processed into pill diodes. There are four major steps involved in this process: (1) diffusion of the  $p^+$  contact, (2) thinning of the substrate material, (3) metallization of the wafer to form the electrical contacts and (4) etching the wafer into individual pill diodes by photolithography. These processing steps will be described in this section.

### 2.4.1 Low-Temperature Diffusion

Low-temperature boron diffusion is used to form a shallow  $p^+$  contact layer on the top surface of the epitaxial p-layer of the double epitaxial layer material. The high surface concentration resulting from this process minimizes

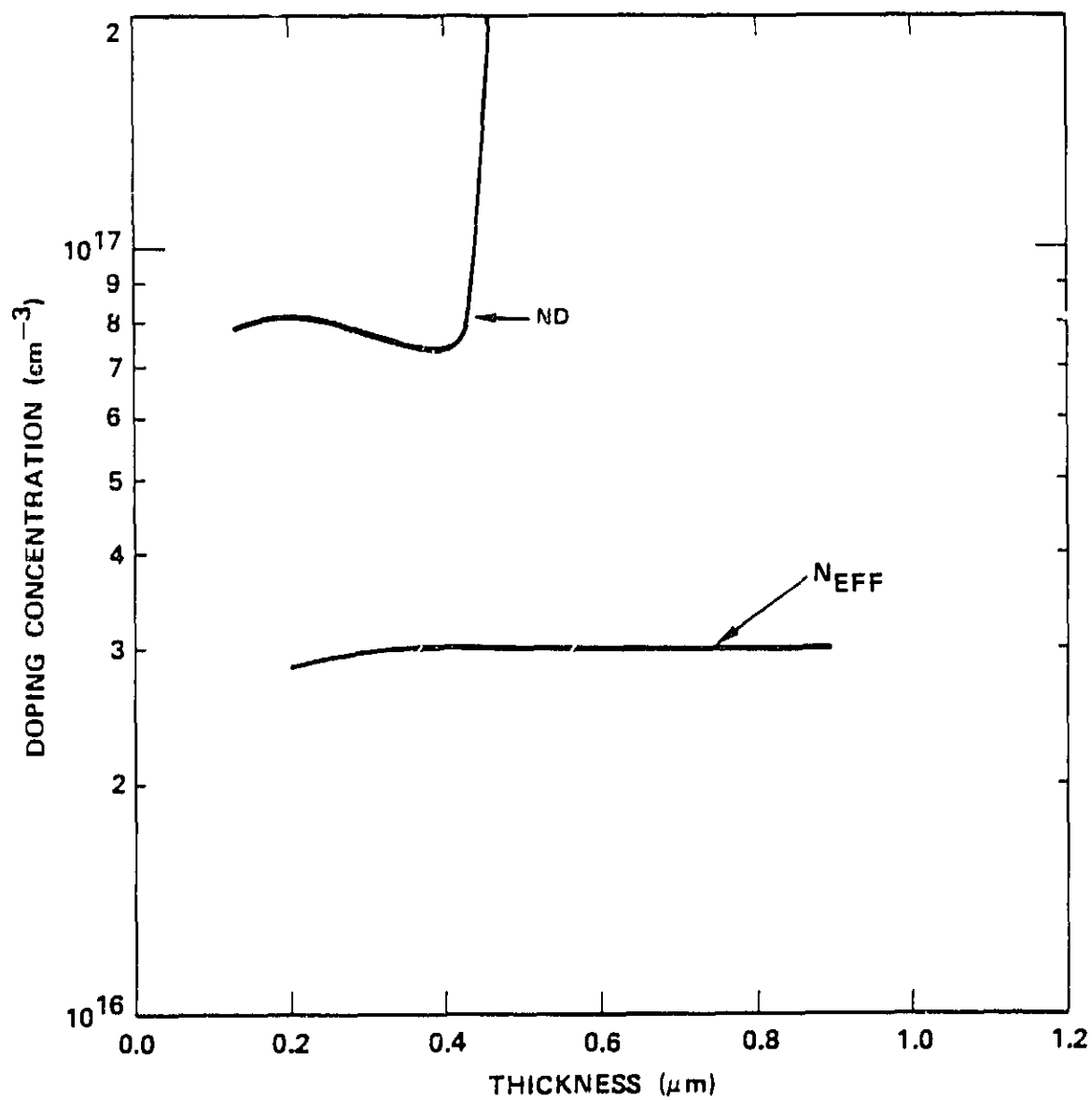


Figure 2.3-1  $N_D$  and  $N_{\text{eff}}$ , as determined by C-V profiling, for a Q-band silicon double-drift IMPATT.

the contact resistance between the epitaxial material and Cr-Pt-Au metallization applied later. To ensure that this diffusion does not degrade the epitaxial n-type doping profile, the diffusion temperature must be kept low. Typically,  $1000^{\circ}\text{C}$  is used. At this temperature both the boron diffusion into the p-layer and the outdiffusion of arsenic from the  $n^{+}$  substrate into the n-layer are relatively slow. Because of the difference in diffusion coefficients, the diffusion into the p-surface from a high-concentration boron source is typically more than five times faster than the outdiffusion of arsenic from the substrate. Therefore, for a nominal  $0.15\text{ }\mu\text{m}$   $p^{+}$  diffusion depth, the outdiffusion from the substrate is less than  $0.03\text{ }\mu\text{m}$ , which is acceptable for high performance IMPATT devices.

The diffusion depth can, if desired, be varied about this nominal  $0.15\text{ }\mu\text{m}$  value by varying the duration of the diffusion step. This capability provides a limited means for adjusting the thickness of the p-region layer after the epitaxial material is grown.

Diffusion at temperatures below  $1000^{\circ}\text{C}$  can also be used if desired. The  $1000^{\circ}\text{C}$  value was chosen primarily for ease of depth control. For higher temperatures, control is more difficult because the total time for a shallow diffusion is one or two minutes less. The time required for the temperature to stabilize is considerably longer than this, resulting in unwanted outdiffusion from the substrate.

In the diffusion furnaces used for silicon IMPATT processing and shown schematically in Figure 2.4-1, the boron p-type doping is done by bubbling nitrogen ( $N_g$ ) through a liquid source (trimethyl borate). The doping gas thus formed flows rapidly, creating a high surface concentration. The wafers are loaded onto a quartz boat and pushed into the furnace tube at a temperature rate of  $100^{\circ}\text{C}/\text{min}$  until the boat is situated in the  $1000^{\circ}\text{C}$  flat zone. A stabilization time of three minutes is allowed before the source is turned on. Nitrogen ( $N_B$ ) is the carrier gas and flows at a rate of about 2 liters/min. Before entering the tube, the nitrogen is mixed with doping gas and oxygen ( $O_B$ ). The oxygen slightly oxidizes the silicon surface to prevent boron glass, insoluble in most acids, from forming. Diffusion time for a junction depth of  $0.15\text{ }\mu\text{m}$  is 4 minutes.

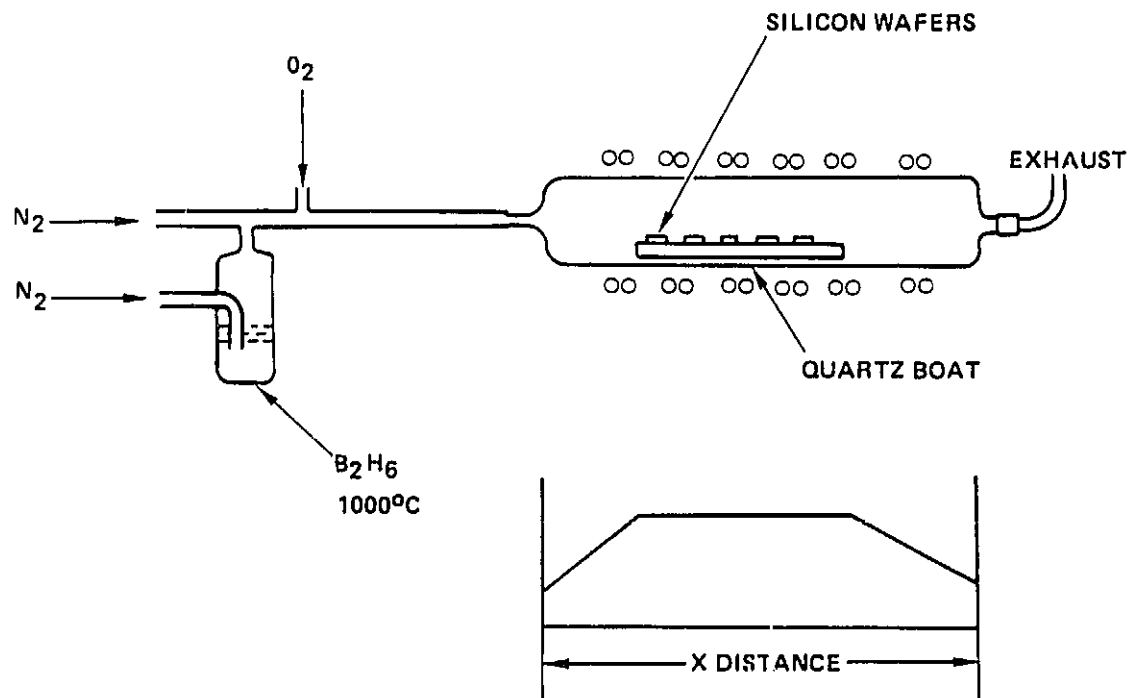


Figure 2.4-1 Schematic of diffusion furnace.

#### 2.4.2 Substrate Thinning

Following the diffusion of the  $p^+$  contact into the top surface of the p-type epitaxial layer of the double-drift IMPATT material wafer, the substrate material is thinned from its original thickness of 7 to 10 mils to a final thickness of 25 to 35  $\mu\text{m}$ , near the practical limit to which the wafer can be thinned. The purpose of this thinning is to reduce to as low a level as practical the parasitic series RF resistance and reactance associated with this excess substrate material.

In preparation for the thinning of this material, the wafer is mounted with wax on a sapphire disc. Protective wax is applied to the outer edge of the wafer to retain a thick silicon ring for handling the material after the wafer is thinned the desired amount. Thinning is accomplished chemically using a barrel etch process to achieve the final thickness 25 to 35  $\mu\text{m}$ . At thicknesses below about 35  $\mu\text{m}$ , silicon is transparent to light in the visible region. The thickness of thinned wafers is measured by optical transmission.

#### 2.4.3 Wafer Metallization

Following the process of thinning the substrate side of the wafer, the two sides of the wafer are metallized, providing an electrical contact surface as well as a surface which can take a high-quality thermocompression bond at the later diode packaging stage.

First, the  $p^+$  or epi side of the wafer is metallized. Three metal layers are then deposited onto the  $p^+$  side of the wafer of IMPATT material. A cryo-sublimation ion-pumped vacuum system with an electron beam heated source is used. The metallization for the  $p^+$  or front side of the wafer employs first a layer of chromium, then a layer of platinum and a layer of gold. Once the wafers are loaded into the chamber, this metallization sequence is fully automated. The gold layer is later built up by plating. This gold layer allows for a good thermocompression bond to the package heatsink at the later diode packaging stage.

The platinum layer acts as a diffusion barrier between the chrome and gold layers to improve device reliability. The major failure mechanism observed for these IMPATTs is the formation of a metallic gold spike which migrates through the metallization layers and through the silicon device material and eventually shorts out to the opposite metallized surface of the diode. The platinum barrier layer helps to reduce the rate at which this gold migration takes place.

Next the  $n^+$  or substrate side of the wafer of epitaxial material is metallized in a manner similar to the  $p^+$  side. However, the platinum barrier layer is not included on the  $n^+$  side to avoid the difficulty of chemically etching a pattern in the platinum when the individual pill diodes are formed.

To serve the high-performance CW application for which these V-band diodes are intended, diamond heatsinking is required. To obtain the maximum thermal advantage which diamond heatsinking offers, the diode must be bonded directly to the diamond with a minimum of intermediate metallization to minimize the thermal resistance of the device. Plated heatsink technology, therefore, does not apply to the high performance V-band IMPATTs developed for this program.

#### 2.4.4 Etching of the Wafer into Pill Diodes

The pill diodes are formed from the 1.25-inch-diameter wafer material by means of standard masking and chemical etching techniques. The masking and etching are done from the substrate side. For CW V-band silicon IMPATTs, pills of approximately 5 mils in diameter are formed. Later during packaging, the diode is trim-etched down to the final size required, which is nominally about 1.5 mils in diameter. From a single 1.25-inch diameter wafer, about 1500 pill diodes are obtained.

### 2.5 DIODE PACKAGING

The packaging of the IMPATT diode pill or chip is among several items which are critical for maximum performance from the IMPATT device. The package design is especially critical at millimeter-wave frequencies, where RF losses and parasitic capacitances and inductances must be kept very low. Attention

must be given in the package design that only materials having sufficiently low RF losses are used and that the package parasitic capacitances and inductances are kept down to acceptable levels. Hughes has developed standard package configurations for millimeter-wave IMPATTs. These standard packages have been used for nearly ten years in wide ranging applications and are well proven.

There are a number of qualities that a package for millimeter-wave IMPATT diodes must have to be useful in practical applications:

1. Low electrical parasitics or parasitics which are beneficial to the impedance matching of the diode to the circuit.
2. Low RF loss in the package materials.
3. Low thermal resistance between the diode chip and the remainder of the millimeter-wave circuit.
4. Mechanical ruggedness.
5. Hermetic sealing.
6. Reproducibility.

The millimeter-wave IMPATT diode package developed at Hughes and used for standard V-band devices meets all of these requirements. This package employs diamond heatsinking for its high thermal conductivity. An alternative low thermal resistance heatsinking technique of the pill diode bonded to a metalized diamond heatsink is the multi-mesa geometry, silver-plated heatsink technology. This method has been commonly used for GaAs IMPATTs at Hughes, as well as at other laboratories. However, for high-performance CW IMPATT devices, the diode pill individually bonded to diamond heatsinking has the advantage of lower thermal resistance. Also, more efficient use of epitaxial wafer area is realized, as many times more devices can be obtained from a



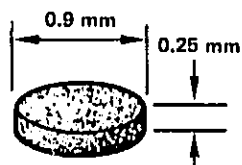
given area of wafer with the pill-on-diamond technique than with the plated heatsink technology.

In practice, realizing the potentially low thermal resistance of a diamond heatsink depends on the diamond metallization. A high temperature sputtering process has been developed using a Cr-Pt-Au metallization. The method involves the use of a high temperature sputtering procedure during which the diamond is first heated in vacuum before the Cr-Pt-Au layers are sputtered on in the same vacuum system. The Cr is used as a contact metal because of its relatively good match in lattice constant with diamond. The close match in lattice constant is believed to result in a metallic interface layer with optimum thermal transfer properties.

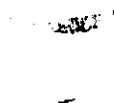
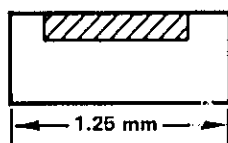
The assembly steps for the standard Hughes millimeter-wave IMPATT package are shown in Figure 2.5-1 and are described as follows:

1. A metallized Type IIa diamond disc 0.9 mm in diameter by 0.25 mm thick is hot-pressed flush into a gold plated copper disc 1.25 mm in diameter by 0.5 mm thick. This copper disc is of the standard size used for most applications. However, for special requirements, the package can be built up on any larger size gold-plated copper heatsink configuration as well.
2. The diode mesa is thermo-compression bonded to the center of the imbedded metallized diamond. Hughes has developed techniques for bonding small-diameter diodes ( 0.075 mm) onto both copper and diamond heatsinks using an in-house-developed thermo-compression bonder. The diodes are approximately 0.01 to 0.025 mm in thickness. The uniformity and reproducibility of the bonding have been excellent.
3. A 0.90 mm O.D. alumina insulating ring metallized top and bottom is soldered to the heatsink base concentric to the diode diameter. The capacitance of this ceramic ring is 0.19 pf. Alternatively, quartz rings can be used for their lower capacitance. Both were evaluated on this program, and the ceramic ring package produced best results for all stages of the amplifier.

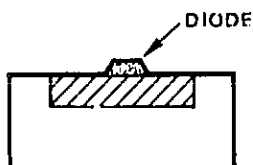
1. METALLIZE (Cr-Pt-Au)  
TYPE IIA DIAMOND



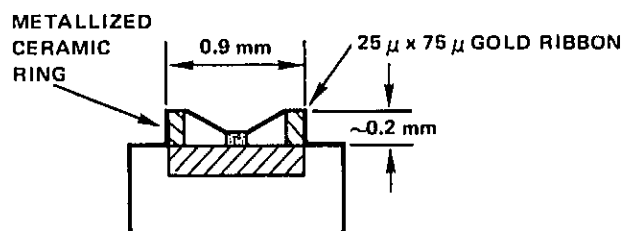
2. PRESS DIAMOND INTO  
COPPER HEATSINK



3. T.C. OR ULTRASONIC  
BOND DIODE ON DIAMOND



4. SOLDER CERAMIC RING  
AND RIBBON BOND --  
THEN TRIM-ETCH



5. SOLDER PACKAGE CAP

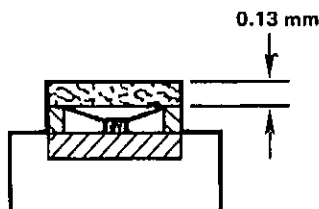


Figure 2.5-1 Sequence of fabrication for ceramic ring  
"mini-pill" package.

4. A gold ribbon 0.075 mm by 0.025 mm in cross-section is thermo-sonic bonded from the back of the diode to the top of the insulating ring. Optionally, 1/2, 1- 1/2, 2 or even 3 such ribbons can be used to vary the lead inductance as an aid in impedance matching of the diode to the external circuit. Generally, the best ribbon configuration for a given amplifier application is determined experimentally in actual RF evaluation of the devices.
5. The diode is chemically trim-etched to reduce the diameter to the desired final value. This process is monitored by measuring the zero-bias capacitance of the diode, which is a function of the diode cross-sectional area.
6. The assembly is baked to remove any volatile contaminants while a gold-plated copper lid is soldered in an inert atmosphere onto the ceramic ring insulator, completing the hermetically sealed package.

## 2.6 THERMAL ANALYSIS

Thermal analysis of the IMPATT is a major part of the IMPATT design process. The thermal analysis is required to estimate tradeoffs between the lifetime of the IMPATT device and the RF output power which the IMPATT device can deliver. An increase in the bias power to a given IMPATT device will, in general, increase its RF output power. The increase in bias power will also cause the IMPATT junction temperature to rise and consequently will result in a decrease in the mean-time-to-failure (MTTF) of the device.

A thermal analysis of IMPATTs normally involves determining the thermal resistance  $\theta$  of the IMPATT for the desired device geometry and mode of operation, i.e., CW or pulsed at some duty cycle and prf. The present program is limited to CW operation only. Thermal resistance of an IMPATT is defined as the power dissipated in the junction divided into the junction temperature rise over ambient:

$$\theta = \frac{\Delta T_J}{P_{\text{diss}}} \quad (2.6-1)$$

While the thermal resistance is generally assumed to be a constant independent of temperature, this is not exactly true, as the thermal properties, such as heat conductivity, of many materials are temperature dependent.

A few basic expressions related to the thermal resistance of the IMPATT will be listed here. The device is assumed to be operated in the free-running oscillator mode. The RF output power generated by the IMPATT ( $P_{RF}$ ), the bias power ( $P_{bias}$ ), and the power dissipated as heat in the IMPATT ( $P_{diss}$ ), are related as follows:

$$P_{bias} = P_{RF} + P_{diss} \quad (2.6-2a)$$

$$P_{RF} = \eta P_{bias} \quad (2.6-2b)$$

$$P_{diss} = (1-\eta) P_{bias} \quad (2.6-2c)$$

$$P_{RF} = \frac{\eta}{1-\eta} P_{diss} \quad (2.6-2d)$$

where  $\eta$  is the conversion efficiency of the IMPATT. From Equation (2.6-1).

$$P_{diss} = \frac{\Delta T_J}{\theta_{JA}} \quad (2.6-3)$$

then the RF power generated by the IMPATT can be expressed as

$$P_{RF} = \frac{\eta}{1-\eta} \cdot \frac{\Delta T_J}{\theta_{JA}} \quad (2.6-4)$$

Normally, a maximum allowable value for  $T_j$  for a given application is determined by reliability lifetime requirements of the IMPATT as discussed in Section 2.8 of this report. Therefore, the quantity

$$\frac{\rho}{1-\rho} = \frac{1}{\eta} \quad (2.6-5)$$

must be maximized to maximize the RF output power from a given device with  $T_j$  fixed. For a given lot of epitaxial material, the parameter  $\rho$  depends primarily upon the device area and the operating current density.  $\eta$  depends upon geometry as well as area. For a given geometry, such as the circular disc,  $\eta$  depends upon area. Determining the optimum values of device area and current density which result in a maximum for Expression (2.6-5) generally cannot be done on a theoretical basis only. It involves a careful laboratory evaluation for a given type of epitaxial material.

Only the circular disc geometry of the IMPATT is proposed for this program. The circular disc IMPATT mounted on diamond heatsinking is relatively straightforward to fabricate in a routine manner. It is highly efficient in its use of a given area of IMPATT wafer material, and it is a relatively low thermal resistance configuration. In this section, the thermal resistance of the V-band silicon double-drift IMPATT diode is calculated as a function of the diameter of the IMPATT for the cases of both copper and diamond heatsinks.

The thermal model that closely represents the actual V-band silicon IMPATT device of circular geometry is shown in Figure 2.6-1. A silicon diode disc of diameter  $D$  is bonded junction side down to a semi-infinite heatsink slab of either copper or diamond. The heatsink has a gold bonding layer and the diode has three metal layers, Cr over the Si, Pt over the Cr, and Au of 0.7  $\mu\text{m}$  thickness over the Pt. These metal layers are standard for Hughes millimeter-wave silicon IMPATT diodes. The thickness of the p and n type silicon layers of the diode is about 0.8  $\mu\text{m}$  for the 44 GHz silicon IMPATT as determined from the IMPATT doping profile design presented in Section 2.1.

It is very difficult to make exact CW thermal resistance calculations based on the model of Figure 2.6-1. Several approximations will be made in the

G9527

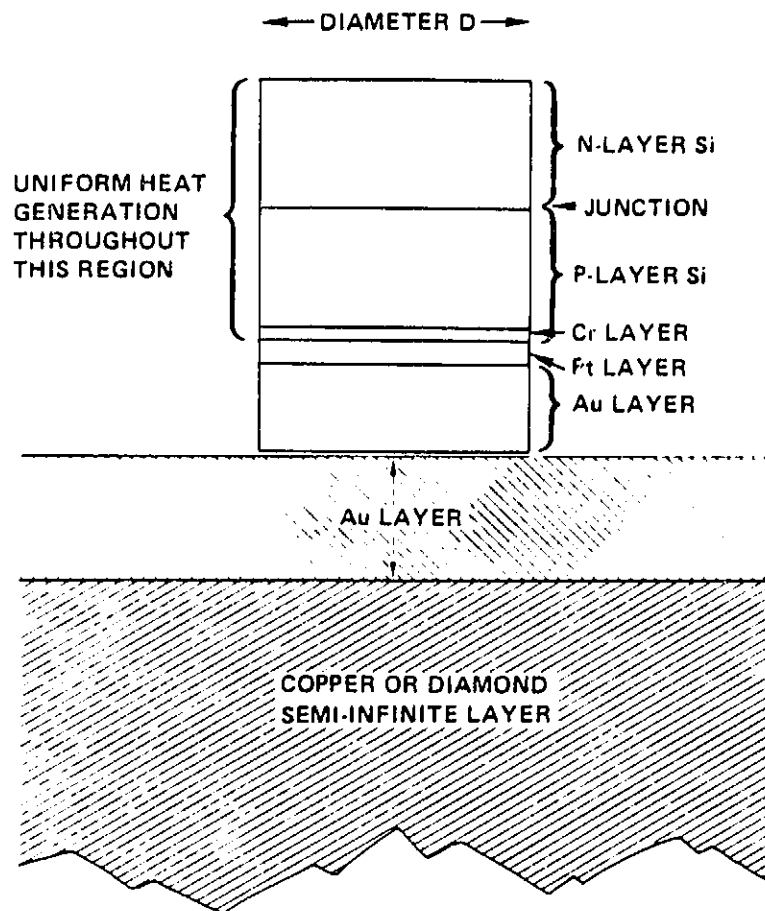


Figure 2.6-1 Thermal model for the pulsed silicon double-drift IMPATT.

model to simplify the calculation of thermal resistance. The (approximately) uniform generation which takes place throughout the volume of the p and n regions of the diode will be approximated by a surface of uniform heat flux, and that surface will be located at the p-n junction. Analysis indicates that this is a good approximation of the calculation of the thermal resistance of a symmetric double-drift device. No heat flows through the top or n-layer of the IMPATT for this approximation.

Another approximation which is made in the model of Figure 2.6-1 concerns the distribution of heat flow through the p-layer and through the metallization layers of the IMPATT. This will be taken into account by treating the layer of Si and the three metal layers, all of diameter D, as having uniform heat flow. These layers will be treated as simple series-connected thermal resistances each of whose contribution to the total CW thermal resistance of the IMPATT is

$$r_i = \frac{t_i}{A_i k_i} \quad (2.6-6)$$

where  $t_i$  is the thickness of layer  $i$ ,  $A_i$  is its area, and  $k_i$  is the thermal conductivity of the material of that layer. Figure 2.6-2 illustrates the simplified thermal model used for calculation of the thermal resistance of the IMPATT according to these approximations.

The calculation of the thermal resistance for the first part of the model in Figure 2.6-2 is done according to the expression for the spreading resistance for a circular disc uniform heat source on a two-layer semi-infinite heatsink as given by K. Board.<sup>2</sup> The thermal resistance for this configuration is given by the expression

$$\theta = \frac{1}{\pi K_1 R} \int_0^\infty \frac{1 + p \exp(-2uH)}{1 - p \exp(-2uH)} J_1(u) \frac{du}{u} \quad (2.6-7)$$

Where  $H = h/R$ ,  $p = (k_1 - k_2)/(k_1 + k_2)$ , and  $k_1$  and  $k_2$  are the thermal conductivities of the upper and lower heatsink material, respectively.  $h$  is the thickness of the upper layer of the two-layer, semi-infinite heatsink, and  $R$  is the radius of the heat source. Where the thickness of the top layer of the

0.9528

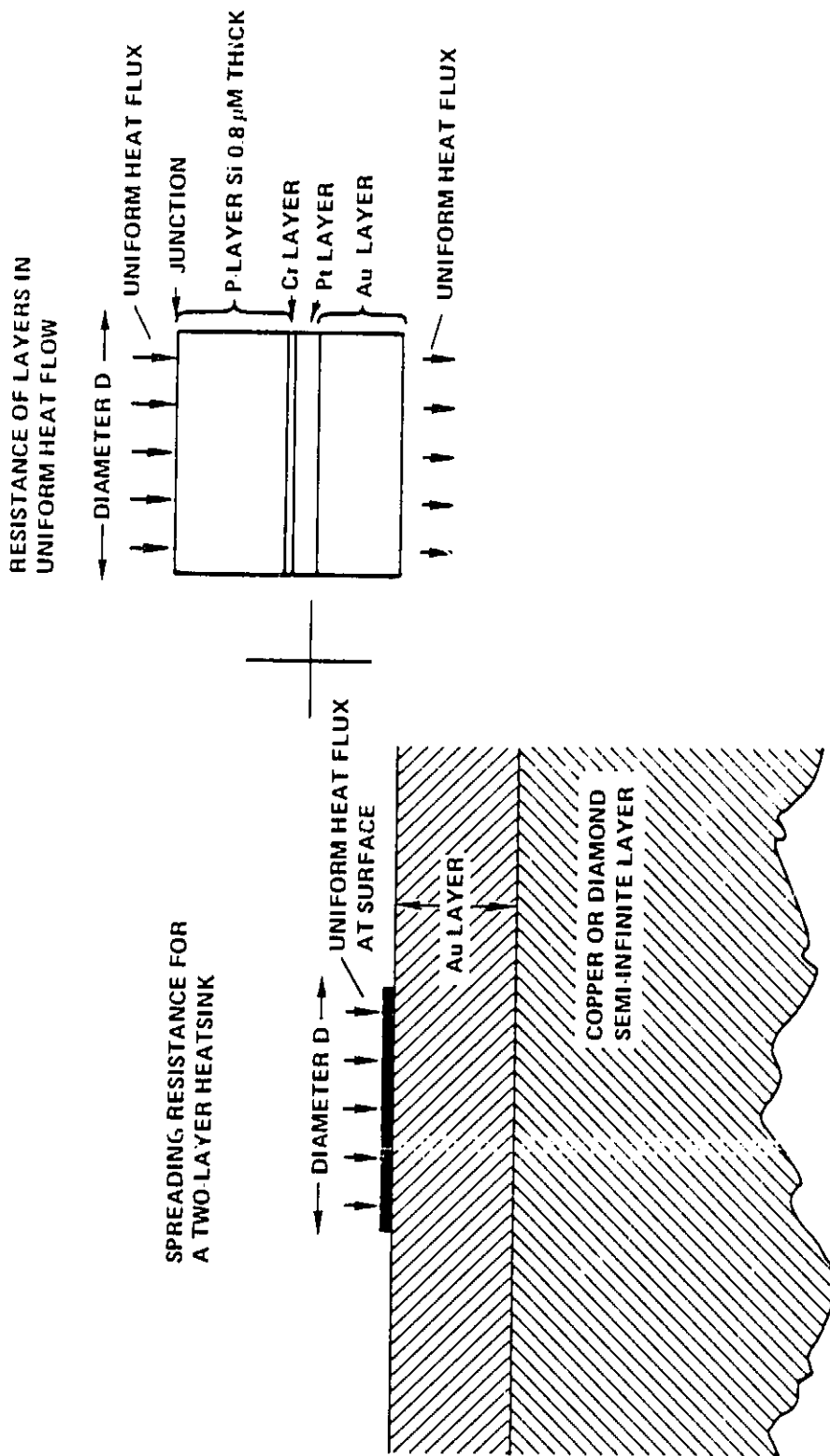


Figure 2.6-2 Simplified thermal model used for the calculation of the CW thermal resistance of the 44 GHz silicon double-drift IMPATT. The total thermal resistance is taken as the sum of that of the two separated configurations shown.



two-layer, semi-infinite heatsink is zero, the thermal spreading resistance for this configuration is simply,

$$\theta = \frac{1}{\pi kR} \quad (2.6-8)$$

As previously explained for calculation of the IMPATT thermal resistance, the approximation is made that the thermal resistance of the four layers of diameter D beneath the junction are in uniform heat flow and that their individual thermal resistances, given by Equation 2.6-6, are simply added to the spreading resistance for the disc on the two-layer heatsink.

The results of these calculations are shown in Figure 2.6-3 where the thermal resistance of a circular IMPATT is plotted versus junction diameter for the cases of a copper and a diamond heatsink for the IMPATT model shown in Figure 2.6-2. Also plotted in Figure 2.6-3 for a copper and a diamond heatsink are the contributions of the spreading resistance of a single material semi-infinite heatsink only. The contributions from the Si and metallic disc layers of diameter D and the contribution of the gold bonding layer of the semi-infinite heatsink are excluded. These calculations indicate that for a device of 65  $\mu\text{m}$  diameter, for example, these layers account for 34 percent of the total 16.8°C/watt thermal resistance of the device for the diamond heatsink case. The approximately 2-to-1 reduction in the CW thermal resistance for the case of diamond heatsinking over copper heatsinking is indicated in Figure 2.6-3.

The results of the thermal resistance calculations for copper heatsinking are included as a reference. However, copper heatsinking was not used in this amplifier development program because of its much higher thermal resistance over diamond heatsinking. The method used for the actual laboratory measurement of the CW thermal resistance of an IMPATT is described in Section 2.7.

## 2.7 THERMAL CHARACTERIZATION

Measurement of the thermal resistance of an IMPATT is important in device and circuit development because it is used in estimating the operating junction temperature of the diode. The junction temperature determines the MTF of

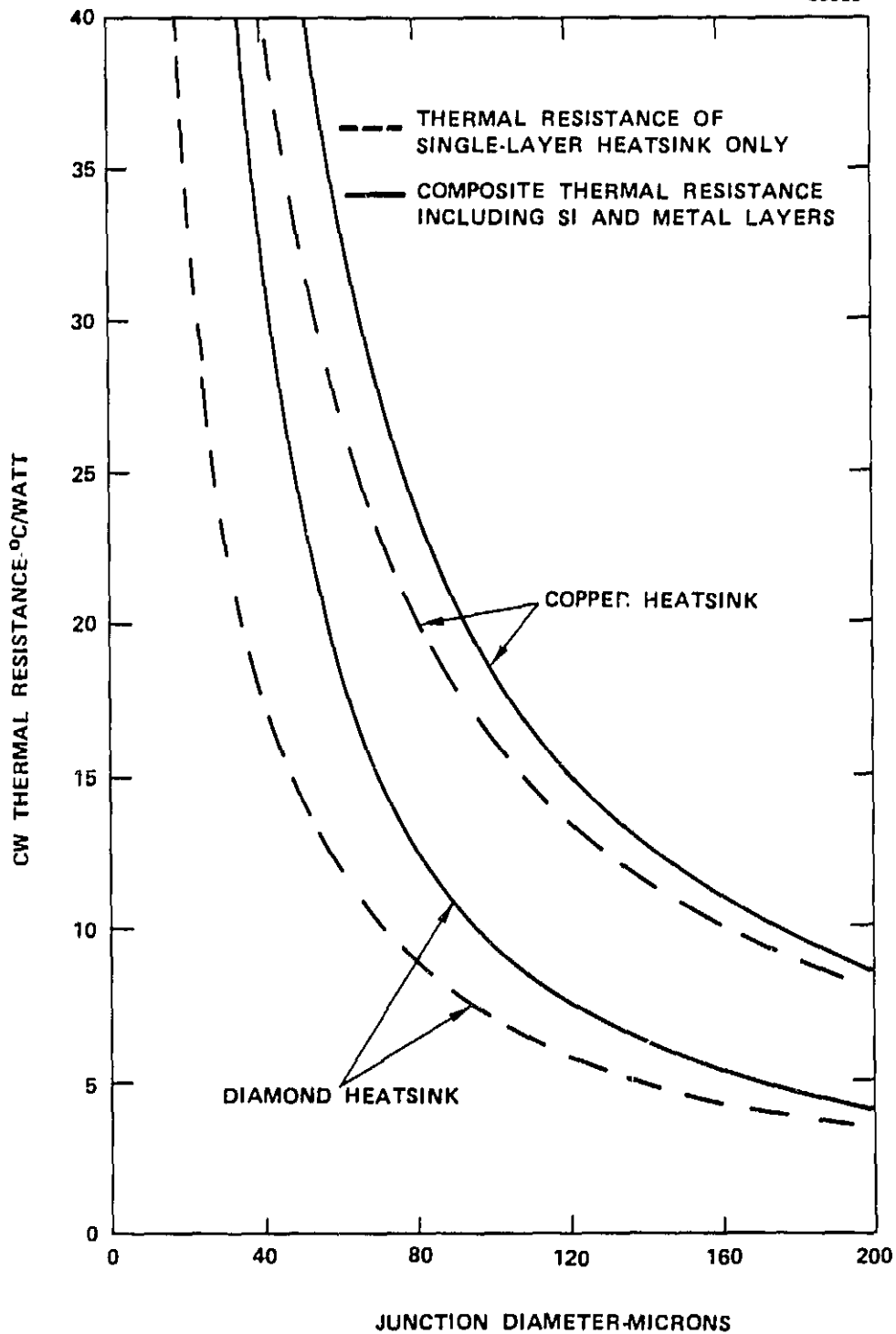


Figure 2.6-3 CW thermal resistance versus junction diameter calculated for the thermal model of Figure 2.6-2. Results for a copper heatsink and for a diamond heatsink are shown.

the device. The thermal resistance of the device also is used as an indicator of the quality of the bonding of the diode to the heatsink.

The technique for the measurement of thermal resistance of silicon IMPATT devices, which has been routine at Hughes for about 10 years, takes advantage of the current-voltage (I-V) characteristic of an IMPATT diode in avalanche breakdown and of the temperature dependence of this characteristic. In the absence of RF power generated by the device, three parameters in general completely describe the I-V characteristic of the IMPATT: voltage (V), current (I) and junction temperature (T). For a given IMPATT there is an associated functional relationship between these three variables,

$$f(V, I, T) = 0 \quad (2.7-1)$$

In the thermal resistance measurement method which will be described, this functional relationship is approximated by a linearization about some nominal operating point which will be called point 1. This linear relationship can be written as follows:

$$V_2 = V_1 + \alpha (T_2 - T_1) + R (I_2 - I_1) \quad (2.7-2)$$

the subscripts 1 and 2 represent two operating points where the linearization is valid, and

$$\alpha = \left. \frac{\delta V}{\delta T} \right|_1 = \text{temperature coefficient of avalanche voltage}$$

and

$$R = \left. \frac{\delta V}{\delta I} \right|_1 = \text{electrical resistance which consists primarily of the depletion region space charge resistance plus any additional series resistance.}$$

The technique for measurement of the thermal resistance is based upon the application of this linear relationship for the three parameters, V, I and T.

The linear relationship, Equation (2.7-2), is solved for the temperature difference between operating points 2 and 1.

$$T_2 - T_1 = \Delta T = \frac{V_2 - V_1 - R(I_2 - I_1)}{\beta} \quad (2.7-3)$$

By definition, the thermal resistance  $\theta$  equals the difference in junction temperature rise  $\Delta T$  divided by the change in DC power dissipation  $\Delta P$  for the device between the two operating points 1 and 2. A fixed ambient or heatsink temperature is implied for operating points 1 and 2 as is the absence of RF power generation for the thermal resistance measurement. Therefore,

$$\theta = \frac{\Delta T}{\Delta P} = \frac{V_2 - V_1 - R(I_2 - I_1)}{\beta (V_2 I_2 - V_1 I_1)} \quad (2.7-4)$$

To determine the thermal resistance according to this equation, the coefficients  $R$  and  $\beta$  must be determined, and  $I$  and  $V$  must be measured at two operating points. The IMPATT must be at the same ambient temperature for each of these points. The measurements for determining  $R$  and  $\beta$  need not be totally independent of those for the two operating points 1 and 2. In the standard measurement method described, some of these measurements are combined to minimize the number of individual measurement operations to be performed. In this measurement method, all measurements are done at one of two bias current levels,  $I_1$  and  $I_2$ .

Normally, 5 mA is used for  $I_1$  and 55 mA for  $I_2$ . Other current values could be used. The operating points 1 and 2, therefore, are both defined as two conditions where the diode housing is held (by means of good heatsinking) at ambient room temperature defined as  $T_{A1}$ , and the applied diode bias current is 5 mA for point 1 and 55 mA for point 2. The resulting DC voltages  $V_1$  and  $V_2$ , respectively, which will be defined also as  $V_R$  (5 mA,  $T_{A1}$ ), and  $V_R$  (55 mA,  $T_{A1}$ ) respectively, are measured and recorded.

What remains to be determined in Equation (2.7-4) for calculating the IMPATT thermal resistance are the two parameters  $\beta$  and  $R$ . The parameter  $\beta$ , which is the rate of change of voltage with temperature at a fixed current, is determined by measuring the operating voltage of the IMPATT at two different ambient temperatures  $T_{A1}$  and  $T_{A2}$  and with the IMPATT biased at a fixed 5 mA DC in reverse breakdown. The respective voltages defined as  $V_R$  (5 mA,  $T_{A1}$ ) and  $V_R$  (5 mA,  $T_{A2}$ ) are recorded. Actually, the former of these voltages was measured in the previous step.  $T_{A1}$  is taken as the ambient room temperature,

and a temperature somewhere around 100°C is taken for  $T_{A2}$ . This elevated ambient temperature can be realized by placing the IMPATT mount on a temperature regulated hotplate. The two ambient temperatures  $T_{A1}$  and  $T_{A2}$  should not be confused with the actual junction temperatures at the two operating points 1 and 2. This set of measurements determines according to:

$$r = \frac{V_R(5 \text{ mA}, T_{A2}) - V_R(5 \text{ mA}, T_{A1})}{T_{A2} - T_{A1}} \quad (2.7-5)$$

The parameter R is the rate of change of voltage with current at a fixed temperature. To measure this parameter, a fast rise time pulse is used in the bias of the IMPATT under test. This allows the current to the IMPATT to be changed while the temperature of the IMPATT junction remains essentially constant, at least for a few nanoseconds following the rise of the pulse. With the IMPATT housing at ambient room temperature  $T_{A1}$  and the diode biased at a DC current level of 5 mA, a fast, low duty cycle bias pulse of 50 mA pulse current is applied and the pulse voltage rise on the IMPATT  $V_p(5-55 \text{ mA}, T_{A1})$ , at a time less than a few nanoseconds into the pulse, is recorded. The value for R is then:

$$R = \frac{\Delta V_p(5-55 \text{ mA}, T_{A1})}{0.050} \quad (2.7-6)$$

Now all measurements have been made to determine the IMPATT thermal resistance according to Equation (2.7-4). The thermal resistance can be expressed directly in terms of the various measured values of voltage, current and temperature, as they have been defined in the description of the measurement, as follows,

$$r = \frac{|T_{A2} - T_{A1}| \times |V_R(55 \text{ mA}, T_{A1}) - V_R(5 \text{ mA}, T_{A1}) - V_p(5-55 \text{ mA}, T_{A1})|}{|V_R(5 \text{ mA}, T_{A2}) - V_R(5 \text{ mA}, T_{A1}) \times .055 \times V_R(55 \text{ mA}, T_{A1}) - .005 \times V_R(5 \text{ mA}, T_{A1})|} \quad (2.7-6)$$

Figures 2.7-1 and 2.7-2 are block diagrams of the test setups used for making the DC and the pulsed measurements involved in the measurement of thermal resistance of IMPATTs.

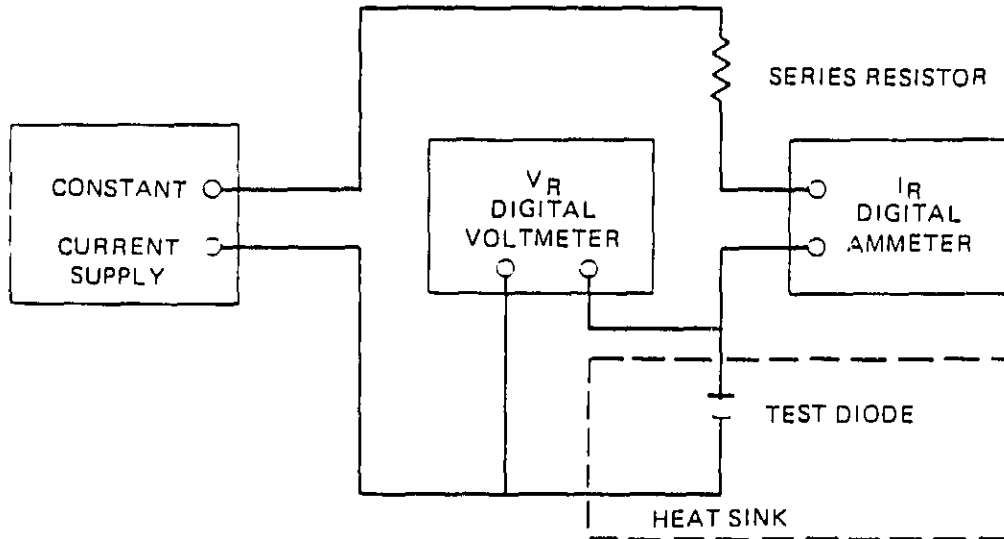


Figure 2.7-1 Test setup for DC parameters required for the measurement of thermal resistance of an IMPATT diode.

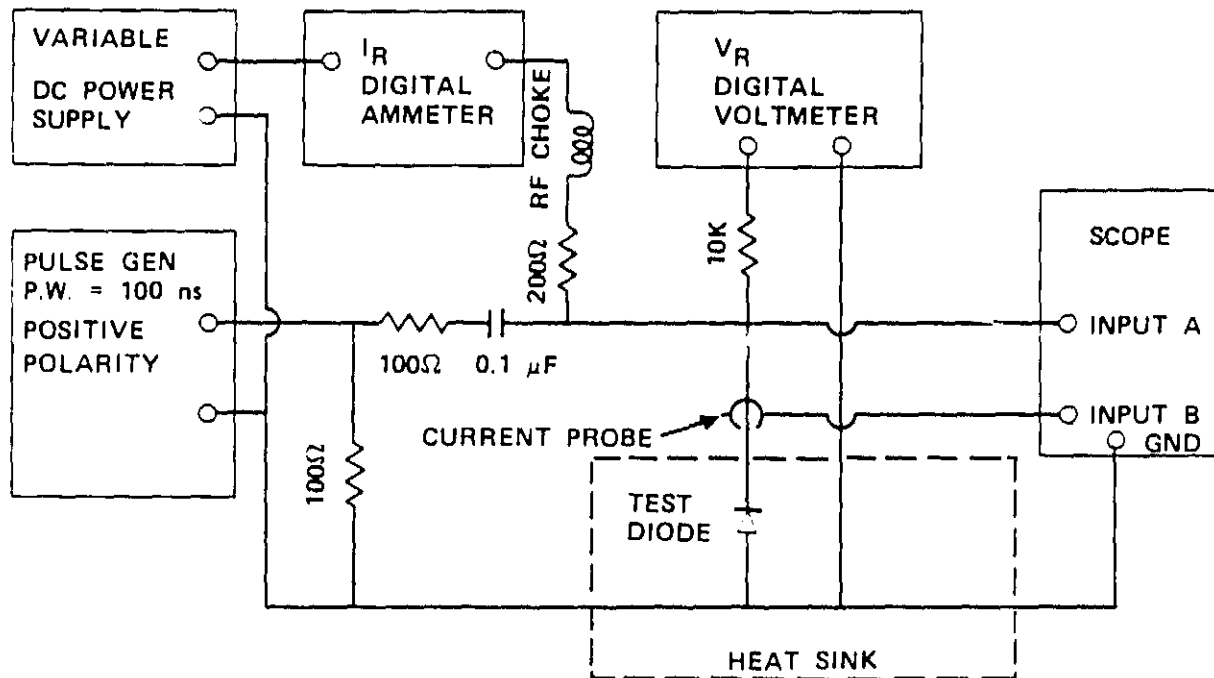


Figure 2.7-2 Test setup for pulse parameters required for the measurement of thermal resistance of an IMPATT diode.

## 2.8 SILICON IMPATT RELIABILITY

Silicon IMPATT diodes fabricated according to this Hughes process have been subjected to comprehensive life testing under a number of R&D programs starting in 1972. Over these ten years, considerable data have been accumulated which establish projections for the reliability of Hughes silicon double-drift diodes. Test procedures and dedicated facilities have been developed at Hughes for IMPATT reliability studies, and a concerted effort has been given to failure analysis to identify failure modes.

No reliability testing was performed specifically as part of the contract for the V-band amplifier development program. However, some of the IMPATTs used on this program were developed under a past development program in which extensive reliability studies were made on those devices packaged with diamond heatsinks. Also, the newer diode lots which were fabricated as part of this program were fabricated by essentially the same processes; therefore, the reliability of the new lots should be the same as the reliability of those lots on which extensive reliability studies were made. The many reliability studies performed at Hughes on Hughes silicon double-drift IMPATTs have indicated that this is true. In this section, the accelerated life testing procedures performed on the Hughes double-drift silicon IMPATTs are described, and the resulting reliability projections are presented.

To obtain adequate information on IMPATT reliability and wear-out in a reasonable amount of time, it is necessary to resort to accelerated life testing. Accelerated life test techniques can be organized into two general categories: step-stress testing and constant-stress testing. In a step-stress test, devices are operated for a fixed period of time at each of a series of increasing stress levels until all have failed. The specific stress parameter chosen for these IMPATT diodes is the same as that is chosen for life testing of most semiconductor devices in general, i.e. temperature. The purpose of step-stress testing is to establish operating stress levels that will accelerate the formation of failure mechanisms in a relatively short period of time. Step-stress testing is also useful for determining operational limits and for establishing device screening procedures useful in eliminating early failures.



In a constant-stress test, each group of diodes tested remains at the same level of stress for the entire duration of the test. The stress levels are sufficient to accelerate device failures so that an adequate amount of failure rate data for statistical analysis can be generated in a reasonable time. A regression analysis is used to extrapolate constant-stress test data to obtain reliability information regarding normal operating levels. The results of such testing are easier to interpret for analytical purposes than step-stress results, as the effects of prior stress levels do not have to be considered. In general, the constant-stress levels chosen, as well as pre-test screening procedures, can be determined from the results of prior step-stress testing.

Hughes silicon IMPATT diodes are currently being flown in space with excellent reliability. Similar diodes have been under RF constant-stress testing for the past 10 years, and these tests are still ongoing. The reliability data previously obtained based on accelerated testing have now been verified under actual RF conditions.

#### 2.8.1 Step-Stress Testing

The actual DC step-stress life testing of IMPATT diodes is very straightforward. Packaged diodes are soldered onto copper studs. These studs are then screwed into holes provided in a water-cooled constant-temperature base plate. With the diodes mounted in the life test fixture, the thermal resistance and initial electrical data are measured and entered into a log book. The diodes are then reverse-biased into avalanche breakdown. The bias current of each diode is adjusted so that the product of the DC power dissipated and the measured thermal resistance of the diode equals the desired operating junction temperature rise above the temperature of the water-cooled base plate. When all the diodes in a group are operating, the test is considered started, and the accumulated operating time is monitored. The diodes are then operated continuously for approximately 72 hours. During this time, operating conditions are monitored and recorded daily. If a diode has opened or shorted, the time-to-failure figure is recorded. After 72 hours, the power is removed and the initial electrical measurements are repeated and recorded. The surviving diodes are then brought up to the next step junction temperature and the operating test time is continued. This approximately

72-hour cycle is then repeated until all the diodes in the group fail. The initial junction temperature normally chosen is 250°C, and the step size is 25°C.

Figures 2.8-1a and 2.8-1b represent combined histograms of the step-stress test results conducted on three 44 GHz and three 60 GHz silicon double-drift IMPATT diode lots. Failures for these tests were taken to be catastrophic, i.e., either short- or open-circuited devices. A large number of diode failed around 375-425°C in the step-stress test. The failure mode for all diodes was a short circuit. This is the failure mode commonly observed for millimeter-wave silicon IMPATTs under either DC or RF operating conditions.

### 2.8.2 Constant-Stress Testing

After sufficient data have been obtained from the step-stress tests, constant-stress testing is initiated in order to make a quantitative projection of diode life expectancy. Results of the constant-stress tests have indicated that the IMPATT failure distribution was relatively well-ordered. The overwhelmingly predominant failure mode was a shorting, resulting from a single mechanism consisting of the formation of a gold-silicon alloy spike which short-circuited the p-n junction, as failure analysis using a scanning electron microscope has indicated. Statistical and graphical analysis of the observed failure distribution confirmed that the failure occurrence was distributed as a log-normal variable, the same distribution observed for many types of semiconductor devices. These observations give confidence that the anticipated failure distribution for the silicon millimeter-wave double-drift IMPATT diodes is also distributed log-normally and that the analysis of test data should therefore be straightforward.

The procedure for constant-stress testing is very similar to that of step-stress testing. The main difference is that in constant stress testing, devices in a given test group are maintained at the same junction temperature level throughout the test. The precise temperature values selected for constant-stress testing are derived from an analysis of the step-stress data. Typically, three constant-stress temperatures are selected with 24 diodes tested at each temperature.

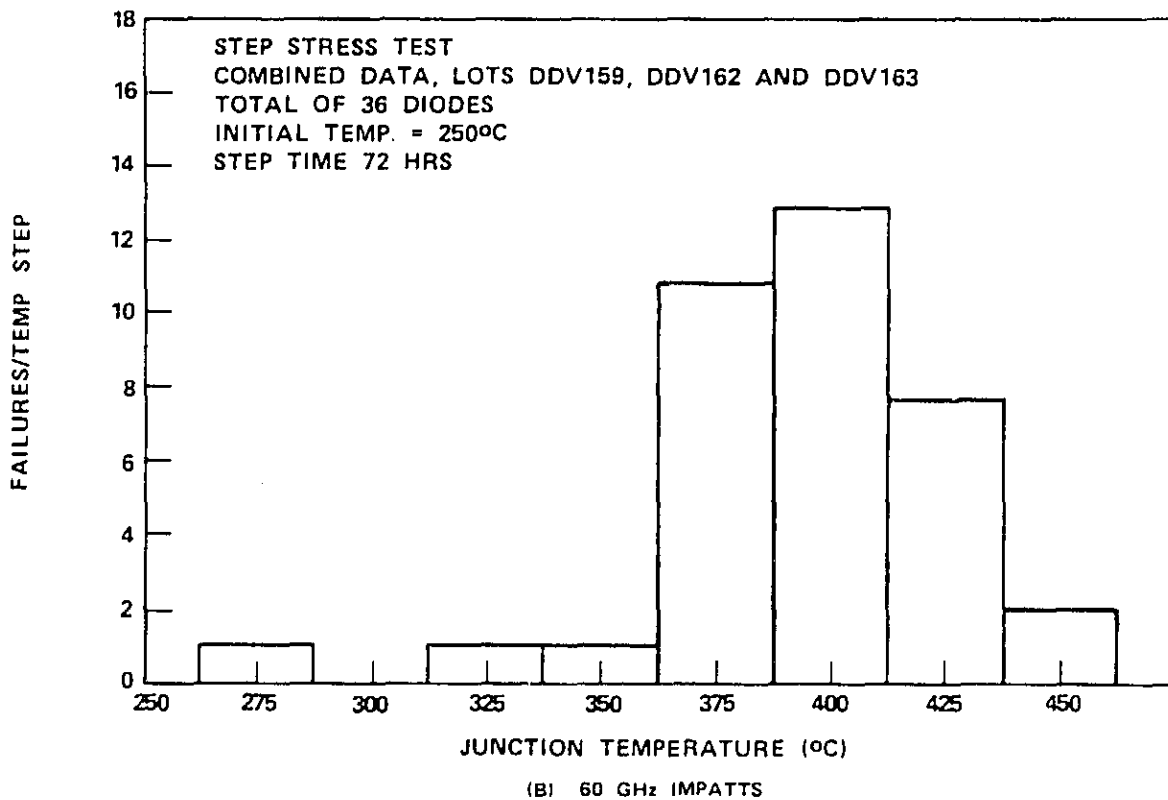
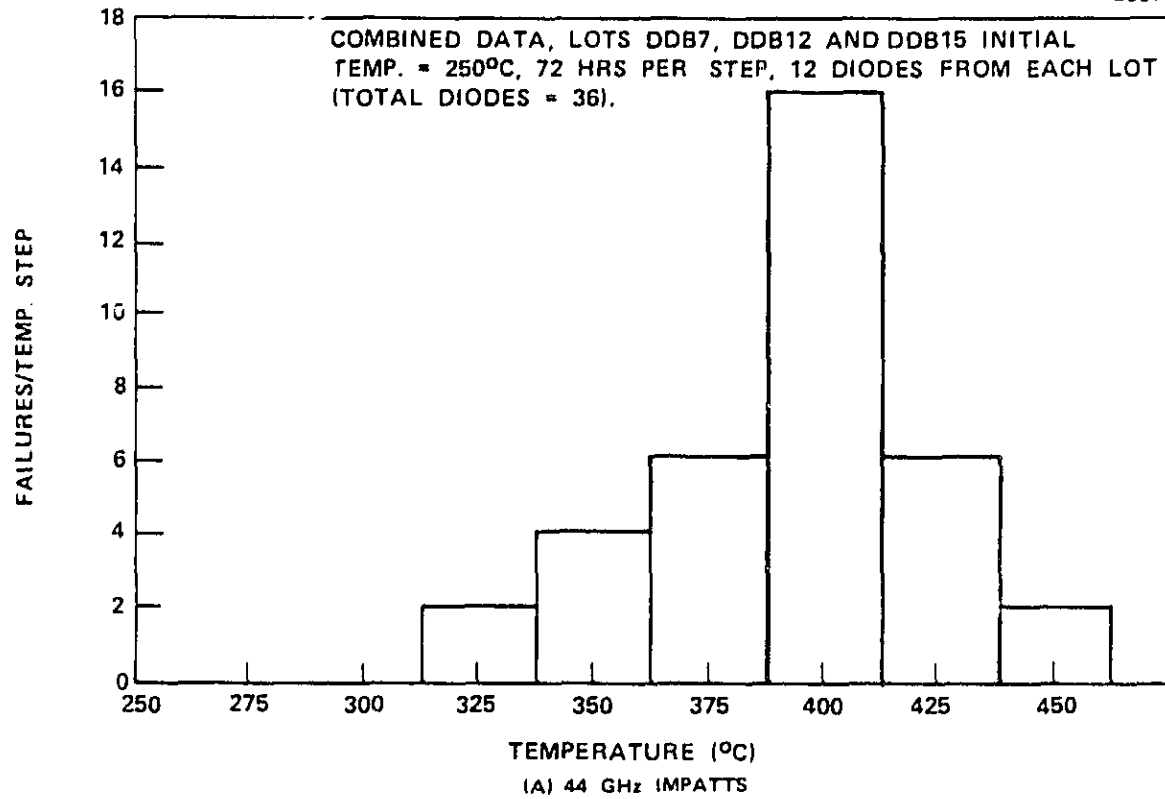


Figure 2.8-1 Combined histograms of step-stress test results.

Data obtained from constant-stress tests on silicon 44 GHz and 60 GHz double-drift IMPATT diodes on diamond heatsinks is presented in Figures 2.8-2 and 2.8-3. In Figure 2.8-2, cumulative percent failures are plotted as a function of time in special log-normal probability paper. This paper has a normal probability scale for the abscissa and a logarithmic time scale for the ordinate. The data plotted show that the results of constant-stress tests at three different temperatures could be fit with a straight line. This indicates that the log-normal distribution is appropriate. The variance of the distribution is related to the plotted line slope. A conclusion to be derived from the plots is that the variance is nearly the same for the three temperatures and that it is reasonable to assume that a single failure mechanism is operative.

The Arrhenius equation can be used to relate the time-to-failure at different temperature levels. The equation can be written as:

$$t_f = C \exp (E/kT) \quad (2.8-1a)$$

where  $t_f$  is the time-to-failure for a given percentile of the population, i.e., time to 50 percent failure or median-time-to-failure (MTTF), time to 5 percent failure, etc.; C and E, the activation energy, are constants derived by fitting Equation (2.8-1) to the experimental data; k is the Boltzmann constant; and T is the temperature in degrees Kelvin. To solve for activation energy E, time to failure, two temperatures are taken. Thus from Equation 2.8-1a

$$E = \frac{k}{\left(\frac{1}{T_1} - \frac{1}{T_2}\right)} \ln \left(\frac{t_1}{t_2}\right) \quad (2.8-1b)$$

where

$$t_1 = \text{Time to failure at temperature } T_1$$

$$t_2 = \text{Time to failure at temperature } T_2$$

Once the constants in Equation (2.8-1a) are determined, it can be used to estimate the MTTF (or time-to-failure for other specified percentiles) for any operating temperature so long as the failure mechanism does not change. The extrapolation to temperatures of interest can most easily be carried out by

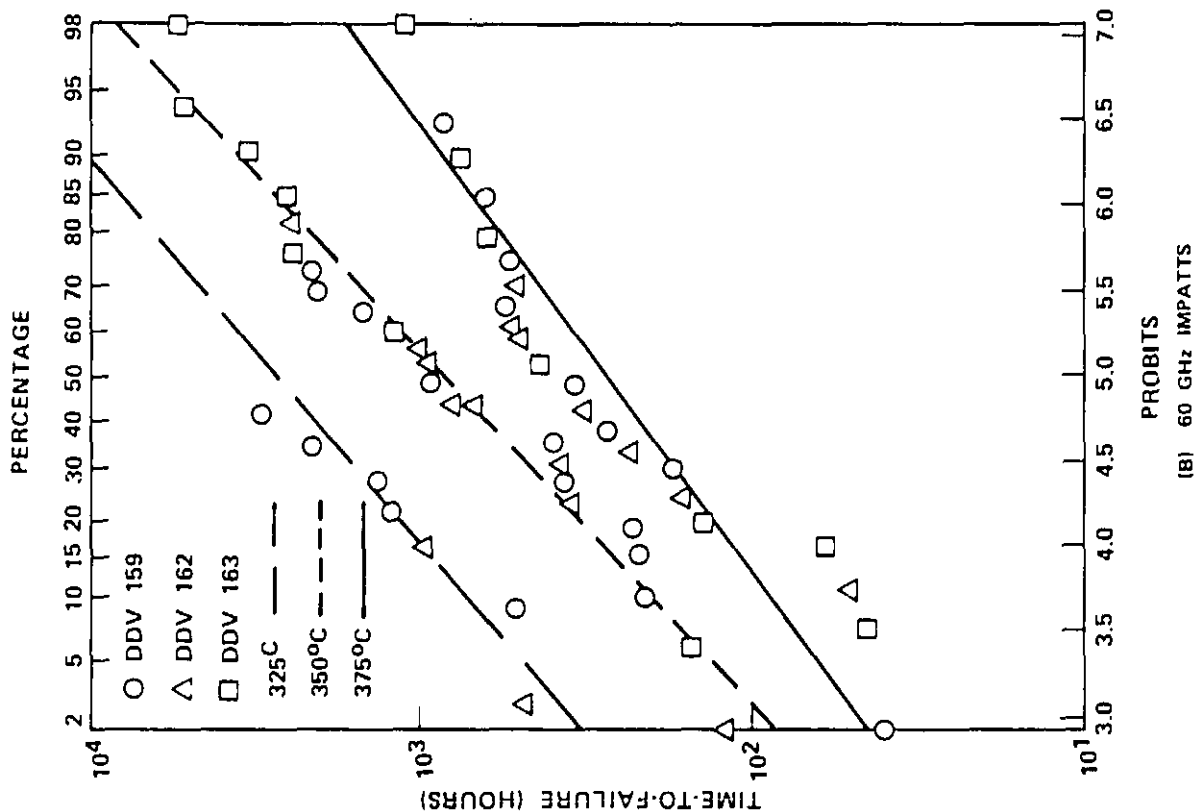
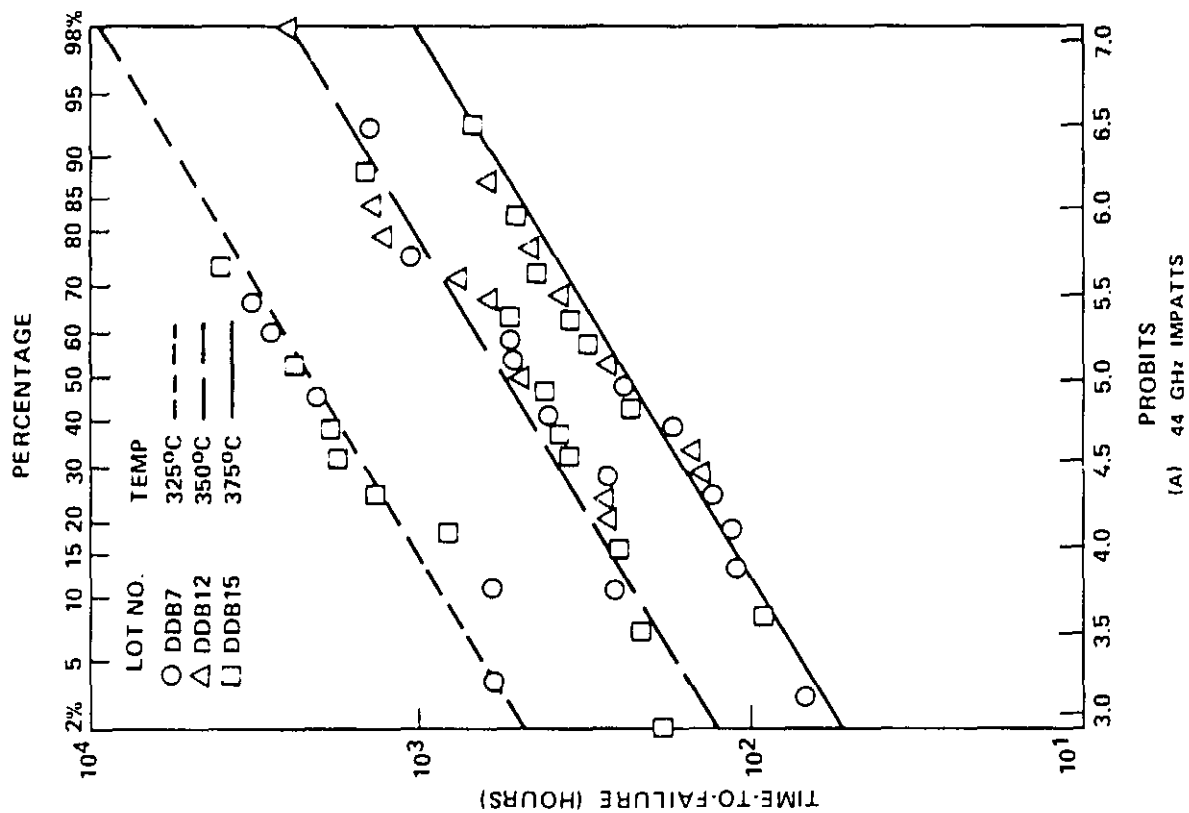


Figure 2.8-2 Log-normal plots of cumulative failure distributions.

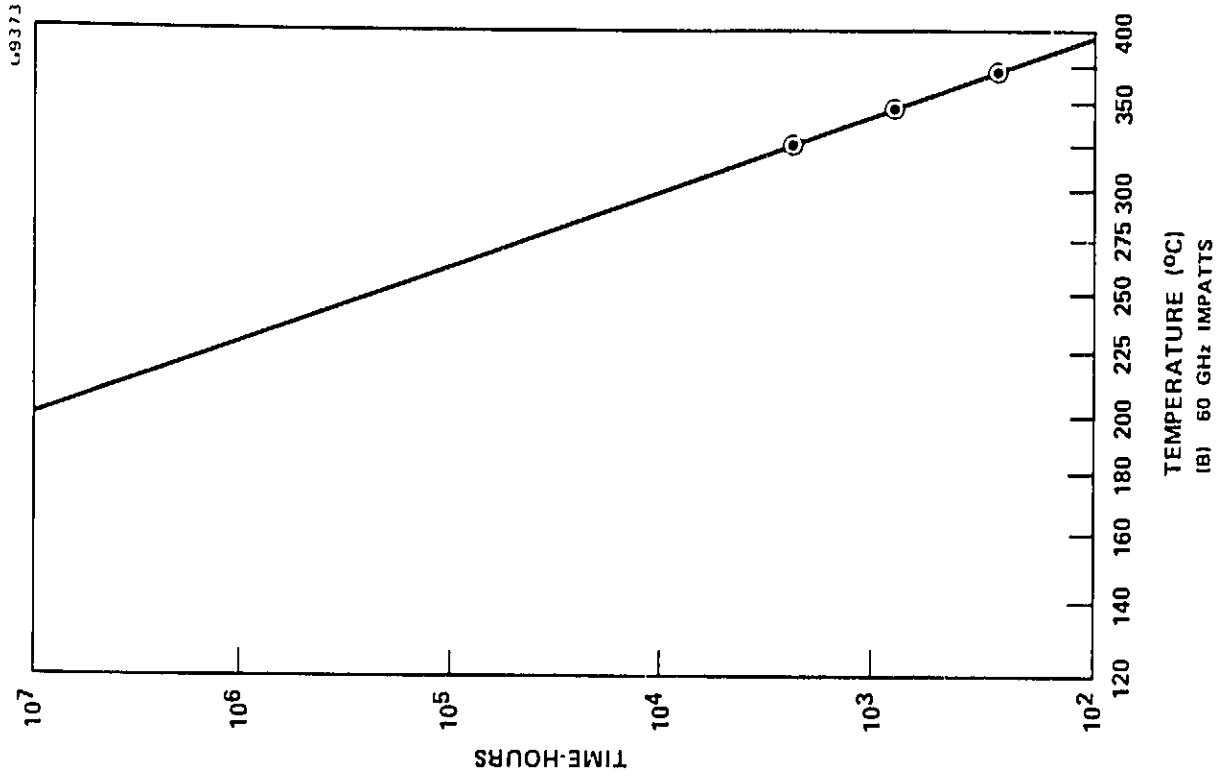
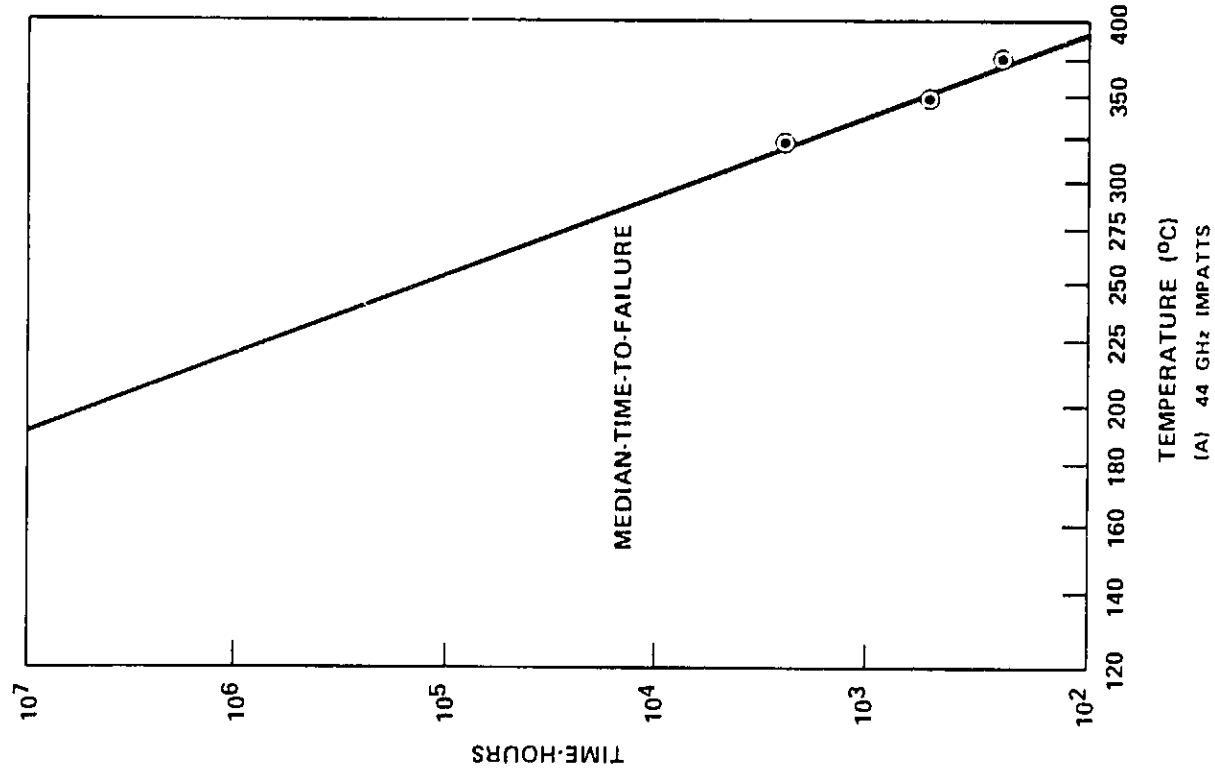


Figure 2.8-3 Estimated MTF vs junction temperature of silicon double-drift IMPATT diodes.

fitting Equation (2.8-1b) to test data on paper which has a logarithmic time scale and a reciprocal absolute temperature scale. The results of this technique are illustrated in Figure 2.8-3 where the MTTF data from Figure 2.8-2 have been plotted. The line representing Equation (2.8-1) has been fit to the three data points. This line can be extrapolated to estimate the MTTF at other temperatures where life testing is not practical. Nearly identical MTTF versus junction temperature relationships are indicated for the 44 GHz and the 60 GHz IMPATTs. For example, the MTTF of silicon double-drift IMPATT diodes is estimated to be about  $1 \times 10^6$  hours at  $225^{\circ}\text{C}$  and  $2 \times 10^5$  hours at  $250^{\circ}\text{C}$ .

A representative test station used in the step-stress and constant-stress accelerated life test is shown in Figure 2.8-4. The test station is designed to permit periodic monitoring of the DC conditions of each diode under test without physically removing the diode from the mounting stand. Figure 2.8-5 is a block diagram of the main components of the station, namely the DC power supply, individual coarse and fine current-adjust controls, current-limiting resistors, individual I-V readout jacks, and the test diode mounting stand in dry nitrogen atmosphere. A chart recorder is used to monitor continuously the total bias current to the test stations. Changes in the current level indicate the exact failure time in the event that a diode fails.

Protective measures are taken wherever possible to prevent unnecessary damage to the test diodes. Current-limiting resistors are used to prevent excessive current when a diode shorts; a DC power supply having an excellent voltage regulation and negligible voltage-overshoot in the event of an electrical power outage is selected; an over-temperature control system is included to reduce the power supply voltage to a value less than the breakdown voltage of the test diodes when the temperature of the diode stand exceeds a preset limit; and finally, an alarm and automatic emergency dry nitrogen supply system are included in event that the house nitrogen supply is interrupted. The temperature of the diode test stand is controlled by pressure regulated chilled water flowing continuously through the channels inside the stand and the water is maintained at  $18 \pm 2.5^{\circ}\text{C}$ . The temperature of this stand is monitored by means of a thermocouple embedded into the stand.

ORIGINAL PAGE IS  
OF POOR QUALITY

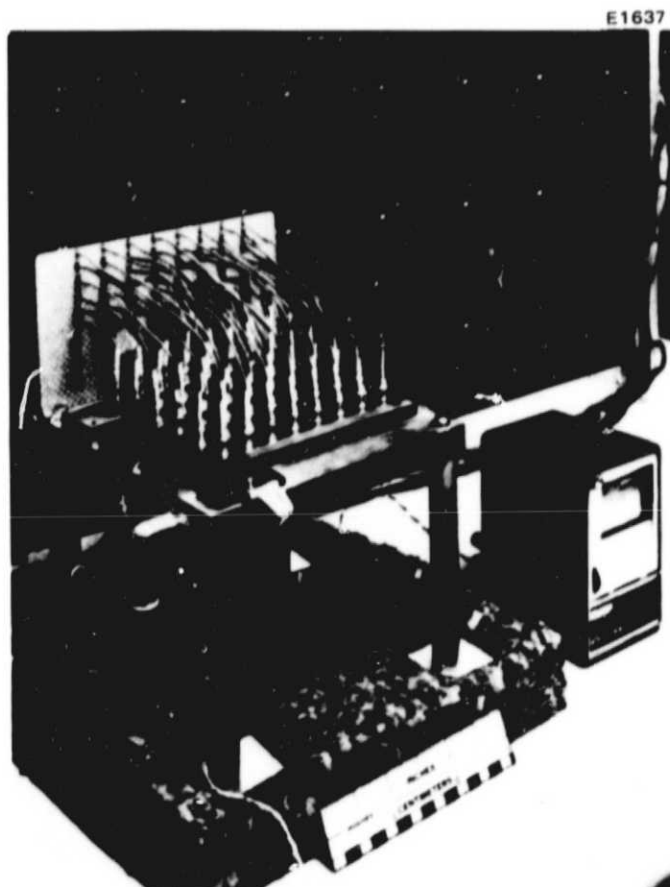


Figure 2.8-4 IMPATT diode life test station.



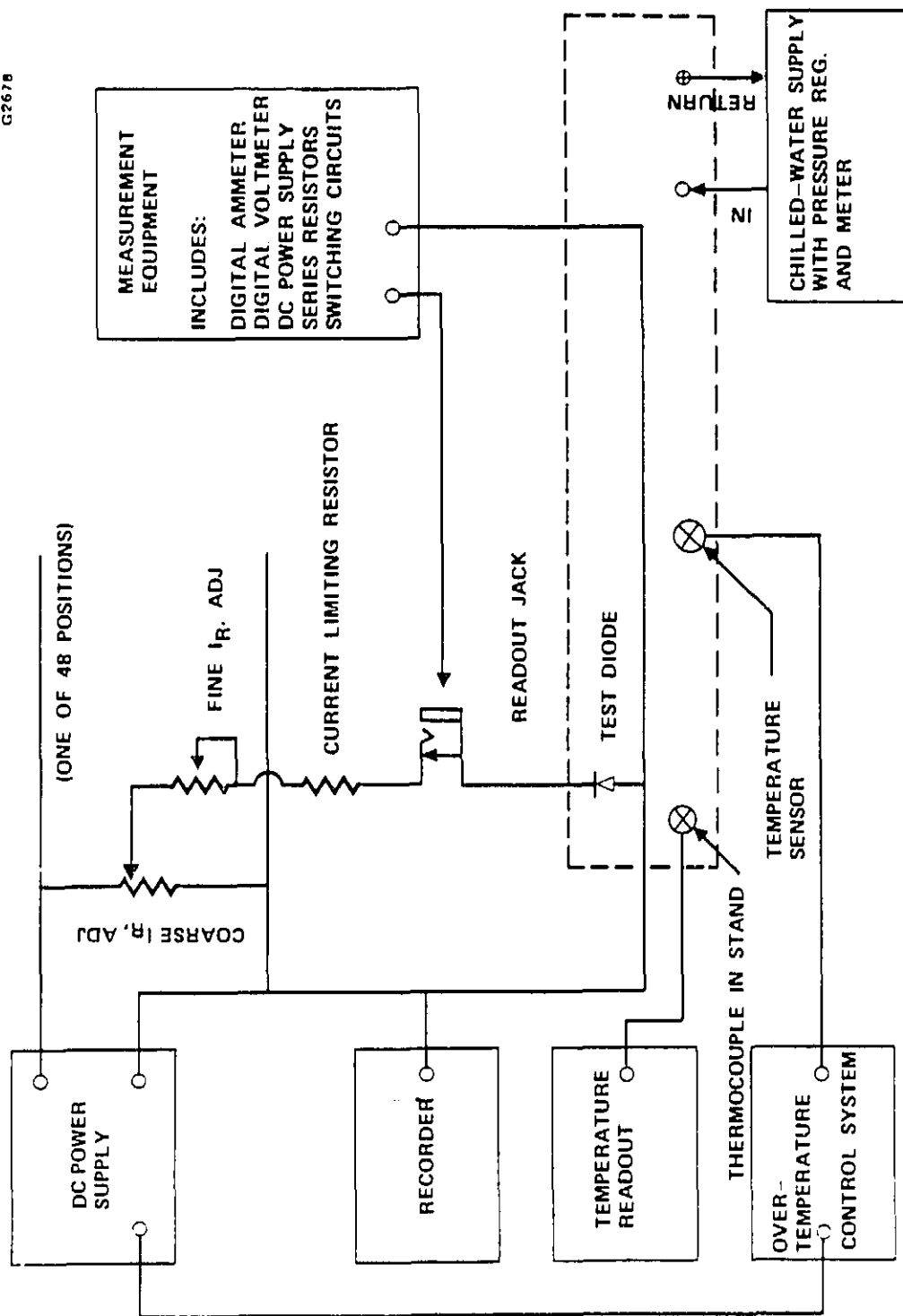


Figure 2.8-5 IMPATT diode life test station. Broken lines represent mounting stand (in dry nitrogen atmosphere).

### 3.0 COMPONENT TECHNOLOGY FOR IMPATT AMPLIFIERS

There are a number of major components whose general configuration is common to most or all stages of the solid state V-band transmitter. The general features of these components will be described in this section. The specific features of these components which result in the required performance for each individual stage of the transmitter are discussed in subsequent sections. The silicon IMPATT devices are described in Section 2.0. The components described in this section are: (1) the coaxially-coupled, reduced-height waveguide circuit in which the IMPATT operates in each stage of the transmitter; (2) circulators used to separate the input and output signals from the one-port amplifier; (3) hybrid couplers which are used for module-level power combining; (4) and the current regulators which are used to condition the bias for each IMPATT device on the transmitter.

#### 3.1 COAXIALLY-COUPLED, REDUCED-HEIGHT WAVEGUIDE CIRCUIT

From the the onset of this program, the approach to the development of the transmitter was to utilize metallic waveguide as the transmission medium throughout. Metallic waveguide has advantages over alternative approaches such as stripline and finline: It is lower in loss, and such components as ferrite devices, hybrid couplers, and test instruments are available as catalog products. Waveguide circuits, properly designed, can be modified easily and lend themselves readily to empirical development, a very important feature for the development of the variety of amplifier stages required for this program. A general type of IMPATT circuit fabricated in waveguide which has proven highly successful at Hughes for the development of circuits for essentially any type of operation of IMPATT devices is the coaxially-coupled, reduced-height waveguide circuit. IMPATTs are, in general, low-impedance devices, and the reduced-height waveguide section provides a lower impedance region, compared to full-height waveguide, to assist in the impedance matching of the IMPATT. Transition from reduced-height to full-height waveguide is by means of a multiple-section step transformer, typically consisting of three quarter-wave sections of waveguide machined into the same section along with the reduced-height waveguide. The coaxial section provides a convenient means to deliver the DC bias current to the IMPATT and to provide an additional

and a very wide-ranging means of impedance matching of the IMPATT. Figure 3.1-1 is a cross-sectional schematic illustration of this general coaxially-coupled, reduced-height waveguide circuit. A two-section coaxial matching transformer located between the reduced-height waveguide and the IMPATT diode is shown in the figure. However, any number of coaxial matching sections, from zero up to some practical limit, may be used.

The physical realization of the coaxially coupled, reduced-height waveguide circuit used in the development and final fabrication of the various stages of the transmitter is of modular design, featuring simple interchangeability of various circuit elements. This allows a discrete change to be made in the dimension or material of one part of the circuit at a time while the remainder of the circuit is essentially unchanged. Besides the means to make discrete adjustments in the circuit, continuous tuning adjustments can be made by the sliding backshort and the positioning of the bias choke.

Another important feature of the coaxially coupled, reduced-height waveguide circuit hardware is convenient removal and replacement of the IMPATT device without disassembling the circuit. The packaged IMPATT devices are built up on gold-plated copper cylinders 0.160 inches in diameter and 0.118 inches in height. These devices can be placed into a hole provided in the IMPATT circuit housing and locked into place with a threaded plug. This capability saves time and allows a series of diodes to be evaluated in the circuit without disturbing the sometimes critical alignment of circuit parts as each device is inserted into and removed from the circuit. This minimizes the variation in the impedance of the circuit between the testing of each IMPATT device. Figure 3.1-2 is a photograph of the assembled V-band coaxially-coupled, reduced-height waveguide circuit. Figure 3.1-3 shows an exploded view of the disassembled hardware including two coaxial matching sections. The bias pin forms the center conductor of the coaxial matching sections of generally fixed center conductor diameter. The length and outer diameter of the coaxial sections are determined by the thickness and diameter of a hole machined into, respectively, metallic rectangular shims. The length and outer diameter of each coaxial section can be conveniently changed in discrete steps by replacing these shims.

G2010

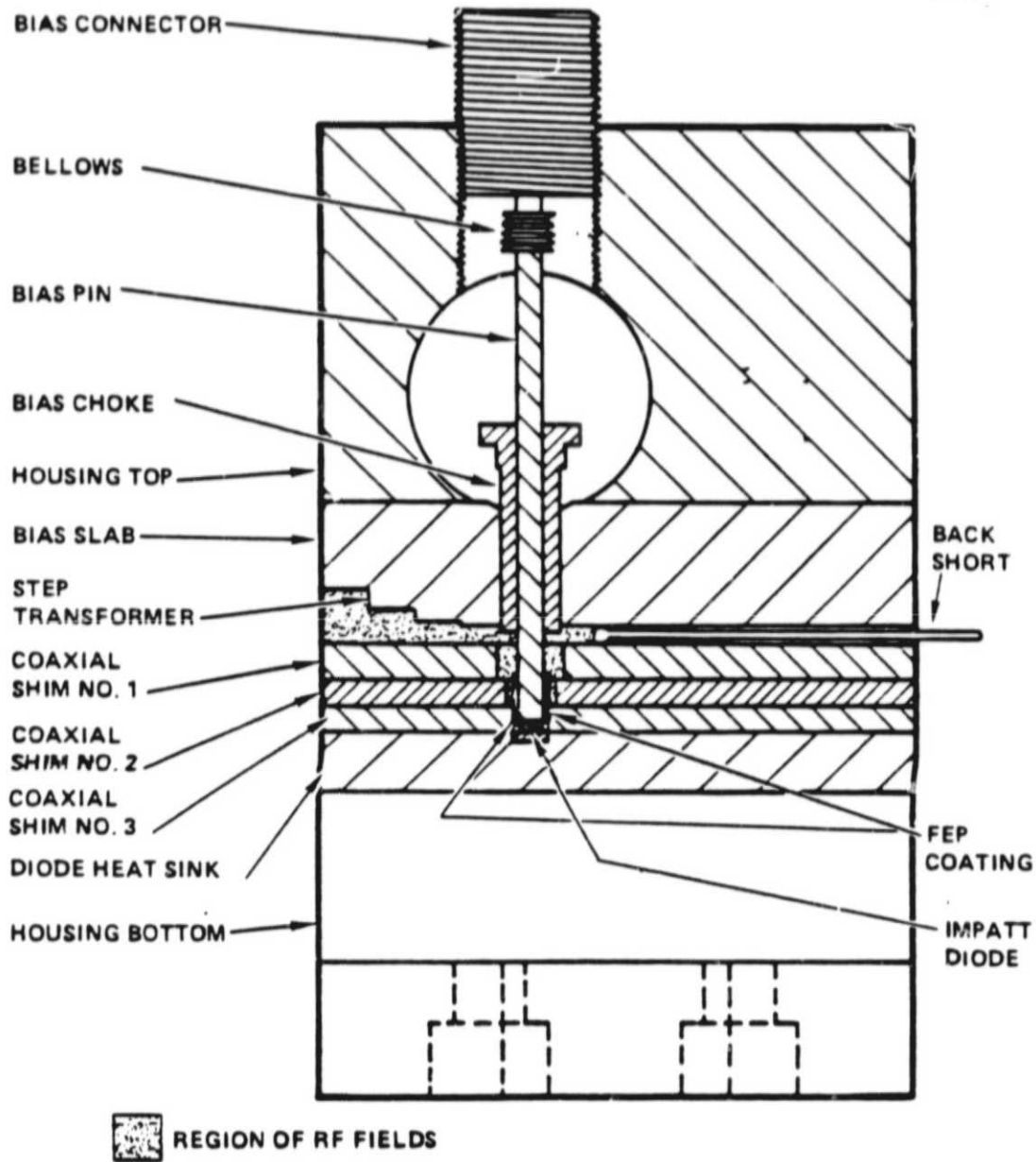


Figure 3.1-1 Scale drawing of the single-diode V-band free-running and injection-locked oscillator circuit.

E3664

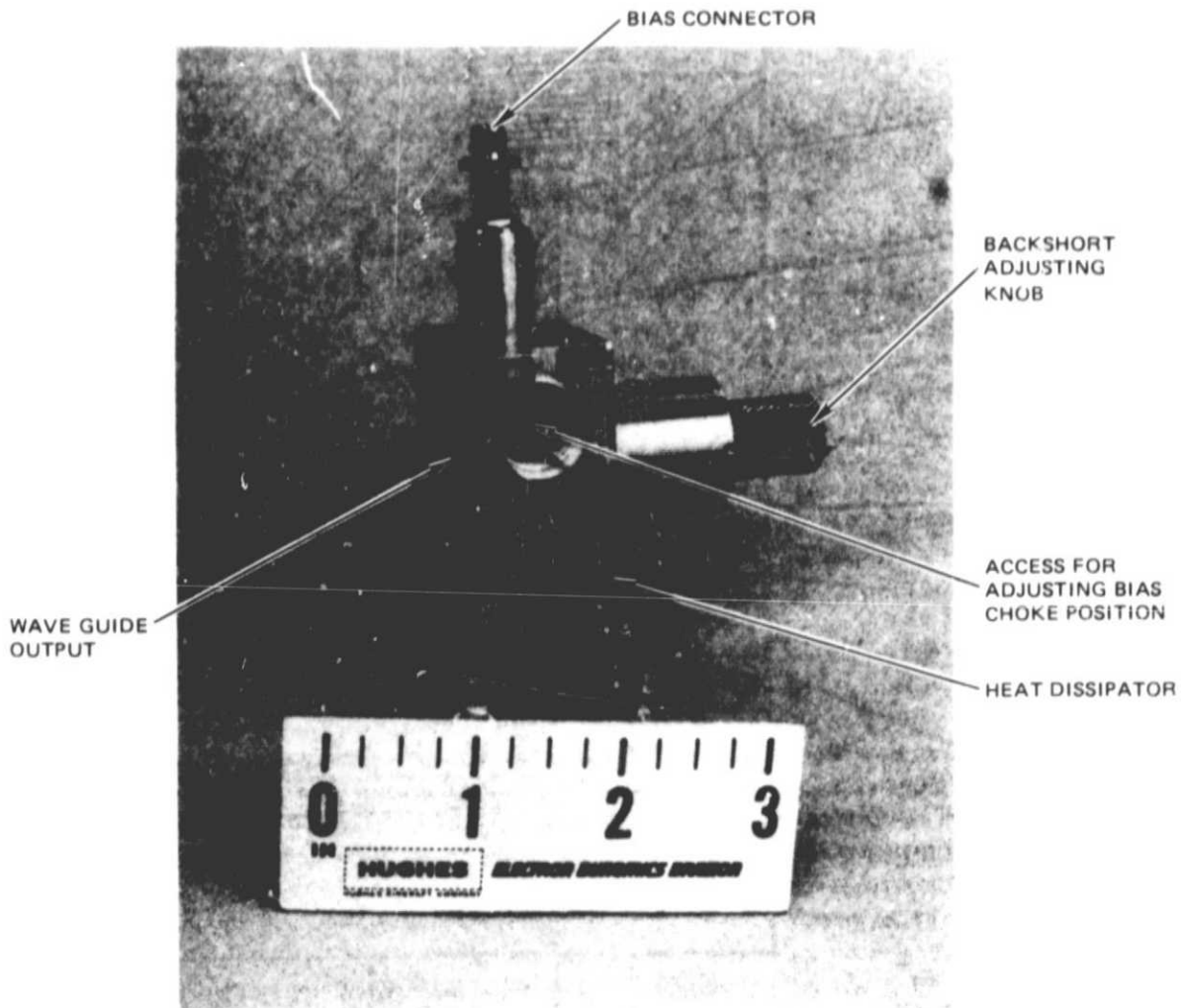


Figure 3.1-2 Developmental version of the single-diode free-running and injection-locked oscillator circuit.

E3665

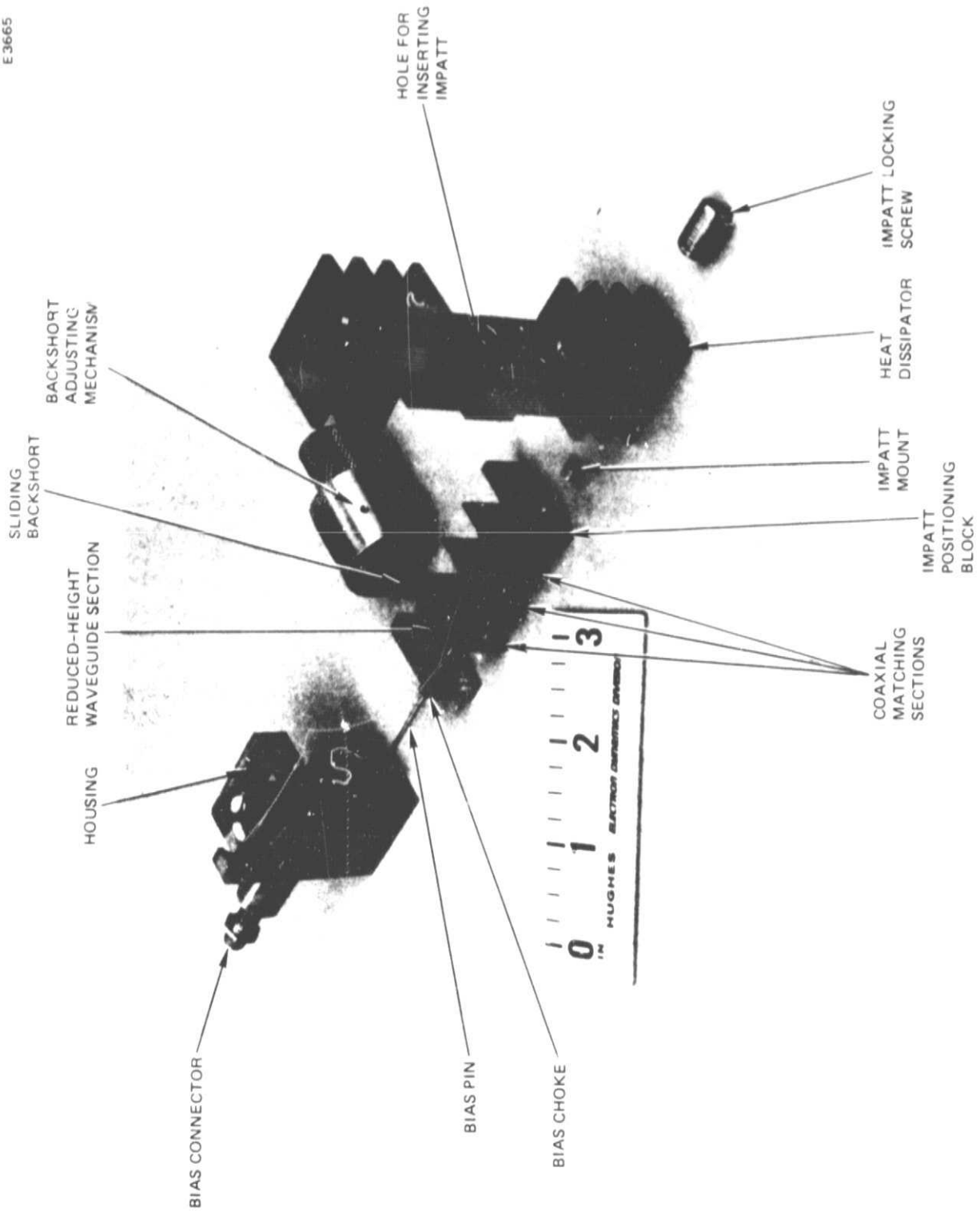


Figure 3.1-3 Exploded view of the developmental version of the single-diode Q-band free-running and injection-locked oscillator circuit.

The development of each different type of amplifier stage for the transmitter consisted of determining the proper combination of the various circuit parameters, along with selection of suitable IMPATT device epitaxial material and device package configuration. This process proceeds primarily in an experimental manner. Analytical computer models have been developed at Hughes to model the IMPATT device and the coaxially coupled, reduced-height waveguide circuit. However, these models cannot account for many subtle details of the IMPATT device and the circuit. These models are useful for indicating general effects but have not yet been particularly successful in providing direct designs for these IMPATT circuits. The precise configuration of the coaxially coupled, reduced-height waveguide circuits developed for each stage of the transmitter are specified in Section 4.0.

### 3.2 FERRITE COMPONENTS FOR IMPATT REFLECTION AMPLIFIERS

Twelve separate ferrite components, each fabricated in V-band (WR-15) waveguide, are installed on the final version of the V-band solid state transmitter. Among these twelve ferrite components are four three-port junction circulators, seven terminated three-port junction circulators which act as isolators, and a Faraday rotation isolator. These ferrite components each serve one or both of two important functions. One of these functions is to provide separate ports for the incident signal going into, and the reflected amplified signal coming out of, the one-port IMPATT reflection amplifier. The other function of the ferrite components is to provide isolation of the output ports of each stage from unwanted incoming signals to these ports. These unwanted input signals can originate from a partial reflection of the output power of that stage off of a mismatch in the load into which it is working, or from leakage of output power from the next stage back through its input port and into the preceding stage.

The primary parameters which specify the performance of the ferrite components are isolation, return loss, insertion loss and bandwidth. If available ferrite components were ideal in their performance, then there would be little need to determine and specify minimum performance specifications for them. For this program a relatively simple analysis, based upon a relatively simple model of the ferrite component and the one-port reflection amplifier, was

performed which greatly assisted in the setting of performance standards of these ferrite components. This analysis clarified the limitations which less than ideal ferrite components can impose upon the performance of the one-port reflection amplifier. Section 3.2 concerns the development work performed on this program in the area of ferrite components as it relates to the development of the transmitter. This activity consisted primarily of: (1) the analysis of the performance requirements of the ferrite components (discussed in Section 3.2.1); and (2) the testing and fine tuning adjustment made on the catalog grade ferrite components to ensure that these components met the derived specifications (discussed in Section 3.2.2). Before these tasks were carried out it was extremely difficult to obtain the required 4.2 percent minimum bandwidth from any of the IMPATT amplifier stages. Also, before this analysis was performed it was not clear that inadequate performance of the ferrite components was in fact the primary limiting factor in the operation of the IMPATT amplifiers.

### 3.2.1 Effect of Finite Return Loss of a Circulator on an Injection Locked Oscillator

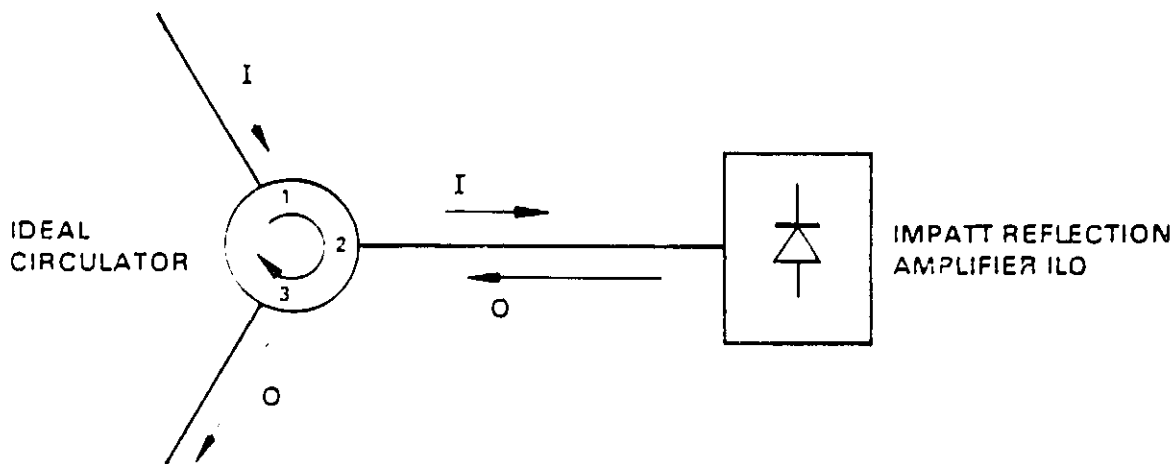
The most common configuration for a solid state millimeter-wave amplifier stage is a one-port reflection amplifier module working into a three-port circulator. The primary role of the circulator is to provide separate ports for the input and output signals of the amplifier stage. It has been determined that, as the gain per stage, bandwidth and phase uniformity requirements for solid state millimeter-wave amplifiers are increased, the return loss of off-the-shelf circulators can become a limiting factor in the operation of the amplifier which often cannot be overcome by further improvements in the reflection amplifier module alone. Often, improved circulators must be developed to extend the performance of the amplifier. This subsection is intended to illustrate, by means of a simple analysis, the effects caused by a finite return loss of a circulator on a wideband injection-locked oscillator. The analysis will proceed with minor modifications for a linear amplifier, but this case will not be discussed explicitly.

A partial reflection at the circulator of the output signal of the one-port amplifier will interfere with, i.e., vectorially add to or subtract from,

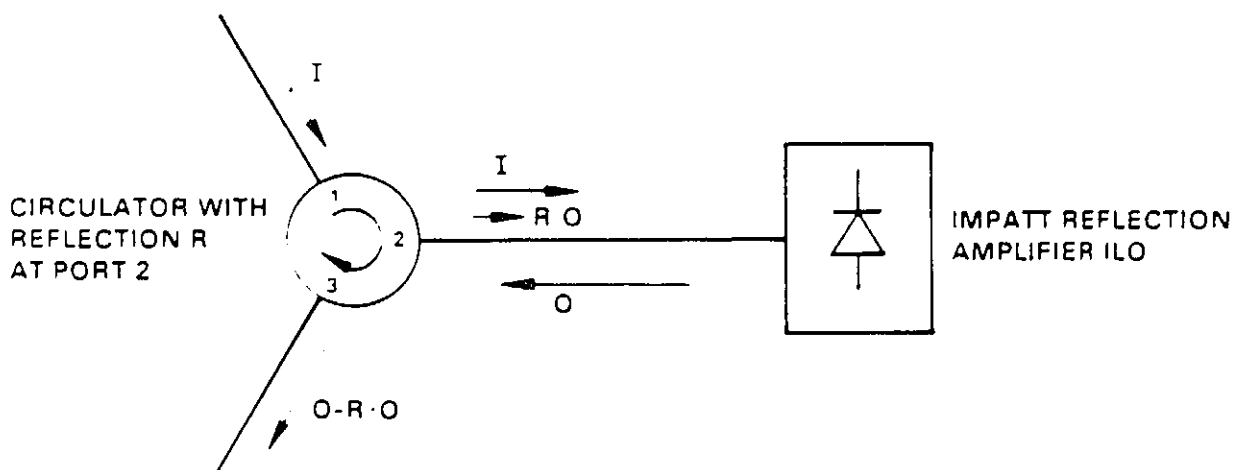


the intended input signal to that amplifier depending upon their relative phases. Therefore, the actual signal directed into the one-port reflection amplifier could vary in both phase and amplitude from the signal that is applied to the input port of the circulator. The present analysis will determine the range of this amplitude and phase variation, as a function of the gain of the one-port amplifier and as a function of the return loss of the circulator. The performance of an injection-locked oscillator reflection amplifier is generally degraded when the input power level is varied significantly. In addition, when the individual output powers of two or more amplifiers are combined, differences in phase transfer characteristics among the amplifiers, which can be caused by this finite return loss, will lead to reduced power combining efficiency and possibly other undesired effects. Consequently, the effect of circulator return loss on the amplifier module must be understood quantitatively in order to set reasonable specifications for the circulator.

The model that was analyzed is that of a one-port injection-locked oscillator (ILO) reflection amplifier module working into a three-port circulator. It is assumed that the power output of the one-port ILO is independent of the input power level. An ideal lossless three-port circulator having no reflections at any port, and with an IMPATT reflection amplifier  $11a'$  mounted on one port is, shown in Figure 3.2-1a. The externally applied input signal power  $I$  is shown which is directed by means of the circulator into the reflection amplifier. The amplifier produces a constant output power level  $O$  which, in this ideal case, is directed out of the remaining port of the ideal circulator without any reflection. Figure 3.2-1b illustrates the case in which the circulator is ideal, except that it presents a power reflection  $R$  at the amplifier port. The constant output signal power  $O$  from the amplifier then produces at this port a reflection whose power is equal to  $R \cdot O$ . The reflected signal  $R \cdot O$  combines with the intended input signal  $I$  to produce an actual input signal to the amplifier which is different in phase and magnitude from the intended value. To determine the phase and amplitude of this actual input signal, the voltages of the intended input signal  $I$  and of the reflected signal  $R \cdot O$  must be combined by vector addition.



(a)



(b)

Figure 3.2-1 Configuration for a one-port reflection amplifier injection-locked oscillator working into a three-port circulator: (a) case of an ideal circulator, (b) case of an ideal circulator except that it presents a power reflection  $R$  at Port 2.

Figures 3.2-2a through 3.2-2e illustrate this vector addition for various cases. In these figures, the amplitudes of the intended input signal  $I$  and of the reflection  $R^*O$  are held fixed, but cases for different phases for  $R^*O$  are shown. Therefore, the resultant vector  $V$  will lie on a circle whose radius is equal to the magnitude to  $R^*O$ . Figure 3.2-2a shows the general case. In Figures 3.2-2b and 3.2-2c, the voltage vectors corresponding to the intended input signal  $I$  and the reflected signal  $R^*O$  add to the maximum and minimum values of actual input voltage, respectively. As these figures indicate, if  $R$  is the power reflection coefficient and  $G = O/I$  is the nominal power gain at which the constant power  $ILO$  is operated, then the actual input power can be enhanced or diminished by a factor  $f$  bounded by the following limits:

$$f_{\pm} = \left[ 1 \pm (RG)^{1/2} \right]^2 \quad (3.2-1)$$

Figures 3.2-2d and 3.2-2e illustrate the case of maximum phase change. The phase angle of the actual injected signal relative to the phase of the intended input signal is bounded by these limits:

$$\psi_{\pm} = \left| \pm \sin^{-1} (RG)^{1/2} \right| \quad (3.2-2)$$

The limits  $f_{\pm}$  and  $\psi_{\pm}$  are readily determined in practice because they depend only on scalar quantities,  $R$  and  $G$ . To determine the actual values of  $f$  and  $\psi$  requires knowledge of the phase of the circulator return loss and the phase of the amplifier gain.

The power limits  $f_{+}$  and  $f_{-}$  are plotted as a function of circulator return loss on dB scales in Figure 3.2-3a for a gain of 3 dB and in Figure 3.2-3b for a gain of 10 dB. The phase limits  $\psi_{+}$  and  $\psi_{-}$  are plotted in Figures 3.2-4a and 3.2-4b for these same two gains. Figure 3.2-5a shows power combining loss of a two module combiner versus the phase difference  $\psi$  between the two modules. A  $(1 - \cos \psi)/2$  law has been assumed. Figure 3.2-5b shows in greater detail the low angle portion of this curve.

The pairs of curves presented in Figures 3.2-3a and 3.2-3b indicate the range of possible enhancement or reduction of the nominal input signal power to

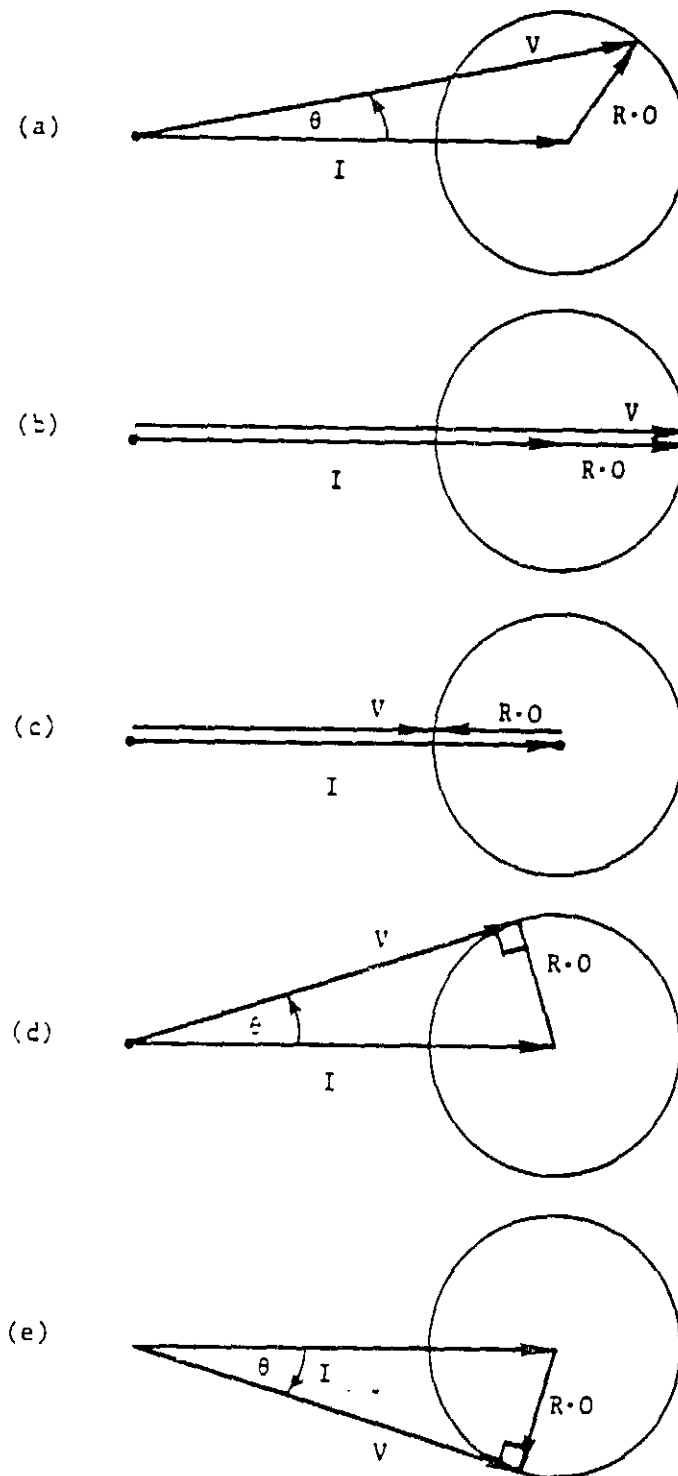


Figure 3.2-2 Diagrams showing the vector addition of the amplitude of the intended input signal  $I$  and the constant-amplitude reflection  $R \cdot O$  to produce the actual input signal amplitude  $V$ : (a) general case, (b) and (c) maximum and minimum input signal amplitude limits, (d) and (e) maximum limits of phase variation.

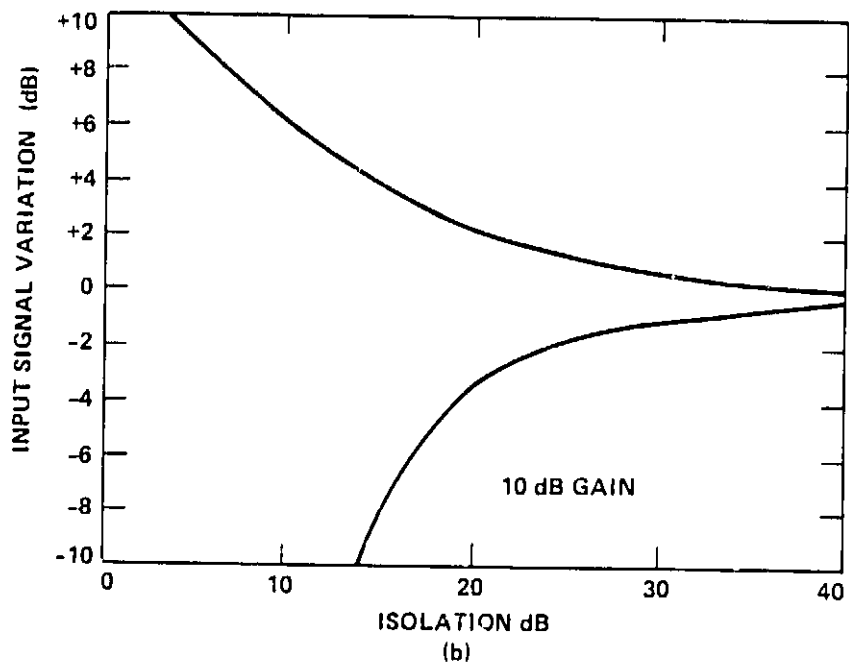
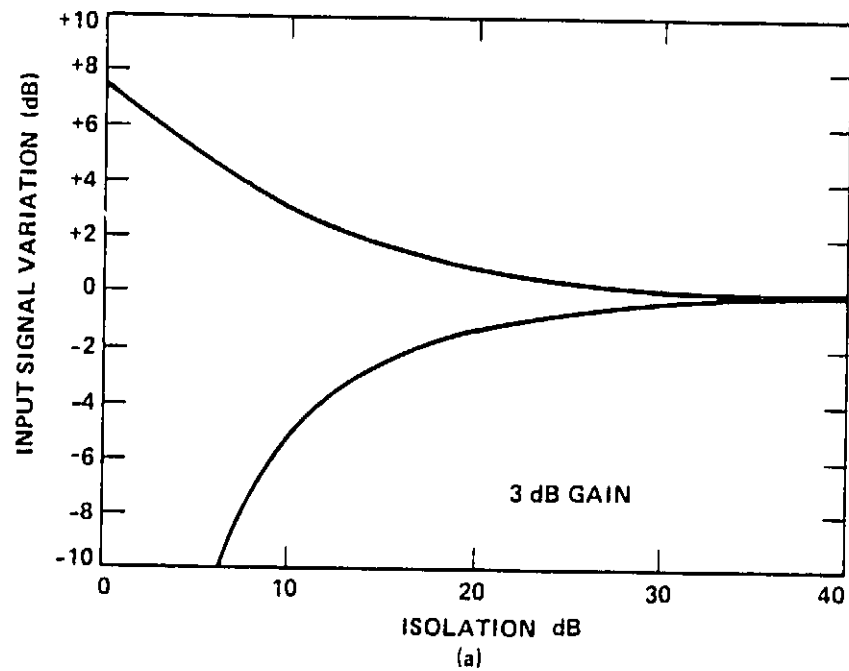


Figure 3.2-3 Plots of the upper and lower limits of the required locking range for a reflection amplifier ILO as a function of the isolation of a power combiner hybrid. (a) 3 dB nominal gain, (b) 10 dB nominal gain.

a one-port reflection amplifier which can be caused by the indicated return loss of the circulator. Therefore, a finite return loss implies that in order to ensure suitable operation of the one-port reflection amplifier module when it is placed on the circulator, that module should be able to operate, over the required frequency band, over the full indicated input power range associated with the corresponding return loss of the circulator. Figures 3.2-4a and 3.2-4b indicate the range of phase variation which is possible due to the finite return loss of the circulator. When uniform unit-to-unit phase matching is required, these curves indicate the maximum allowable return loss which will ensure operation within the indicated phase limits.

For example, Figure 3.2-3a indicates that for an ILO having a nominal gain of 10 dB operating on a circulator having a 20 dB return loss, the module should have the ability to operate across the required band with a +2.5 dB to -3 dB input power range about the nominal 10 dB gain level to ensure that it will operate on the circulator. Figure 3.2-4a indicates that the same 10 dB gain ILO and 20 dB return loss circulator can have a phase variation within the limits of  $\pm 18$  degrees. Two such modules in a combiner could differ from each other by as much as  $36^\circ$ .

Figure 3.2-5 shows that a power combining loss of 10 percent would occur in this case. Load isolators, if present, would dissipate the lost power. Otherwise the power could appear as reflected power at the module inputs, and the preceeding stage could see a badly mismatched load even if the circulators have excellent return loss at the input port.

There is always a limit to the range of input power over which an ILO will operate. Too large an input signal will cause spurious outputs. An input signal too low in power will cause unlocking. The 5.5 dB range of the example is probably wider than what the typical millimeter-wave IMPATT ILO having a nominal 10 dB gain, 5 percent bandwidth can tolerate. If this is the case, then the need for a circulator having a lower return loss is indicated.

For narrow-band amplifier requirements, the reflection amplifier module often can be made to operate into a circulator having poorer return loss than the figures indicate. For sufficiently narrow-band operation, the phase of the

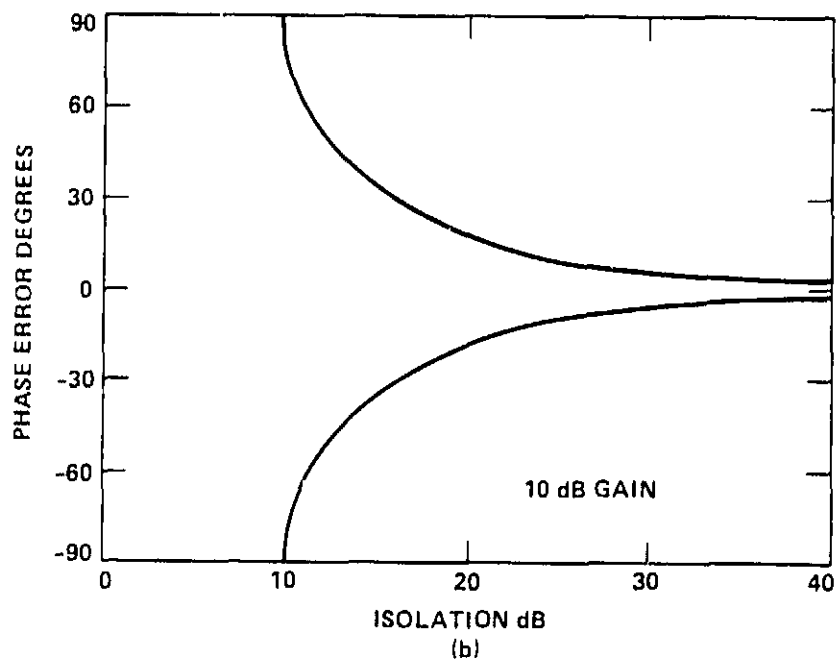
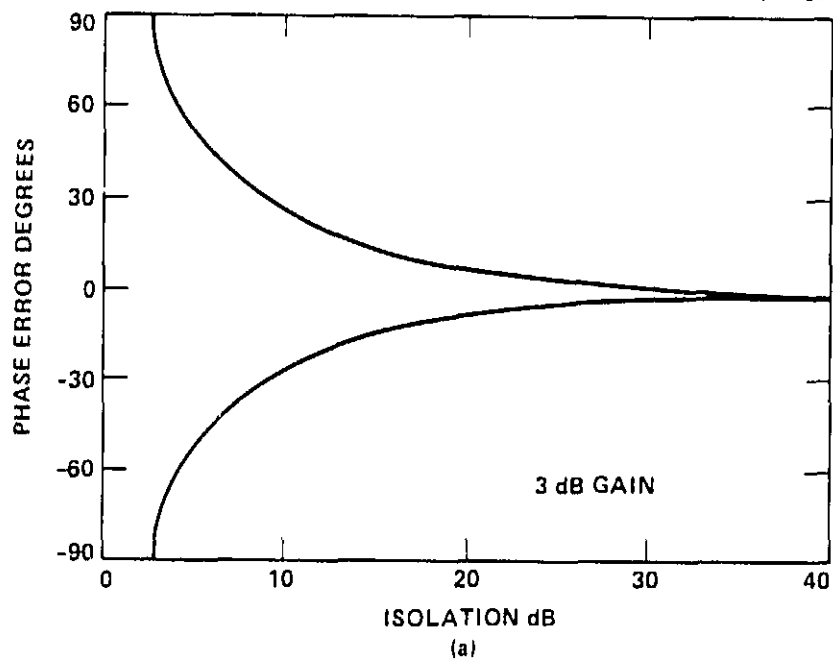
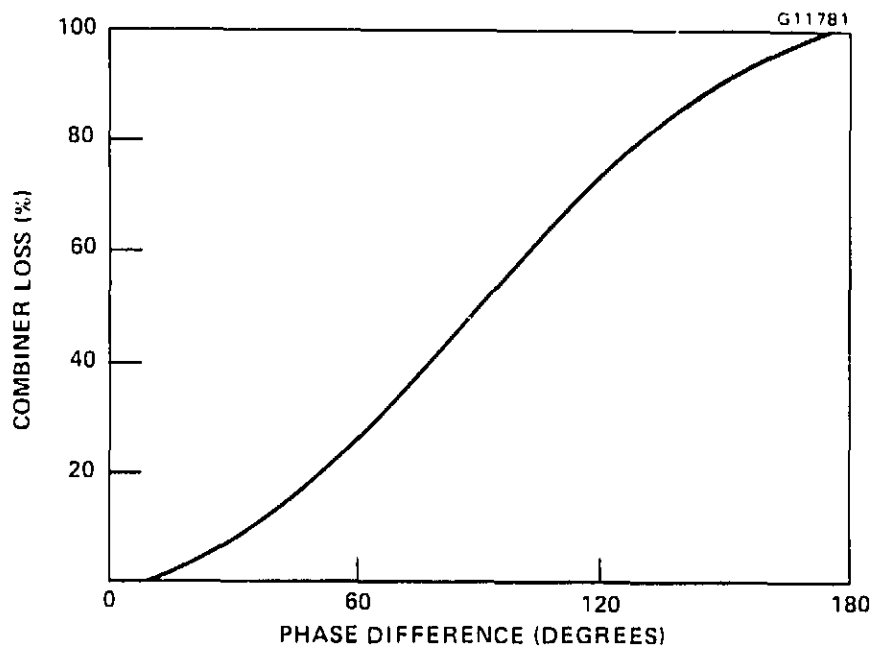
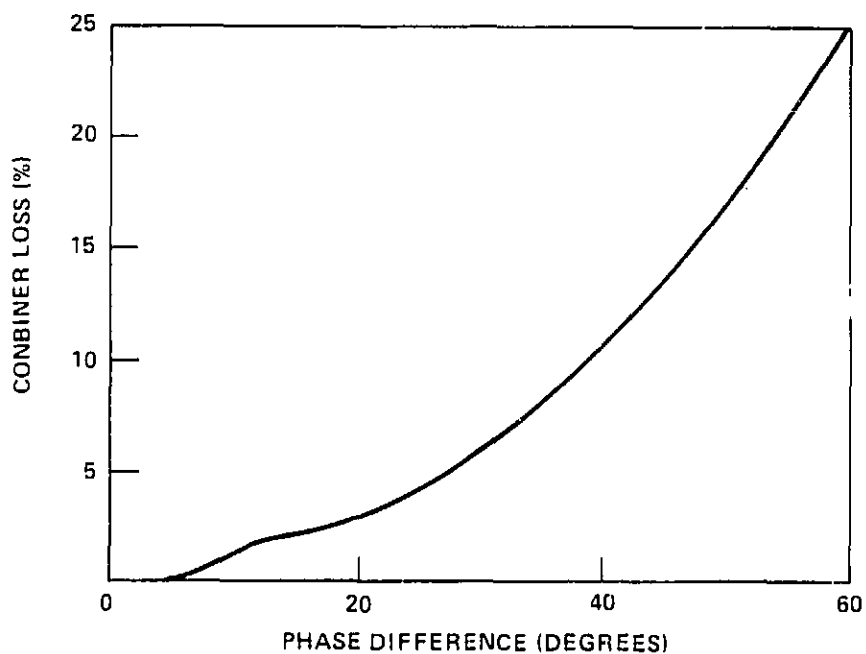


Figure 3.2-4 Plots of the upper and lower limits of the phase error of a reflection amplifier due to isolation in a hybrid power combiner (a) 3 dB gain, (b) 10 dB gain.



(a)



(b)

Figure 3.2-5 Power combining loss for a two-module power combiner versus phase mismatch of the two modules (A  $(1-\cos\theta)/2$  function is assumed.): (a) 0 to 180° x-axis, (b) 0 to 60° x-axis.



reflected signal will have less total variation across the band, and the entire range of amplitudes and phases between the limiting curves will not occur. In this case, it may be possible to make some after-the-fact tuning adjustments to the ILO module, including varying the length of line between the circulator and the ILO reflection amplifier to get the amplifier to function in a satisfactory manner. However, for amplifiers of wide bandwidth, and where amplifiers closely matched in phase are required, these restrictions on the return loss of the circulator should be applied.

### 3.3 HYBRID COUPLERS

The limited maximum output power available from a single IMPATT oscillator creates the need for power combining of discrete reflection amplifiers to provide the higher power levels required for current millimeter-wave system applications. The N-way hybrid coupler is an effective means of combining moderate quantities of IMPATT devices at the module level. The inherently low insertion loss, good port-to-port isolation, broad bandwidth and moderate size of the hybrid combiner have made it an attractive choice for power combining IMPATT devices. This approach was selected for our high power output stages of the transmitter.

A schematic diagram of a single 3-dB hybrid-coupled combiner of two IMPATTs is shown in Figure 3.3-1. The characteristics of a 3-dB short-slot hybrid coupler can best be represented by a scattering matrix:

$$S = \frac{1}{\sqrt{2}} \begin{bmatrix} 0 & 1 & e^{j(\pi/2)} & 0 \\ 1 & 0 & 0 & e^{j(\pi/2)} \\ e^{j(\pi/2)} & 0 & 0 & 1 \\ 0 & e^{j(\pi/2)} & 1 & 0 \end{bmatrix} \quad (3.3-1)$$

The principle of operation is as follows: When a power source is connected in either Port 2 or Port 3, the power will split equally to Ports 1 and 4. If Ports 2 and 3 are connected by a pair of balanced power sources and a

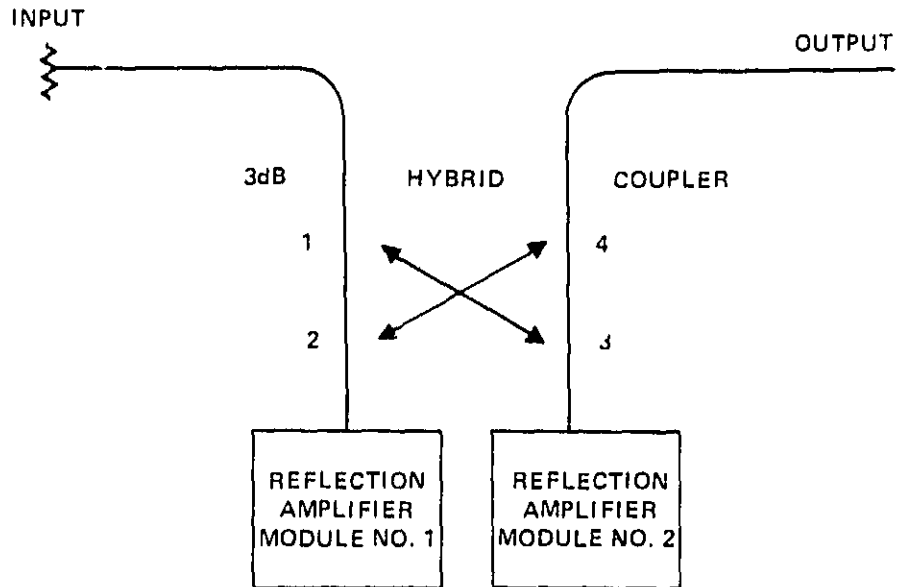


Figure 3.3-1 Schematic diagram of a two-module hybrid-coupled combiner.

proper phase relationship is provided between the two sources, the signals will be added in Port 4 but cancelled in Port 1. If the sources are unbalanced in amplitude or phase, a portion of the signal will be coupled to Port 1 and lost in the termination.

The output power of a 3-dB hybrid-coupled combiner is given by

$$P_o = \frac{1 + 10^{(D/10)} + (2 \cos \theta) \cdot 10^{(D/20)}}{2} \quad (3.3-2)$$

and the output phase angle is

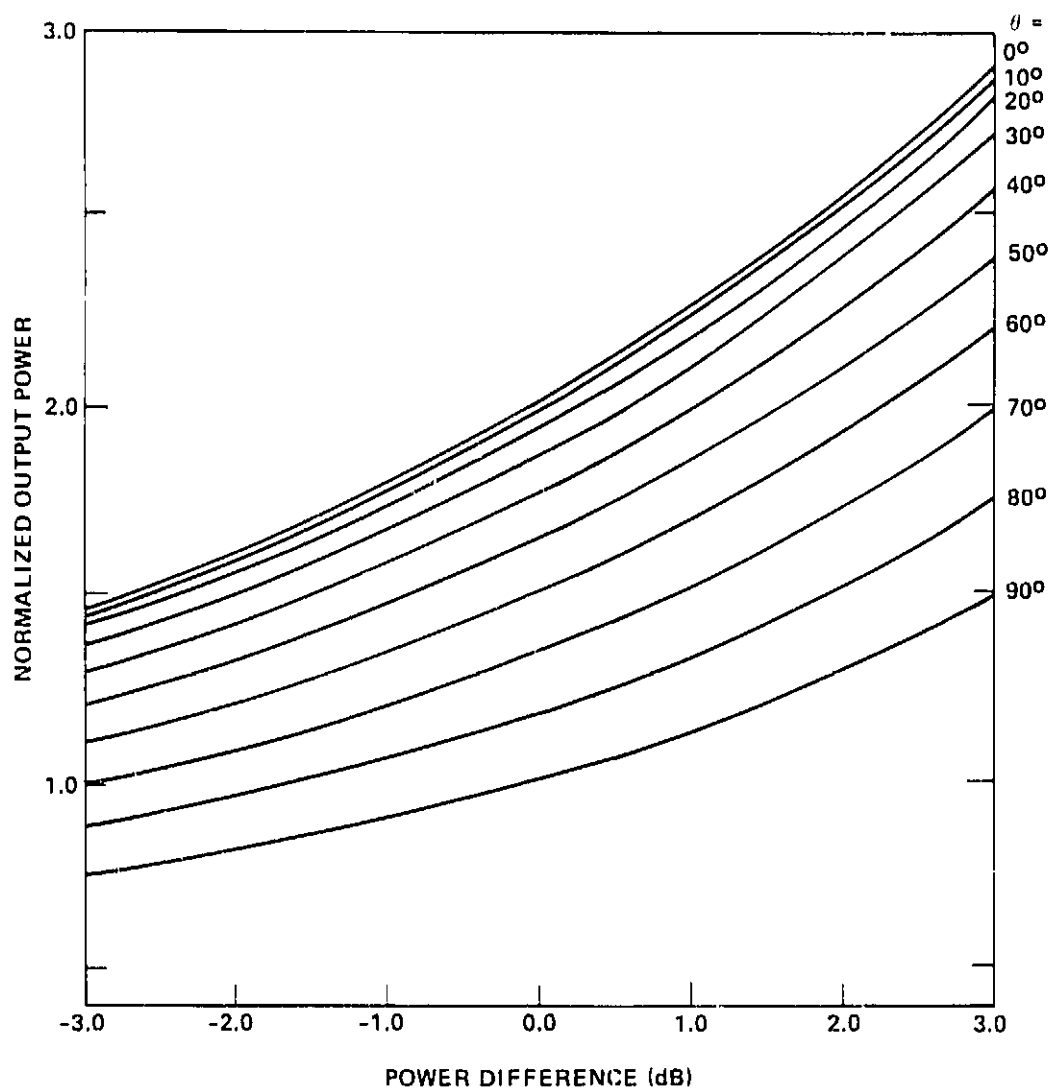
$$\theta_o = \tan^{-1} \frac{(\sin \theta) \cdot 10^{(D/20)}}{1 - (\cos \theta) \cdot 10^{(D/20)}} \quad (3.3-3)$$

where D is the power difference in dB and  $\theta$  is the phase deviation from the proper phase relationship required for optimum power combining of the two power sources. The combining efficiency from input ports to output port is given by

$$\eta = \frac{P_o}{P_{in}} = \frac{1 + 10^{(D/10)} + (2 \cos \theta) \cdot 10^{(D/20)}}{2 \left[ 1 + 10^{(D/10)} \right]} \quad (3.3-4)$$

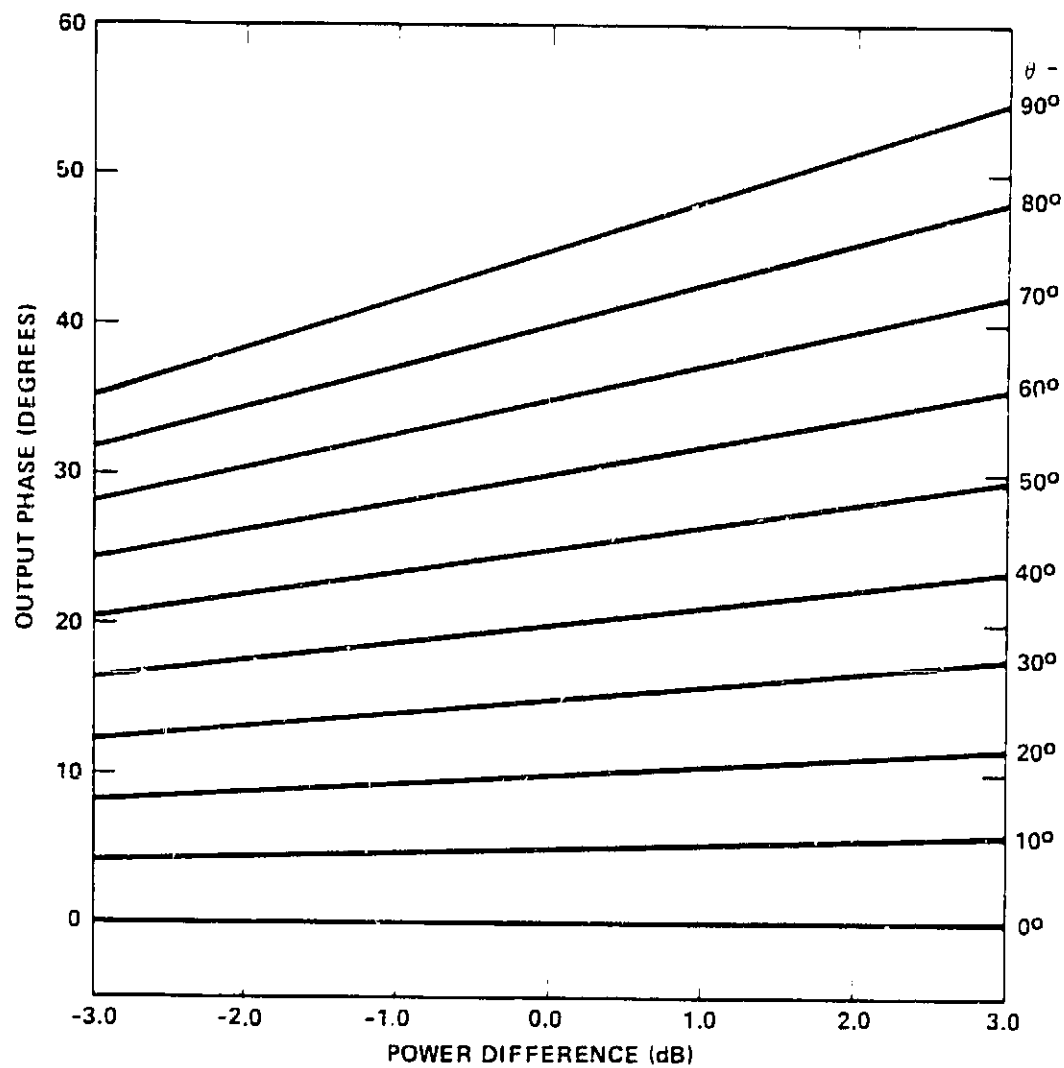
Figure 3.3-2 shows the output characteristics of a 3-dB hybrid-coupled combiner as a function of input power difference with the phase deviation as a parameter. The combining efficiency calculated using Equation (3.3-4) is plotted in Figure 3.3-3. Phase error is much more critical than amplitude unbalance of the sources for good combining efficiency. Higher than 90 percent combining efficiency can be obtained for a wide range of amplitude variation as long as the phase deviation is kept within 30 degrees. As the phase deviation increases beyond this value, the combining efficiency deteriorates rapidly.

The above analysis is based on the assumption that the 3-dB hybrid coupler is ideal and lossless. In a practical system, some amplitude and phase errors exist due to the nonideal characteristics of the hybrid coupler. The hybrid coupler also has some insertion loss. The hybrid-coupler combiner is often



(a) Output power

Figure 3.3-2 Output characteristics of 3-dB hybrid-coupled combiner.



(b) Output phase.

Figure 3.3-2 Continued.

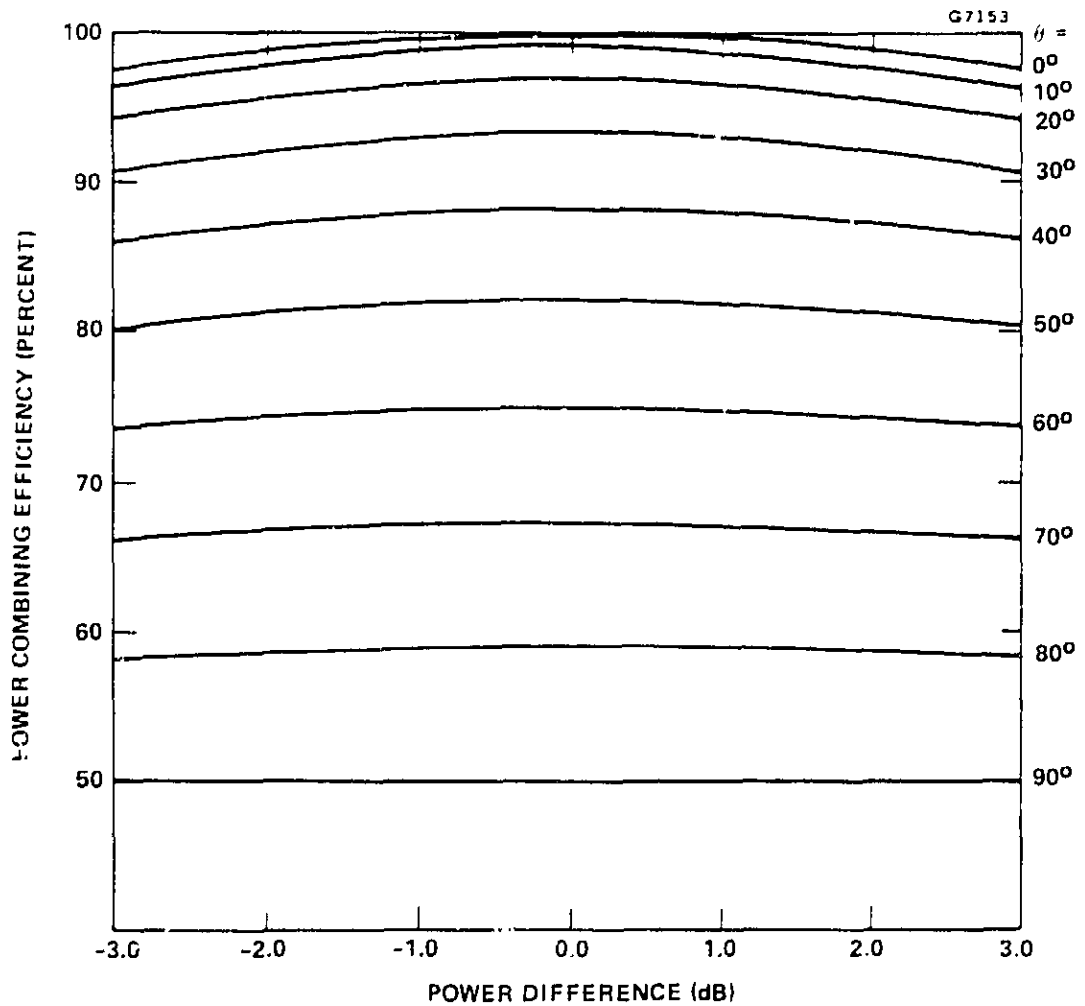


Figure 3.3-3 Power combining efficiency of 3-dB hybrid-coupled combiner.

operated in a table or injection-locked amplifier mode. In these modes of operation, the required amplitude and phase relationships are automatically satisfied when the incoming signal passes through the hybrid coupler.

Hybrid combined pairs of sources can be further hybrid combined. Consider now a symmetrical hybrid combined amplifier of K stages. The number of individual amplifiers required is

$$N = 2^K \quad (3.3-5)$$

The power added at the output of the combiner with each module having gain of  $G_i$  and power output of  $P_i$  becomes

$$P_{add} = 2^K L^{-K} \left( 1 - \frac{L^{2K}}{G_i} \right) P_i \quad (3.3-6)$$

Where L is the insertion loss associated with hybrid per path. It is seen for a lossy hybrid ( $L > 1$ ) and a finite module gain ( $G_i < \infty$ ) that the number of hybrid stages which can be combined is limited. The added power cannot be arbitrarily increased just by increasing K.

The hybrid coupler insertion loss poses an upper limit on the number of amplifiers that can be combined. Unfortunately, this loss increases with frequency. The hybrid-coupled approach is therefore not attractive for combining a large number of devices, especially at higher frequencies.

The key design consideration of a hybrid-coupled combiner is the symmetry of the 3-dB hybrid coupler as well as of the two IMPATT sources to be connected over the frequency range of interest. In the combiner development, therefore, attention must be focused on the adjustment of the hybrid coupler and the individual cavities to obtain proper tracking in amplitude, phase and frequency. As the number of devices increases, the difficulty in achieving the required relationship among sources also increases.

Module-level power combining of single-diode V-band IMPATT amplifier modules by means of 90-degree short-slot hybrid couplers was investigated earlier

in the program. In this module-level power combining study, reflection amplifier modules are individually set up and tested while mounted on a reference circulator. They are adjusted to operate in either the stable amplifier or the ILO mode of operation. Both modes are being studied in this transmitter development. Close matching in performance between the individually adjusted modules is critical. The excellent reproducibility of the silicon double-drift IMPATT devices and the uniformity which has been obtained in the components of the reduced-height waveguide circuit make it possible to produce well matched sets of reflection amplifier modules with little difficulty.

The 90-degree short-slot V-band hybrid couplers procured for this project are Model No. V605 from TRG Alpha Industries, Inc. Before any tests of power combining were made with these couplers, the couplers were individually characterized for VSWR, isolation, insertion loss and equal power split. The catalog specifications for these units are as follows:

VSWR - Maximum	1.15
Isolation - dB Maximum	20
Bandwidth - Percent	6

Actual evaluation of these units indicated that they perform well within specification.

In a number of cases in actual power combining tests, good power combining efficiency has been obtained; however, bandwidth is generally reduced from the wider bandwidth of the individual modules. For example, a pair of stable amplifier modules was prepared for power combining tests. These individual modules each operated at 5 dB gain ( $\pm 0.5$  dB), 4 GHz bandwidth, and 0.9 watts output power. On the two-module hybrid power combiner, gain remained about 5 dB ( $\pm 0.5$  dB), power output was 1.75 watts, while the bandwidth reduced to 2 GHz. Over the original 4 GHz band, power output rolled off to about -3 dB at the two band edges.

There is a second area in which performance was degraded in the power combiner.



In some cases, in isolated regions of the swept frequency band, bias oscillations were observed on the two modules, and these bias oscillations generally did not occur simultaneously on the two modules. When tested individually, no bias oscillations were present on the modules.

To gain a better understanding of some of these effects, hybrid couplers were used for module-level power combining in a different manner, i.e., in a 2-way divider/combiner scheme. The two module-level power combining schemes which both employ hybrid couplers are illustrated in Figures 3.3-4a and 3.3-4b. Figure 3.3-4a shows the scheme proposed for the present program, and this approach requires a minimum of hardware. Figure 3.3-4b shows the alternate scheme, 2-way divider/combiner which was evaluated for the purpose of gaining a better understanding of the problems associated with power combining by means of short-slot hybrid couplers. This scheme requires considerably more hardware, and for this reason it is probably an impractical one for many applications. The presence of the circulators in the latter scheme provides a degree of isolation to the amplifier modules beyond that of the hybrids alone. Otherwise, in this latter scheme, the hybrid couplers are dividing and combining power in a manner similar to the scheme in Figure 3.3-4a.

Tests of power combining by means of this approach utilizing the same pair of previously described modules gave the following results: 5 dB gain, 2.7 GHz bandwidth ( $\pm 0.5$  dB), and 1.5 watts power output. The reduced output power can be accounted for by the insertion losses of the additional components, circulators and additional waveguide sections required for connecting the various components. Also no bias oscillations were observed on either module.

The poor performance of the hybrid combiner shown in Figure 3.3 4a was suspected to be caused by the imperfect isolation of the hybrid coupler. However, no confirmation could be made at the time of the experiment. Later, with the analysis performed on the effects of finite return loss on reflection amplifier performance, it became all too clear that the limiting factor for broadband combining using the approach of Figure 3.3-4a is the 3 db  $90^\circ$  short-slot hybrid couplers. Approaches were sought to solve this problem of bandwidth limitation associated with the  $90^\circ$  short-slot hybrid couplers.

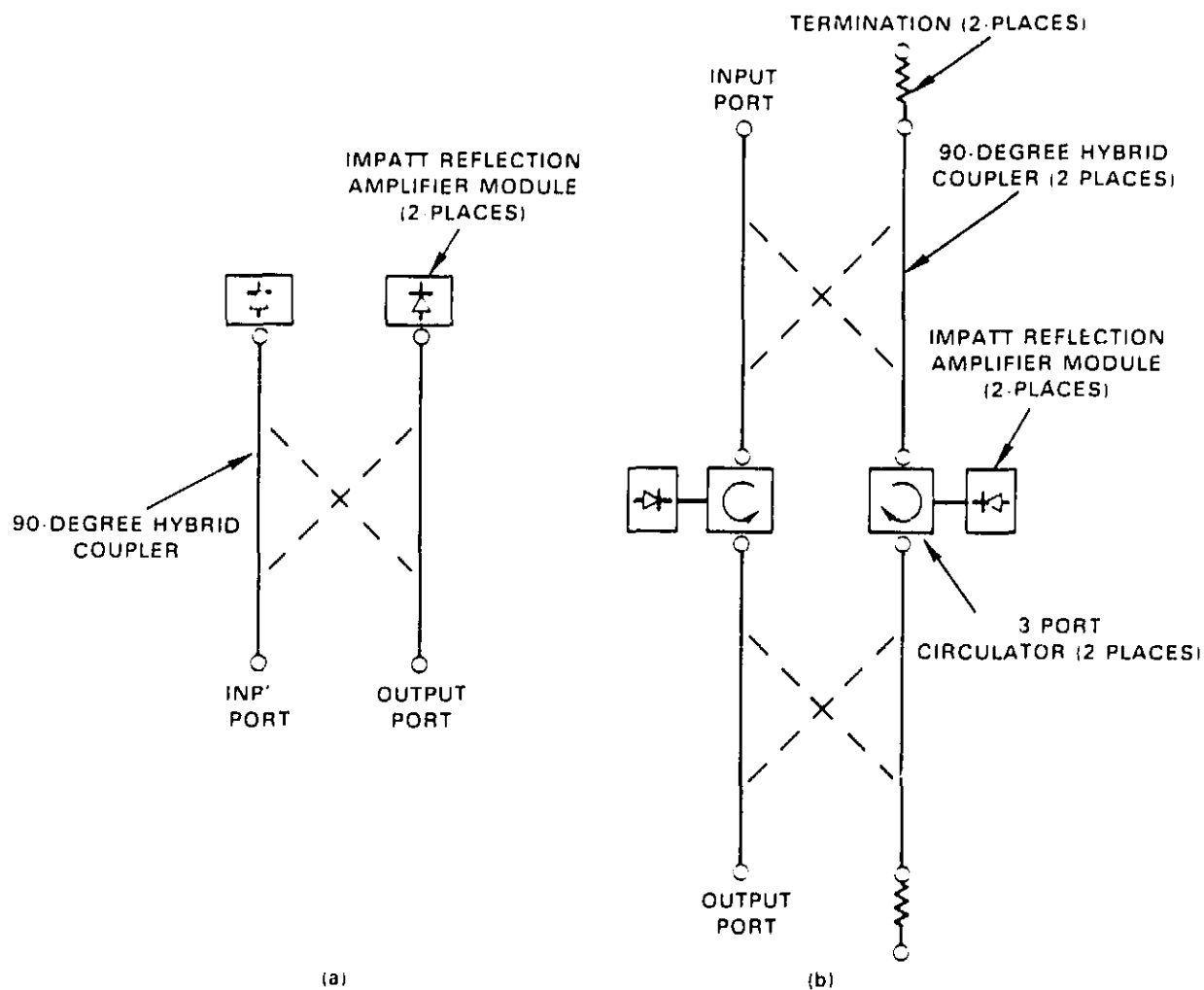


Figure 3.3-4 Two possible schemes utilizing 90-degree, short-slot hybrid couplers for module-level power combining a pair of reflection amplifier modules. (a) Combining with a single coupler. (b) 2-way divider-combiner scheme.

One possible approach is to undertake a program of  $90^\circ$  short-slot hybrid coupler development. The couplers procured for this program were obtained as catalog items from TRG Alpha Industries, Inc. It will be difficult to improve upon the design of the couplers by working with these devices, which were manufactured outside Hughes. Developing our own designs for such a coupler is possible, but it would require many months' time, because a long turnaround time would be needed to prepare drawings for and procure the machining of parts; and because the requirement for several design and evaluation iterations is anticipated. Also, it is uncertain that substantial improvement in the performance of the short-slot coupler can be obtained under any circumstances. While the development of an improved short-slot coupler was not dismissed entirely, it was not seriously considered until other approaches were first evaluated.

There are alternatives to the use of  $90^\circ$  short-slot hybrid couplers for module-level power combining. Use of the  $180^\circ$  or Magic Tee hybrid coupler was considered. An examination of published catalog data of millimeter-wave waveguide components indicates that matched Magic Tee couplers have a much wider bandwidth than  $90^\circ$  short-slot couplers. At first look, a disadvantage to the use of the Magic Tee coupler in combining two modules is that a circulator is required, while with the  $90^\circ$  coupler no circulator is required. However, by means of a newly developed and very simple technique, efficient, wideband power combining of two amplifier modules by means of one of these Magic Tees and without a circulator was demonstrated on this program. Also, this new technique can be extended in a direct manner to the module-level power combining of four matched amplifier modules without any circulators.

This development is very significant for its several important advantages in module-level power combining:

1. It allows, without the need for a circulator, the use of the high performance, commercially available coupler, the Hughes  $180^\circ$ -degree Matched Hybrid Tee, which has significantly greater bandwidth than the short-slot coupler.

2. When extended to the module-level power combining of four or more units, the technique result is a simpler configuration than the case in which short-slot hybrid couplers would be used.

The configuration which has been demonstrated is shown in Figure 3.3-5. The 180-degree Matched Hybrid Tee coupler is effectively transformed into a 90-degree coupler, thereby eliminating the need for a circulator, by the addition of a quarter-wave section of line on one of the symmetric ports of the Magic Tee.

This technique of module-level power combining by means of the Magic Tee and a quarter-wave section can readily be extended to the combining of four modules, as shown in Figure Figure 3.3-6. In this case, still one single quarter wave line section is required for combining.

Excellent results were achieved using the Magic Tee approach for power combining. Better than 90 percent combining efficiency was achieved for both the two-diode and four-diode combiners, as shown in Figure 3.3-7 for the two-diode and Figure 3.3-8 for the four-diode combiner. Better results were obtained later and will be shown in the following sections.

#### 3.4 10-CHANNEL CURRENT REGULATOR

Each of the IMPATT devices in the transmitter configuration must have a separate power controller, or current regulator, to maintain stability of operation and to provide a means for independent adjustment of the bias power for each device. The 10-channel current regulator design is based on the LM 117 HVK monolithic IC, three-terminal adjustable voltage regulator. This device provides excellent regulation with as low as a 3.5 volt input-output voltage differential (thus minimizing internal dissipation), and it can be connected to operate in either the constant-voltage or constant-current mode. Current limiting and over-temperature protection circuitry are built into the LM117 to prevent destruction of the device in the event of associated component failures.

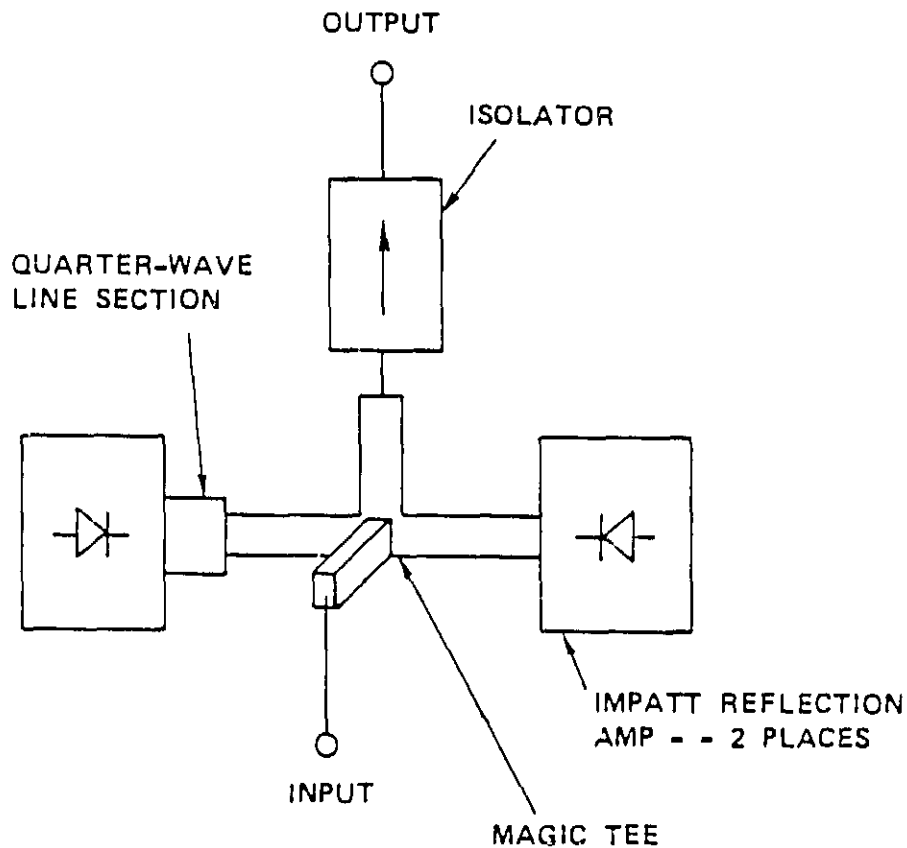


Figure 3.3-5 Configuration for the module-level power combining of a pair of matched IMPATT reflection amplifier modules using a 180-degrees hybrid coupler (Magic Tee) and a quarter-wave length of line. No circulator is required.

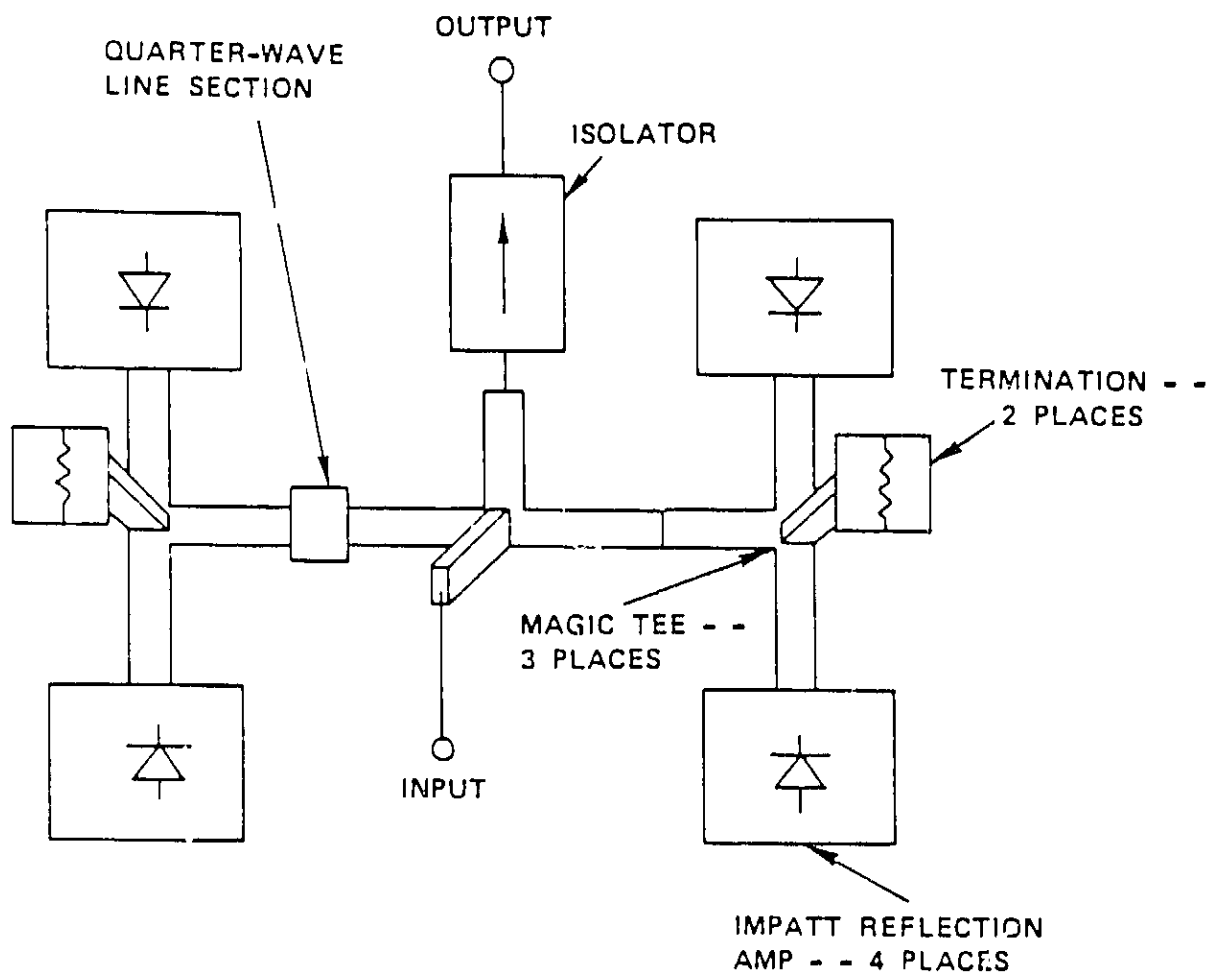


Figure 3.3-6 Configuration for the module-level power combining of four matched IMPATT reflection amplifier modules using three 180-degree hybrid couplers (Magic Tees) and a quarter-wavelength of line. No circulator is required.

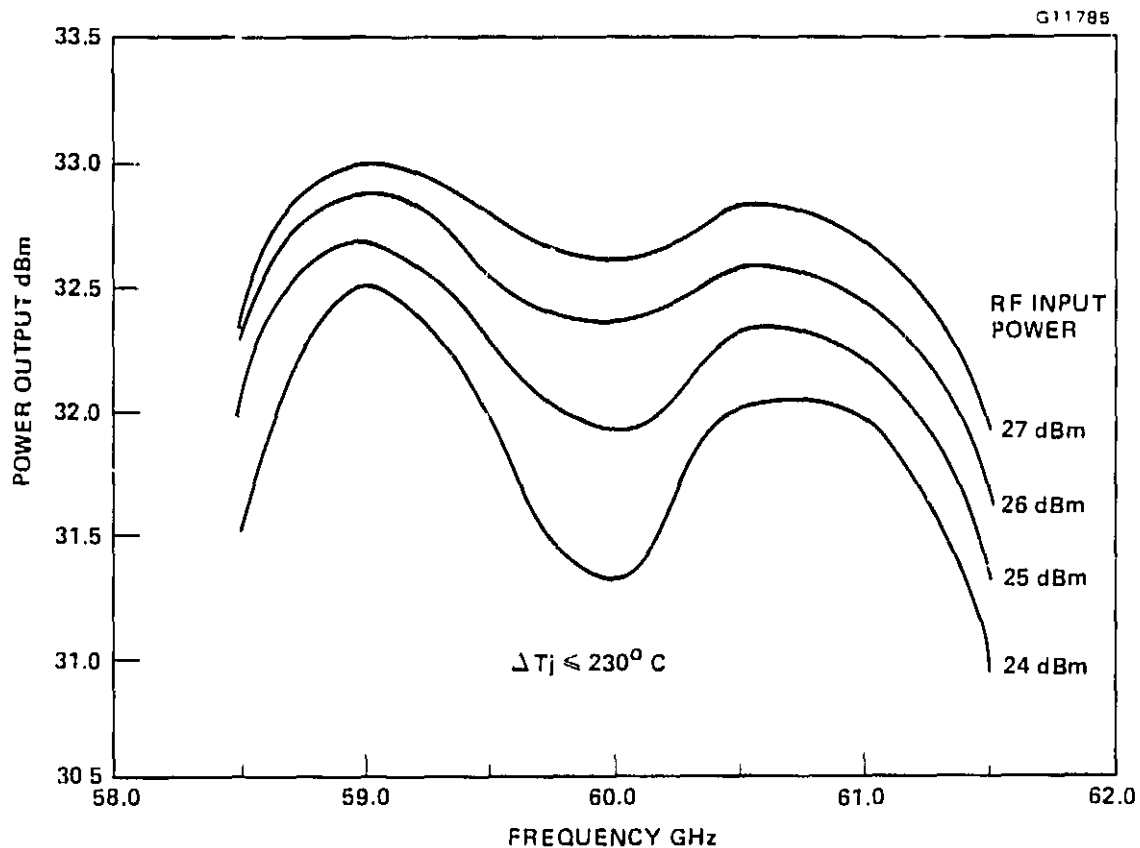


Figure 3.3-7 Power output versus frequency of the two-module module-level power combiner based upon the configuration shown in Figure 3.3-5. A matched Magic Tee and a quarter wave length of line were used without the need of a circulator.

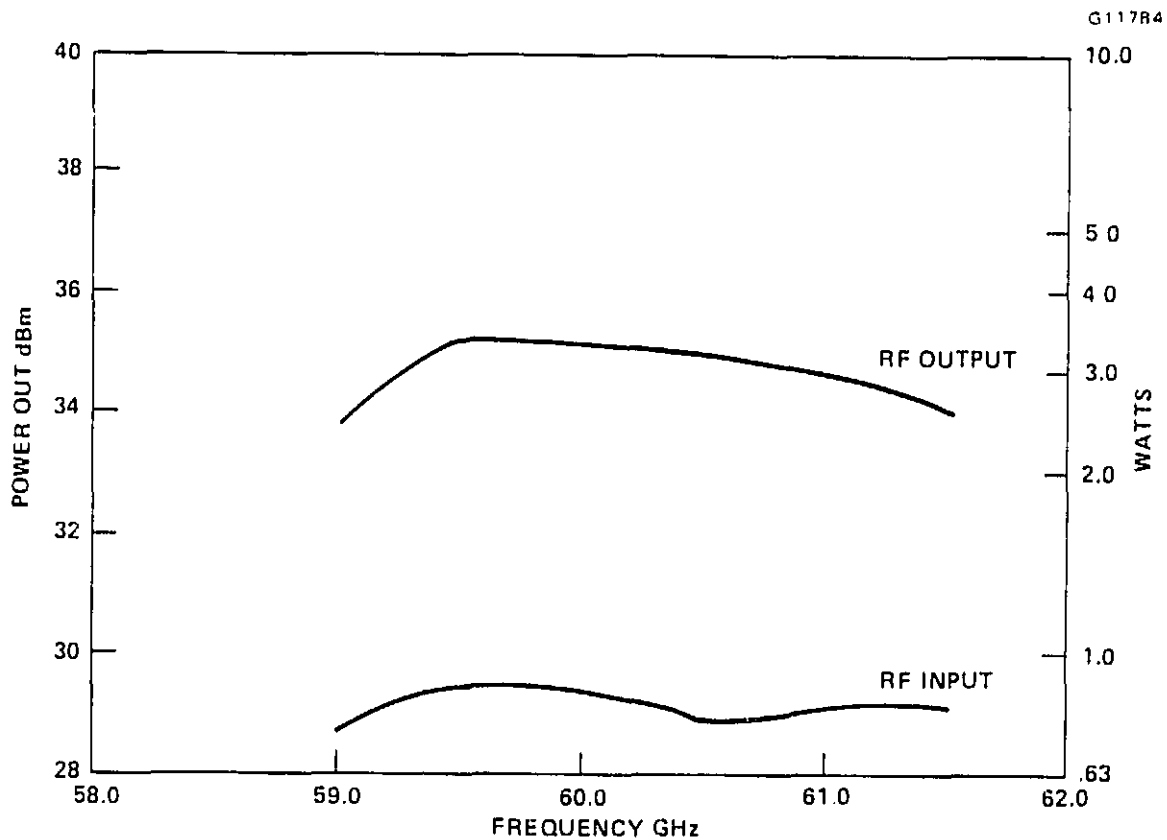


Figure 3.3-8 Output power versus frequency of the four-module module-level power combiner which is being developed to form the output stage of the solid state V-band transmitter.



A schematic of a simplified circuit for employing the LM117 for constant-current biasing of IMPATTs is shown in Figure 3.4-1. A potentiometer is included to allow adjustment of the IMPATT current over a 0.3 to 0.5 amp range.

While the basic regulator circuit shown in Figure 3.4-1 will provide excellent regulation of IMPATT current, the 10-channel current regulator contains supplementary protection and monitoring circuits. A schematic diagram of the 10-channel regulator is shown in Figure 3.4-2. The monitor circuits include a provision to monitor the current and voltage of any of the individual IMPATT devices from front panel jacks without disturbing any of the IMPATT bias lines. A 10-position rotary switch selects any one of a set of 10 10-to-1 voltage dividers and 0.10 ohm shunts for monitoring the voltage and current. All 10 channels can be scanned within a matter of seconds by switching through the 10 positions of the switch. In the unlikely event of an IMPATT failure, an associated failure indicator red LED will light on the front panel. This condition can be confirmed easily using the I-V monitor feature.

#### 3.4.1 Protection Circuits

Protection circuits are built into the power supply to protect against abnormal operating conditions at the dc input bus and at the dc regulator outputs. The dc input voltage bus is monitored, and if an abnormally low input voltage is detected, the power supply will turn off. The power supply will automatically turn on when the dc input voltage returns to a voltage above the lower limit and the ON command is present.

The dc voltage regulators have the fold-back overcurrent protection to prevent excessive current from being drawn from the dc power bus in the event of a short circuit or partial short circuit at the regulator outputs. The current fold-back in the regulators will reduce the power consumed by the power supply in the event of a short circuit or partial short circuit. This protection will isolate the failure from the rest of the power supply, and other regulator outputs will not be affected. In addition, an open circuit load to the regulators will not result in damage to the other regulators. The current regulator

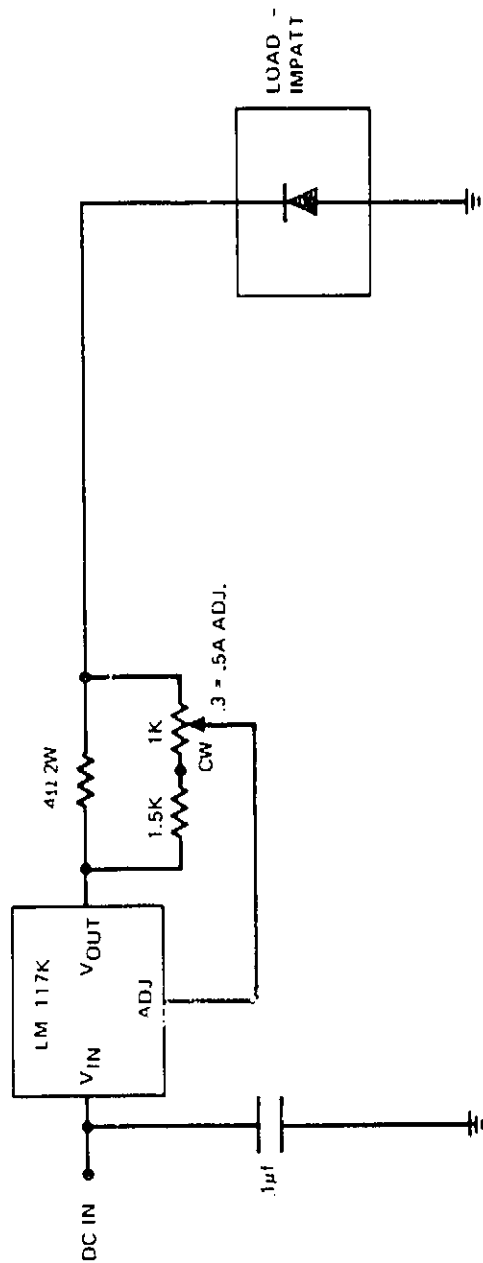


Figure 3.4-1 Schematic diagram of basic circuitry required to operate the LM 117 regulator IC in the constant-current mode.



will provide a constant current into a short circuit and operate with no damage with the output open circuits.

These load failures at the outputs of the linear regulator can result in load changes at the dc-to-dc converter. The DC-to-DC converter will have overcurrent protection for excessive load currents and provide no degradation in regulation at one regulator load. Furthermore, no damage will result at no-load operation.

#### 3.4.2 Monitor Circuits

The telemetry circuits provide operating voltage and current measurements of the linear dc regulator outputs. Normal voltage and current readings can be established, and, in the event of a regulator load failure, this fault condition will be evident in the voltage and current monitor outputs.

### 3.5 TEST EQUIPMENT

Earlier on in the program, it was recognized that two key pieces of test equipment will be required to facilitate the development of the amplifiers. The first is a high-power swept frequency source for the development of the high-power amplifiers/combiners and the second is a high-performance down-converter for making high-resolution spectrum analyzer measurements. This test equipment is used in the basic V-band test station shown in Figure 3.5-1.

#### 3.5.1 High Power Swept Frequency Source

To observe the output response of the amplifiers under various gain conditions, a swept frequency source that has various constant power levels is required for high-power stages of the transmitter.

A leveled sweep generator is one of the most basic and indispensable test equipment items used for the general development and testing of amplifiers. This type of equipment has been constructed under this program. The frequency determining device in the 1.0 watt V-band sweeper which has been constructed is a bias current tuned IMPATT oscillator. This single-diode device has

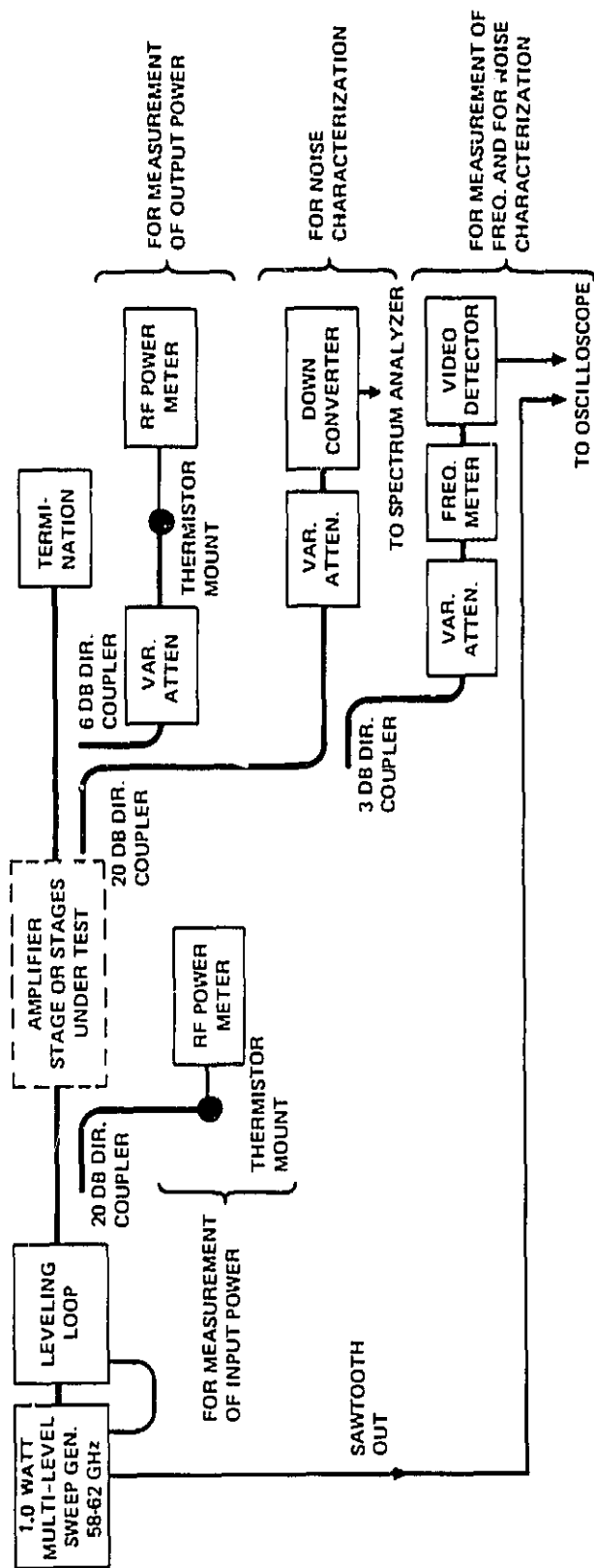


Figure 3.5-1 Block diagram of V-band waveguide amplifier RF test station not including provisions for phase measurements.

an output power of about 20 milliwatts. To bring this sweeper power up to the 1.0 watt level, four wideband IMPATT amplifier stages were constructed and placed following the low power sweep generator stage. This 1.0 watt sweeper has a bandwidth covering the 58.0 to 62.0 GHz range and it has an unlevelled power flatness of about  $\pm 0.5$  dB.

A ferrite modulator leveling loop is used for obtaining tighter leveling. When a ferrite modulator type of leveling loop is employed, the power output level of the leveled sweeper is adjusted electronically, normally by means of a reference voltage set by a potentiometer on the leveler control unit. Advantage can be taken of this feature for constructing an item of specialized test equipment that has proven to be particularly useful for the development of 60 GHz IMPATT amplifiers. When a given amplifier stage is being adjusted or aligned for operation, it is especially convenient if there is available a continuous oscilloscope display of the amplifier response over a frequency range which overlaps the full amplifier operating band, and for several different amplifier input power levels simultaneously. This multiple power level sweep feature is especially useful in the development of stable amplifiers, but it is quite useful also for the development of injection-locked oscillators. With this multi-power level sweep feature it is possible to observe simultaneously and continuously the effect that a tuning adjustment has on the amplifier response over a range of input power levels, and over the full frequency band of interest, as indicated by a display of a video detector output on an oscilloscope screen.

This multi-power level sweeper-leveler system shown schematically in Figure 3.5-2 was constructed on this program, by making a straightforward modification to the Hughes catalog version leveling loop system. The power output of the leveling loop is a monotonic function of a DC reference voltage which is normally set manually by a potentiometer located on the front panel of the leveler control box. Circuitry has been fabricated in which four potentiometers are supplied for setting as many different DC reference voltages each corresponding to a different RF power level. Logic circuitry controls analog switches to switch successively through these four DC reference voltages on the leveler for each successive sweep of the sweep generator. This V-

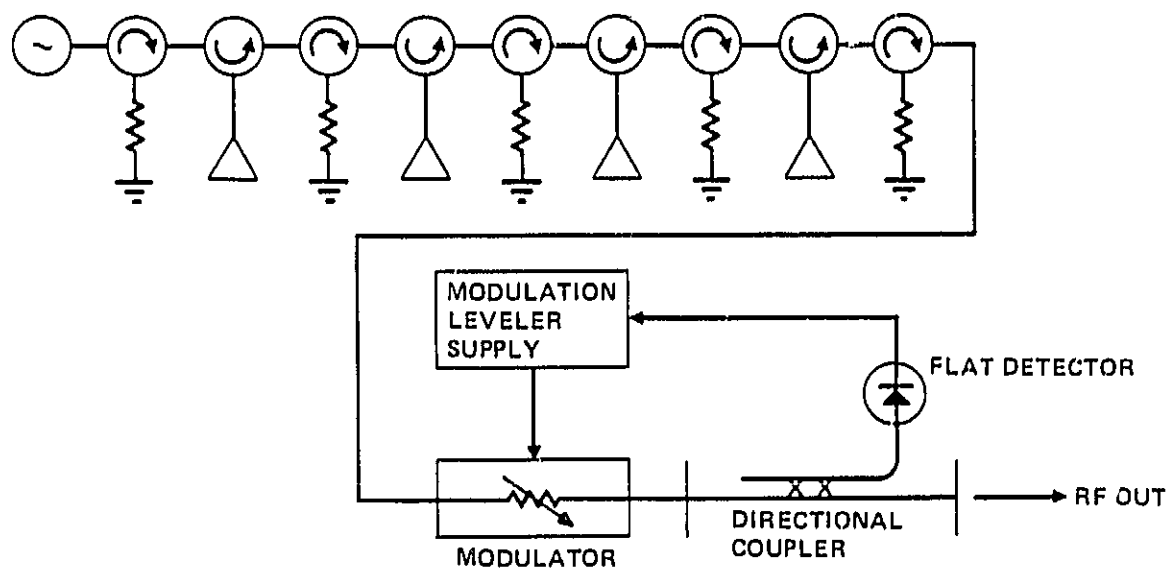


Figure 3.5-2 Multilevel sweep oscillator block diagram for IMPATT characterization.

band multi-level leveling loop system, along with the 1.0 watt V-band sweeper, was employed extensively during the amplifier development program.

### 3.5.2 Downconverter

This item of instrumentation is required for the characterization of noise and spurious outputs in the various amplifier circuits being developed. A downconverter was assembled for dedicated use on this program. A Hughes V-band balanced mixer, which is an item of capital equipment purchased specifically for use on this program, and a V-band klystron local oscillator are the major components of this downconverter. The system is shown in Figure 3.5-3. A spectrum analyzer with a preselector displays, on a single sweep with high sensitivity and without spurious mixer-generated lines, the entire downconverted 59.0 GHz to 61.5 GHz frequency band. This is the operating frequency range specified for the transmitter to be developed on this program.

Time and again, this high-resolution spectrum analyzer capability has proven to be a most important item of test equipment for this program. It has indicated existence of a problem: The circulator-coupled amplifier stages developed under this program exhibit serious spurious oscillations and noise previously undetected when only a spectrum analyzer harmonic mixer was used for these measurements. This downconverter-spectrum analyzer setup also indicated the existence of a second problem: At higher bias levels, the free-running IMPATT oscillator circuits also display a significant level of noise and spurious oscillations, even when operated into a wideband termination without a circulator. This noise, which is generally -35 dBc will usually remain undetected unless sophisticated spectrum analysis techniques are employed..



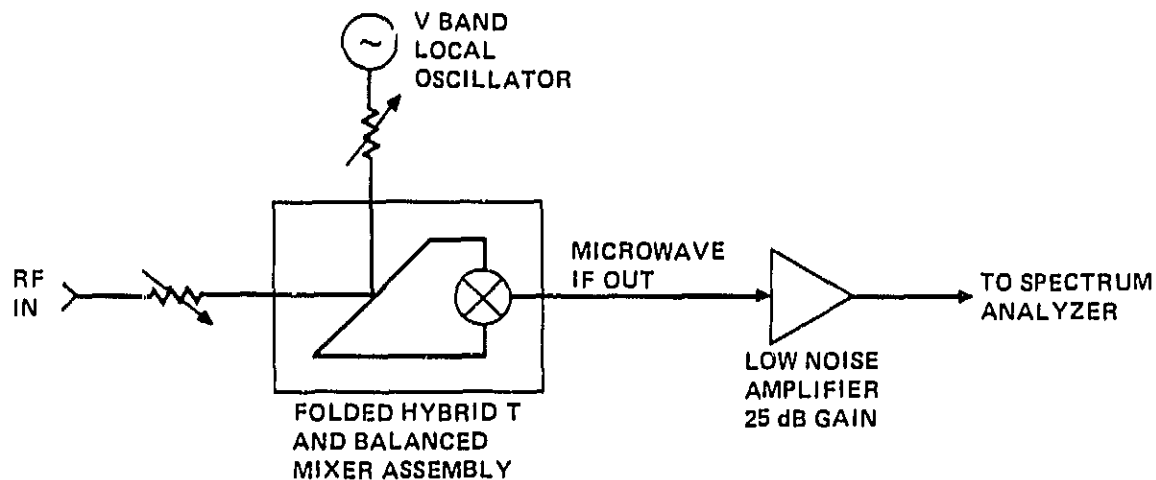


Figure 3.5-3 Down converter for characterization of noise and spurious output.

#### 4.0 SINGLE STAGE IMPATT AMPLIFIERS

The basic modes in which an IMPATT PF reflection amplifier may be operated are: the stable amplifier mode; the injection-locked oscillator mode (ILO); and a third mode observed during our circuit development, which we call the triggered oscillator mode. Figure 4.0-1 shows the basic operating characteristics of these various operating modes.

An IMPATT diode operated in the stable amplifier mode will exhibit the following characteristics:

1. Somewhat linear small signal gain.
2. Large signal gain.
3. Large signal gain compression.

This type of operation has relatively large bandwidth, modest gain and generally the lowest efficiency of the three modes.

An IMPATT diode operated in the injection locked mode will exhibit the following characteristics:

1. No small signal gain.
2. Constant output power.

This type of operation has narrower bandwidth, but has higher gain and efficiency than stable amplifiers. To eliminate unwanted oscillations when input signal is not present requires some method to remove the bias current.

An IMPATT diode operated in the triggered oscillator mode will exhibit the following characteristics:

1. No small signal gain.

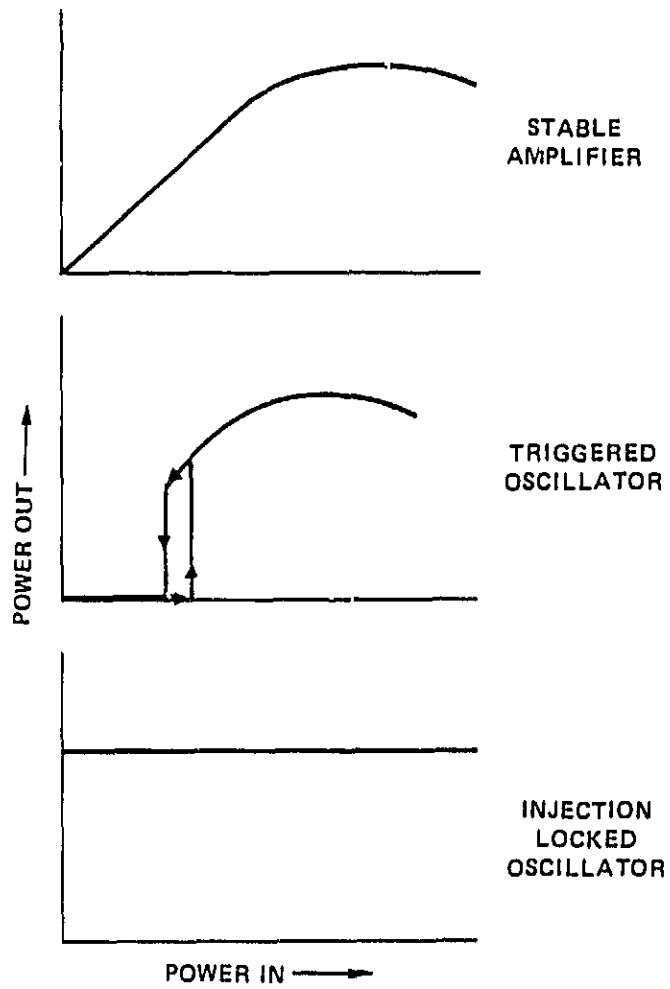


Figure 4.0-1 Reflection amplifier modes of operation.

2. Large signal linear gain over a limited input drive range.
3. Large signal gain compression.
4. No output with no input.

This type of operation has good bandwidth, higher gain than stable mode and medium efficiencies. This mode generally exhibits a hysteresis effect near threshold; that is, the oscillation requires a slightly higher input drive to turn on than to turn off. Amplifiers operating in this mode requires a minimum threshold input drive in order to trigger the onset of the mode, thus the term Triggered Oscillator.

The general circuit hardware required to operate a given stage in any of these modes is essentially the same. Normally, there are only minor differences in the tuning of the amplifier stage among these modes of operation. The effective load impedance presented to the IMPATT is adjusted to be slightly greater in the stable amplifier or triggered oscillator case to suppress free-running oscillations by adjusting the bias choke progressively away from the diode.

The negative resistance of a silicon double-drift IMPATT diode is in the 2-ohm range. The negative resistance exists over a very wide frequency range, typically an octave or more. As long as the circuit impedance presented to the diode at any frequency is greater than the negative resistance of the diode at that frequency the, diode operates as a stable amplifier. Gain and output power are given by Equations 4.0-1 and 4.0-2.

$$G = \frac{R_L + |R_D|}{R_L - |R_D|} \quad R_L > R_D \quad (4.0-1)$$

$$P = \frac{(V_S)^2}{2 R_L} \quad (4.0-2)$$

where

G = gain  
 $R_L$  = effective load impedance

$ R_D $	=	magnitude of the (negative) diode resistance
$P$	=	output power
$V_S$	=	output signal amplitude

As  $R_L$  decreases and becomes equal to  $R_D$ , gain goes to infinity and the diode begins to oscillate. The frequency of oscillation depends upon the diode and circuit reactances, which are not considered here.

A further reduction in  $R_L$  will cause the oscillations to grow until the nonlinear nature of the IMPATT diode causes the diode negative resistance to decrease in magnitude to match the circuit impedance. The power output of the oscillator is determined by the circuit impedance,  $R_L$ , and the impedance versus amplitude characteristic of the diode. High power is associated with low circuit impedance.

The maximum achievable value of the signal amplitude,  $V_S$ , is fixed by the IMPATT diode physics and is approximately one-third of the avalanche voltage of the diode. Once the diode is optimized for operation in a particular frequency band, the maximum value of  $V_S$  is fixed. The diode negative impedance,  $R_D$ , is fixed by diode physics and bias current. The mode of diode operation (either stable or injection locked) and the available power are determined by  $R_L$ .

In the triggered oscillator mode, the circuit load line,  $R_L$ , is adjusted such that it cuts sharply across the locus of the diode impedance. As the input RF power increases, the impedance of the diode changes. At the threshold point, which is also the crossover point of the diode impedance and the  $R_L$ , the diode breaks into oscillations. The triggered oscillations mode is what is generally referred to as the quasi-stable mode where the amplifier is operating at the semi-stable region of a stable amplifier.

The original approach to the development of the transmitter was to use injection locked oscillators to minimize the number of stages, thus reducing the size, weight and cost of the transmitter. However, it was found that at low to medium power levels, to achieve the necessary bandwidth, a stable amplifier has to be employed. The final transmitter configuration, as it

TABLE 4.0-1  
OPERATING MODE OF EACH OF THE  
AMPLIFIER STAGES IN THE V-BAND TRANSMITTER

Stage	Mode of Operation
1	Stable Amplifier
2	Stable Amplifier
3	Stable Amplifier
4	Stable Amplifier
5	Triggered Oscillator
6	Triggered Oscillator

was delivered, consists of amplifiers employing the stable and triggered modes of operation. As a result of the lower gain of stable amplifiers, six stages, rather than the originally proposed four stages, are required to achieve the 30 dB gain. Table 4.0-1 summarizes the operating mode of each of the stages.

#### 4.1 LOW POWER IMPATT AMPLIFIERS

Low-power IMPATT stable amplifiers were developed as drivers for the transmitter chain. As the program proceeds, the development of the low-amplifiers proved to be the most difficult among the driver, the medium-power and the high-power amplifiers.

At Hughes, our experience with low power IMPATT amplifiers has been mostly with silicon single-drift IMPATT diodes. Working either in the stable or injection locking mode, the amplifiers provide roughly the same output power over a fairly broadband. One of the problems with this type of amplifier, when tuned for high gain, is the large gain variation across the frequency band. For the specific low power amplifier on this program, the first stage of the amplifier chain must work with a normal RF input power level of 4 milliwatts. A single-drift IMPATT diode stage operating in the stable amplifier mode and having about 10 db gain has been constructed, but its bandwidth

is only about 1 GHz at the 1 db points. The response of such an amplifier is shown in Figure 4.1-1.

Retuning the circuit results in an amplifier having a double peak response with approximately the same gain. The gain response is slightly flatter than the previous amplifier over a bandwidth greater than 2.5 GHz as shown in Figure 4.1-2. However, in between the peaks, the gain drop is greater than 2.5 db, which again makes it unacceptable.

Stable Gunn device amplifier stages also have been under study as an alternative to the single-drift IMPATT for this stage. A 2.5 GHz bandwidth was realized at 10 dB gain in the Gunn device amplifier, but again the gain ripple is high, about 3 dB.

To minimize the gain ripple, improving the input dynamic range, the amplifiers are retuned for flat response, but at the sacrifice of lower gain. Figure 4.1-3 shows the flat response of the amplifier across the frequency band from 5.9 to 6.2 GHz, but the gain was reduced to 7 db from the original 10 db. Both single-drift and double-drift IMPATT diodes were used in the amplifier. They provide essentially the same performance, but the double-drift IMPATT diodes are slightly more efficient and therefore the operating temperature is lower for single-drift diode. For this reason, double drift diodes were used for this stage.

## 4.2 MEDIUM POWER IMPATT AMPLIFIERS

Medium-power IMPATT stable amplifiers producing 500 mW output power at 7 to 8 db gain are readily fabricated using Hughes silicon double-drift diodes. The circuit elements for these stages are essentially identical to the higher power output of the diode and operating currents are reduced to maintain high-efficiency operation.

In the final transmitter configuration, the input power range for spurious free operation of the output stage dictated some gain variation constraints for the driver stages. First, input drive level variations to the output stage should be minimal, generally requiring available gain to be sacrificed

4.10.2.4.

# RESPONSE OF LOW POWER STABLE IMPATT AMPLIFIER STAGE

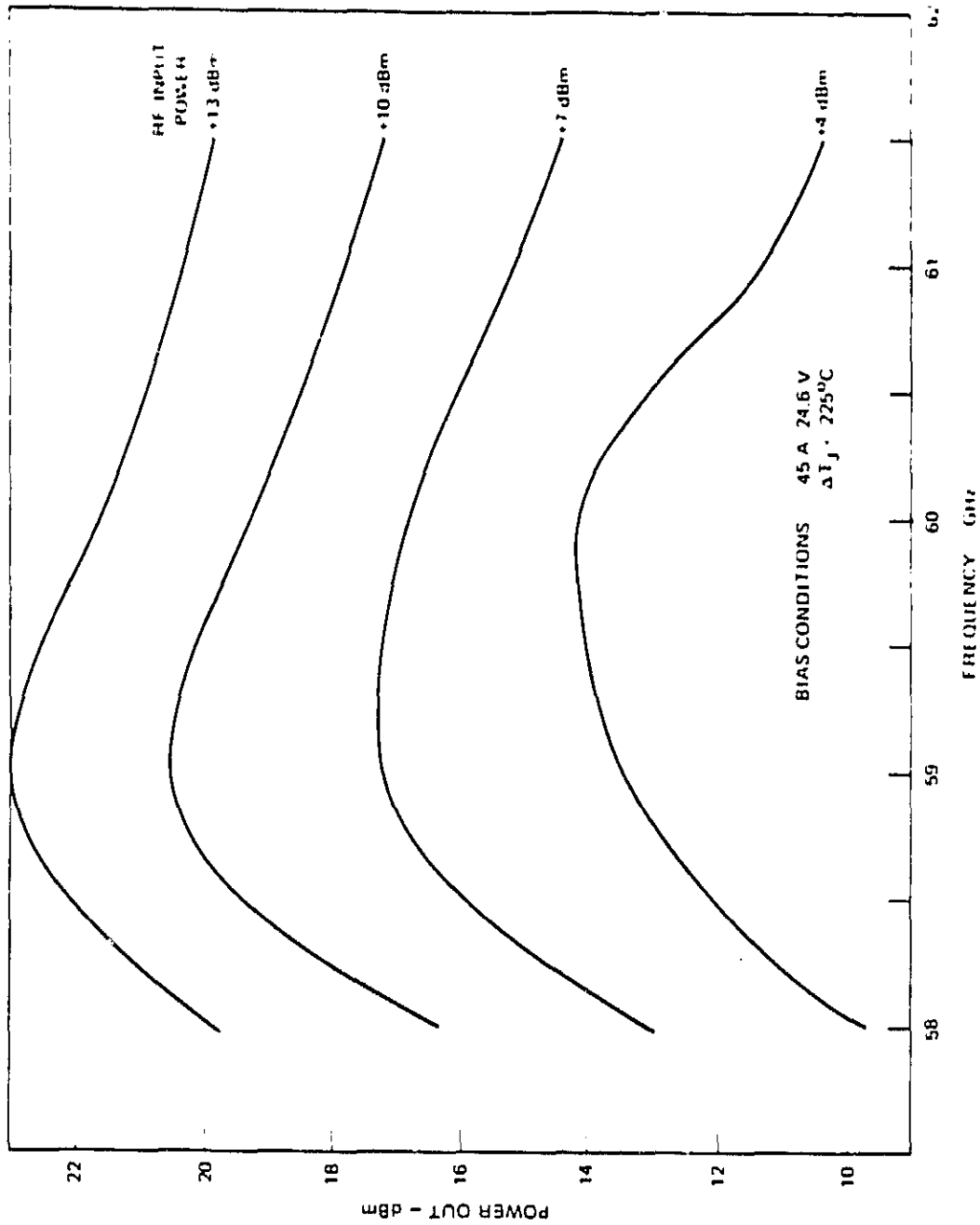


Figure 4.1-1 Response of low power 60 GHz wideband stable amplifier stage employing a single-drift silicon IMPATT diode.



G11789

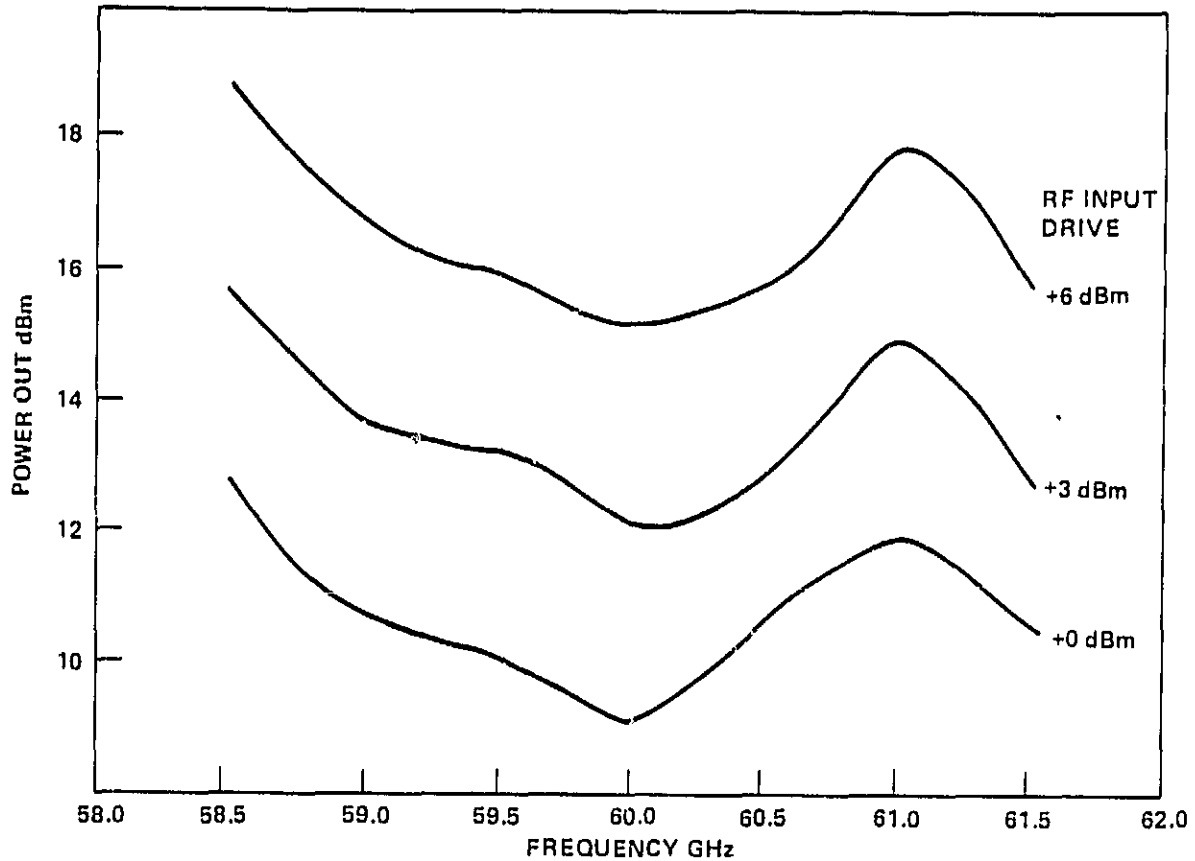


Figure 4.1-2 Low power IMPATT stable amp, with  
double peak response.

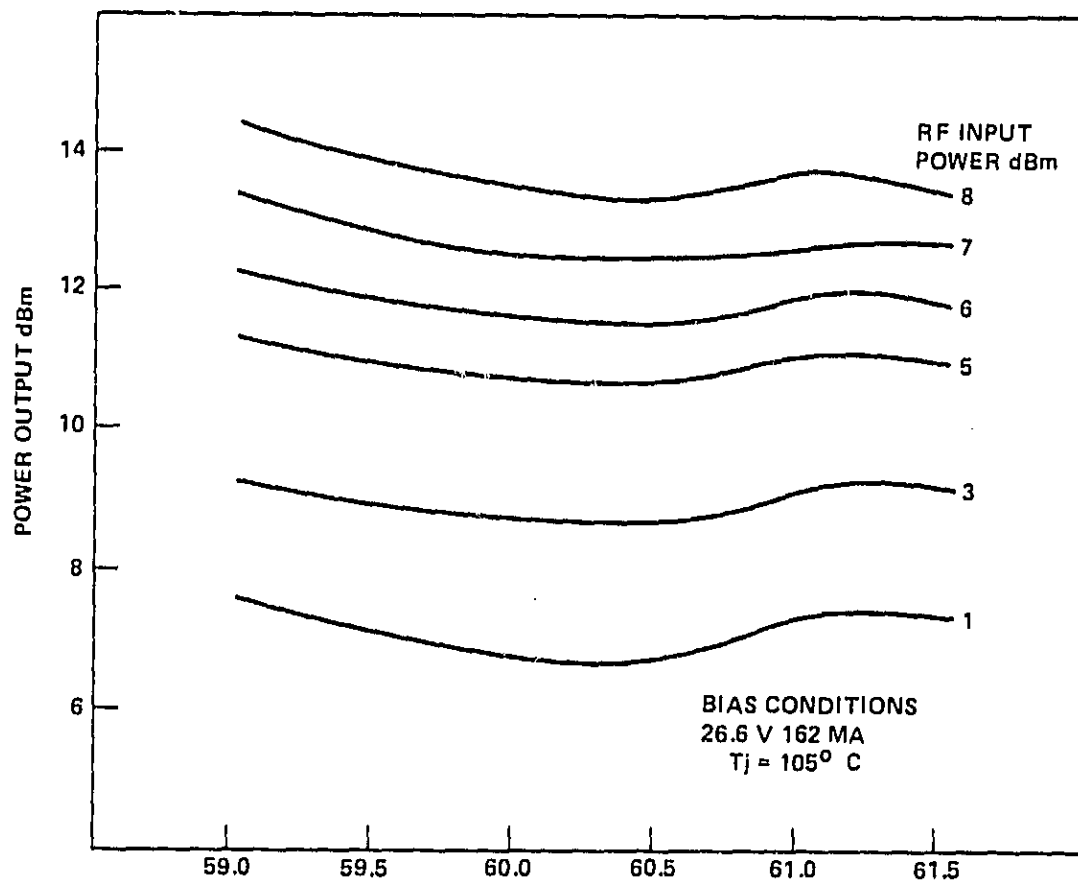


Figure 4.1-3 Driver first stage.

for gain flatness. Second, the stage is operated in gain saturation so that the output stages will not see variations in transmitter input power. Saturating the driver stage means lower gain and thus requires more stages to achieve the overall gain requirement.

Figure 4.2-1 is a graph of power out versus frequency for a typical medium power IMPATT amplifier. A bandwidth of 3 GHz at 7 db gain is indicated.

#### 4.3 HIGH-POWER IMPATT AMPLIFIERS

High-power V-band IMPATT amplifiers have been developed in previous programs with varying degrees of success. These amplifiers made use of both single-drift and double-drift IMPATT diodes developed at Hughes. Both stable and injection locked oscillators were developed.

For single-drift IMPATT amplifiers, the output power of the stable amplifier or ILO is typically 230 mW. It is relatively straight-forward to achieve reasonably broadband, e.g., 1-3 GHz, performance. For ILOs, the bandwidth is limited to less than 1 GHz. In either case, the circulator was the limiting factor in bandwidth performance. By replacing the circulator with a broadband directional coupler, bandwidth as high as 8 GHz has been observed.

For double-drift IMPATT amplifiers, the output power is generally in the 1.0-watt range. The bandwidth of the amplifier, operating in either the stable or ILO mode, was limited to less than a few hundred megahertz before the onset of spurious oscillations. It is believed that this limitation in bandwidth was caused by the highly nonlinear properties of the higher efficiency double-drift IMPATT structure which made circuit matching over a large dynamic range (small signal to large signal) a formidable task.

Our initial approach to the high-power amplifier was to use the ILO. The circuit to be used was a direct scaling of the highly successful broadband Q-band ILO. The circuits developed for the ILO have rather high gain per stage, generally 10 db or better; but in only exceptional cases did they achieve the required 2.5 GHz bandwidth requirement. The most serious drawback to these circuits was the occurrence of spurious responses of the ILOs.

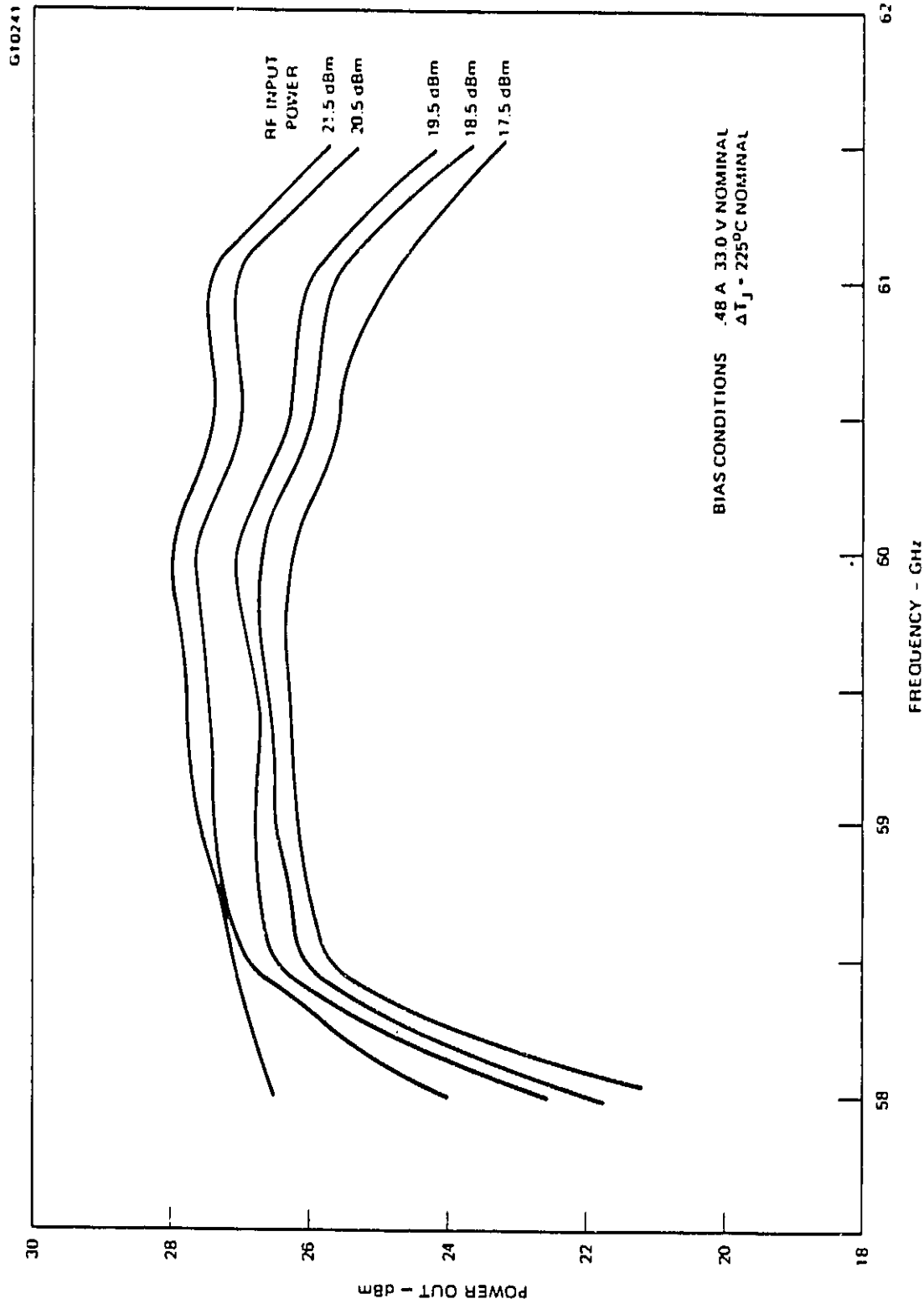


Figure 4.2-1 Response of medium power (0.5 watt) 60 GHz wideband stable amplifier stage employing a double-drift silicon IMPATT diode.

We were able to relate these spurious responses in the majority of cases to relatively higher in-band return loss responses of the circulators being used with the reflection amplifiers. The subsequent study of ferrite component requirements (Section 3.2) for reflection amplifier operation confirmed our observation that the high return loss of circulators was responsible for the in-band spurious responses. We also believed that a stable amplifier with its lower gain may help to relax some of the high return loss requirements. Our attention then turned to stable amplifiers.

It was observed that, by tuning the circuit with the precision fitted anodized bias choke to achieve lower gain, the bandwidth of the amplifier was vastly improved, and noise and spurious responses disappeared. When the gain of the amplifier was reduced to +3 db, the stage behaved as a stable amplifier. When the circuit was adjusted for higher gain, +6 db, the amplifier behaved like a stable amplifier only when the input drive level was above some minimum level. Beyond this level, for about a 4 to 5 db range, the amplifier exhibited linear transfer characteristics exactly like those of a stable amplifier. Below this threshold input drive level, the amplifier was extremely nonlinear and sometimes produced spurious output and noise. However, when the input signal was off, the amplifier output also went to zero. This mode of operation was referred to as the triggered oscillator mode and provided these advantages; (1) better gain and efficiency than for stable amplifiers; (2) no bias shutdown and monitoring circuits such as those required for ILO's; (3) low noise and wideband operation; and (4) ease of circuit tuning and good repeatability.

Figure 4.3-1 is a graph of power out versus frequency of a 1.0-watt. IMPATT amplifier operating in the triggered oscillator mode. A bandwidth of about 3 GHz is shown, but the actual -3 db bandwidth may be greater. The rolloff in gain at the higher bandedge is due to the availability of sufficient drive for this high-power output stage.

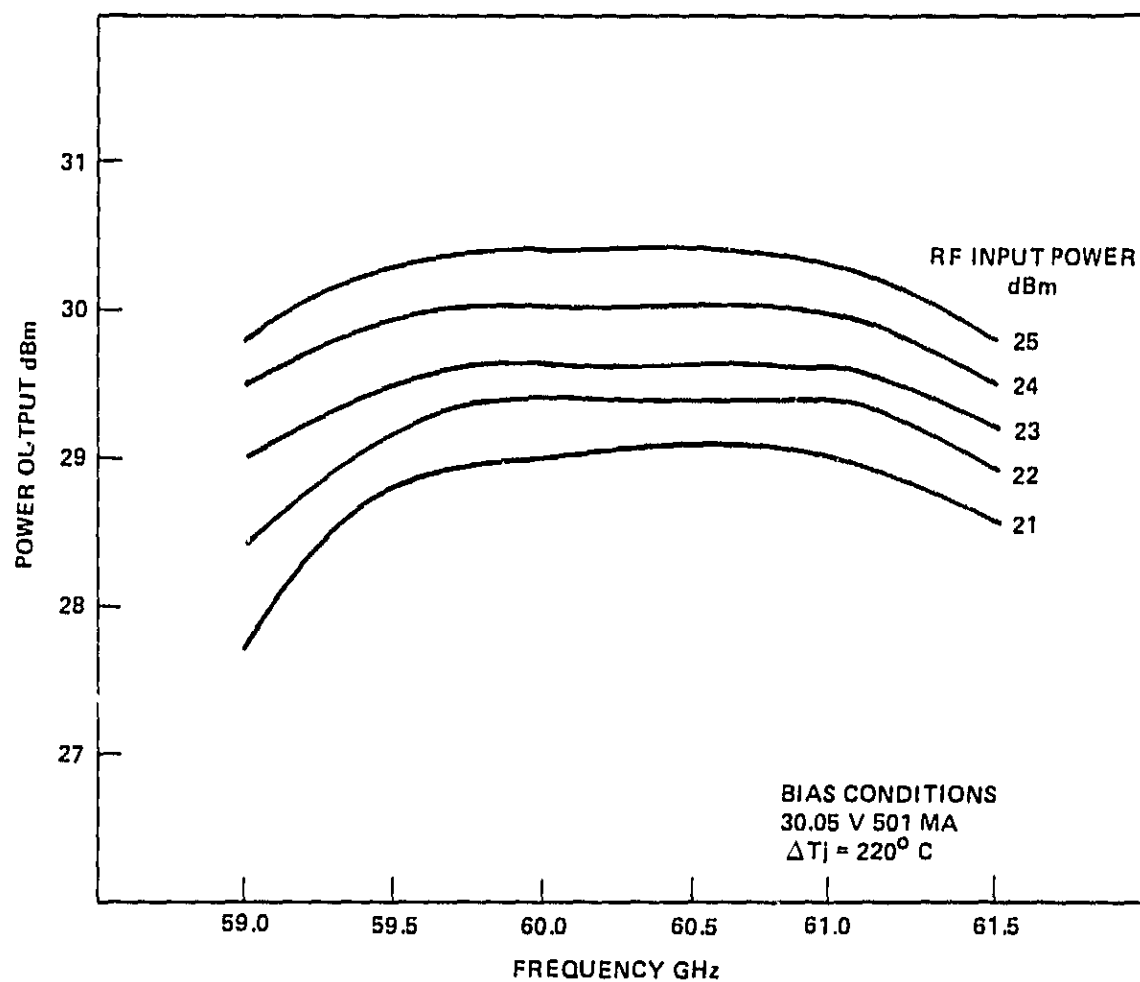


Figure 4.3-1 Output response of a one watt V-band amplifier operating in the triggered oscillator mode.

## 5.0 POWER COMBINER

Module level combining using the 3 db  $90^\circ$  short slot hybrid coupler was proposed originally to combine four single-diode modules at the output stage of the transmitter. As it turned out, the limitation of the short slot hybrid coupler on the bandwidth of the combiner and the favorable performance of the  $180^\circ$  Magic Tees described in Section 3.2 made it clear that the latter approach is decidedly more advantageous.

The  $180^\circ$  or Magic Tee hybrid coupler was therefore studied as a replacement for the  $90^\circ$  short slot. Many manufacturers produce matched Magic Tees, but bandwidths are typically limited to a small percentage of the waveguide band. At Hughes Electron Dynamics Division, matched Magic Tees having nearly full waveguide band performance are produced routinely as commercial products. The unique design of the Hughes Magic Tee employs a special matching element to produce this very wide band operation.

One of these matched hybrid Magic Tees was purchased for evaluation as a power combining circuit. This item as received did not meet the 1:1-to-1 VSWR and 25 db isolation specifications; however, with the aid of dielectric tuning elements we were able to tune the four-port device to meet these specifications.

Our first attempt to power combine two IMPATT amplifier modules was quite successful. The power of the two devices definitely was adding across the entire bandpass with no rolloff on the bandedges marking a noticeable improvement over the short slot hybrids. The combiner, however, was still exhibiting spurious noises.

As it turned out, the problem was due to the fact that the waveguide junction in the Magic Tee was transparent to the external load, which in this case was the ferrite isolator. The output from the combiner was partially reflected by the isolator, causing breakup in the signal across part of the amplifier bandwidth. An attenuator pad was then constructed of 7 feet of V-band waveguide coiled to reduce the VSWR presented to the Magic Tee. As WR-15 waveguide has a loss of 1 db/foot, this pad provided a load for the combiner with greater

than 28 dB return loss and capable of handling high input power. With this waveguide pad at its output, the combiner worked with about 95 percent efficiency over the entire band of interest with no spurious outputs and no need to adjust the amplifier modules. The short slot hybrids were again evaluated using the waveguide pad as a load and the spurious outputs were also reduced. However, the Magic Tee hybrids offered a clearly superior combining structure having better bandwidth and combining efficiency particularly near the band edges. While we were searching for a ferrite isolator with sufficiently low VSWR, the waveguide pad was used temporarily at the output of the power combiner.

A second two-module power combiner based on the Magic Tee was then constructed, with similar results. The two two-module combiners were then further combined to form a four-module combiner, using a third Magic Tee as discussed in Section 3.2. Figure 5.0-1 shows the compact structure of the four-module combiner. The characteristics of the combiner are shown in Figure 5.0-2 in terms of power output across the frequency band of interest. Four nominally 1.0 watt amplifier modules were used in the combiner. Band edge rolloff at the high frequency side is due mainly to insufficient driver power from the transmitter driver chain.

The technique of power combining using the Magic Tees has been developed to where it can be assembled and made to operate reproducibly in the following manner:

Each of the four amplifier modules for the power combiner is assembled and adjusted individually while operating into one of the colinear ports of a single Magic Tee with the opposite port terminated. The modules are individually set for matched operation over the required band. The three magic tees are carefully checked for low return loss on all four ports. If necessary, the matching is improved to achieve a low return loss (typically greater than -26 dB on all parts) and high isolation (greater than 25 dB between combiner parts) across the 59.0 to 61.5 GHz band. The four modules are then assembled as shown in Figure 5.0-1. In general, if the three Magic Tees are well matched, no further tuning of the modules is required.



E4180

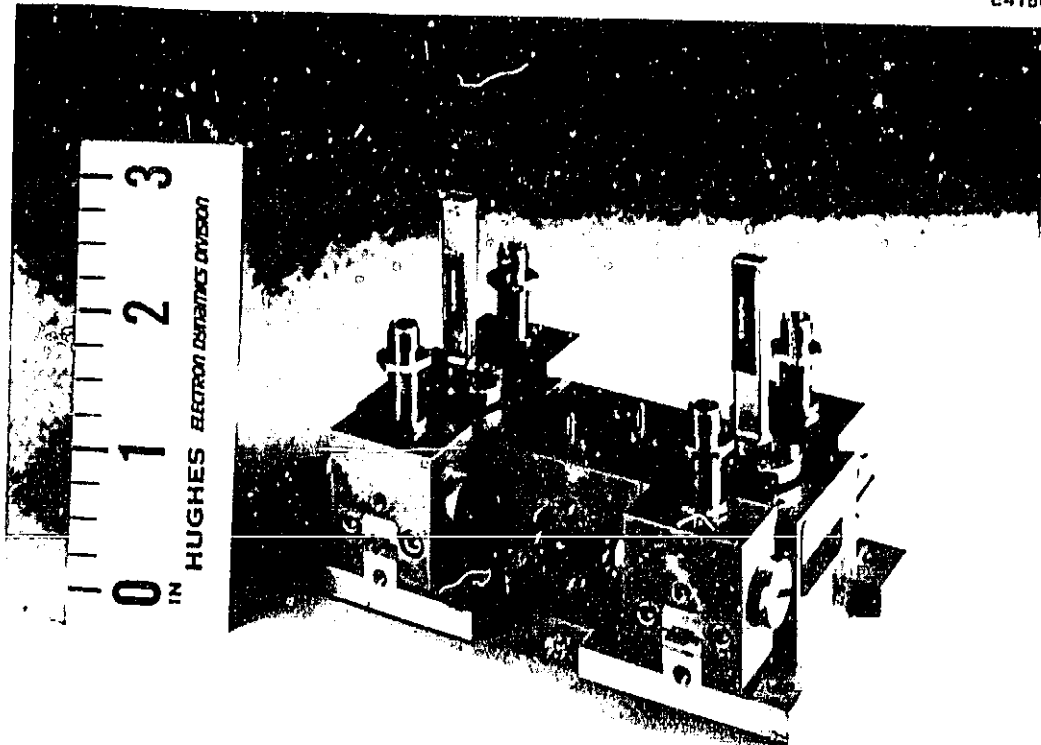


Figure 5.0-1 Assembled V-band four module combiner  
using 3 Magic Tees.

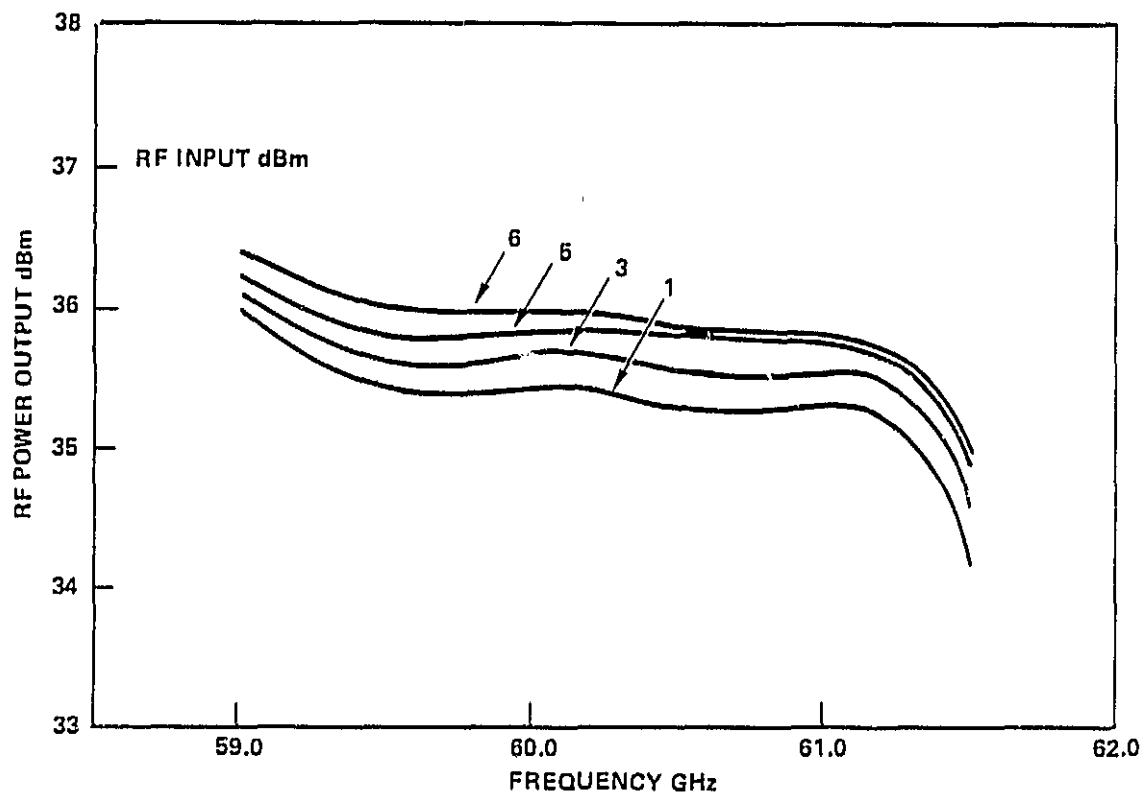
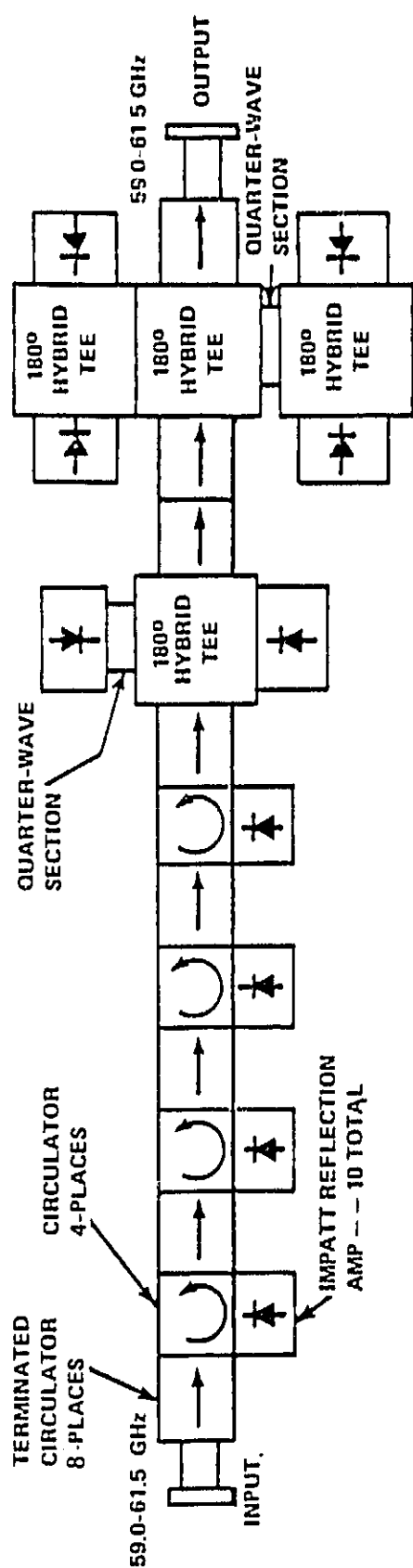


Figure 5.0-2 Four-watt V-band transmitter response.

## 6.0 TRANSMITTER PERFORMANCE

The goal of the transmitter development program was to demonstrate the feasibility and reliability of power combining IMPATT devices for high data rate satellite communications. The task was to develop a 4.0 watt V-band amplifier having 30 dB gain and 2.5 GHz bandwidth (59.0 to 61.5 GHz). Our approach was to develop a 1.0 watt V-band single-diode IMPATT amplifier module using Hughes silicon double-drift IMPATTs and then power combine four of these modules by means of four hybrid couplers for the output stage. Appropriate drivers for the output stage providing adequate drive and gain also were to be developed. This section discusses the development and integration of the transmitter. The actual hardware implementation and approach has deviated from the original proposal somewhat, because of the new development and better combining methods found during the course of the program. Figure 6.0-1 is a block diagram of the final transmitter configuration. It is composed of six stages. The pertinent operating characteristics of each stage are listed. Again, as was pointed out in previous section, a combination of different operating modes was used in each of the amplifier stages. The need for six stages of amplification instead of the originally proposed four stages stems mostly from an input dynamic range consideration. The relatively wide input dynamic range of 4.5 dB makes this transmitter a more practical device than the four stage transmitter with dynamic range of  $\pm 0.25$  dB.

The output power stage was the first developed on this program. The devices operated in the high power stages are Hughes silicon double-drift IMPATTs having 23.5 volts breakdown and approximately 2.0 pF  $C_{jo}$ . When operated at 500 ma bias levels, the devices are capable of nominal 1.0 watt output with a  $\Delta T_j$  of 225°C. Figures 6.0-2 through 6.0-5 show output power versus frequency of each of the four amplifier modules across the band from 59.0 to 61.5 GHz. Figures 6.0-6 and 6.0-7 show the output characteristics of the two-diode combiner modules. These figures show a rather smooth rolloff near the edges of the band, indicative of the wide bandwidth of these amplifier modules and combiners. Figure 6.0-8 is the output response of the four-diode combiner operating into a waveguide pad. The output is a nominal 36.0 dBm, which is the design goal. It should be pointed out that the performance of the single-module and two-module combiners, shown in Figures 6.0-2 through



	STAGE 1	STAGE 2	STAGE 3	STAGE 4	STAGE 5	STAGE 6
RF POWER INPUT (dBm)	6	12	15.5	23.5	28.75	31.5
RF POWER OUTPUT (dBm)	12	15.5	23.5	28.75	31.5	35.4
GAIN (dB)	6	3.5	8.0	5.25	2.75	4.5
NUMBER OF IMPATT DEVICES	1	1	1	1	2	4
DC VOLTAGE PER DEVICE (V)	26.7	28.2	31.0	33.1	31.4	30.5
DC CURRENT PER DEVICE (A)	.150	.182	.353	.375	.485	.490
DC POWER PER DEVICE (W)	4.0	5.1	10.9	12.4	15.2	14.9
TOTAL DC POWER PER STAGE (W)	4.0	5.1	10.9	12.4	30.4	59.8
IMPATT $C_o$ (PF) $V_B$ (V)	1.22 pf 23.5	1.38 pf 23.5	1.52 pf 23.5	1.59 pf 23.5	2.0 pf 23.5	2.0 pf 23.5

TOTAL DC POWER INPUT TO IMPATT DEVICES: 123 W  $\approx$  28% EFF.

Figure 6.0-1 Block diagram of the six-stage V-band solid state transmitter.

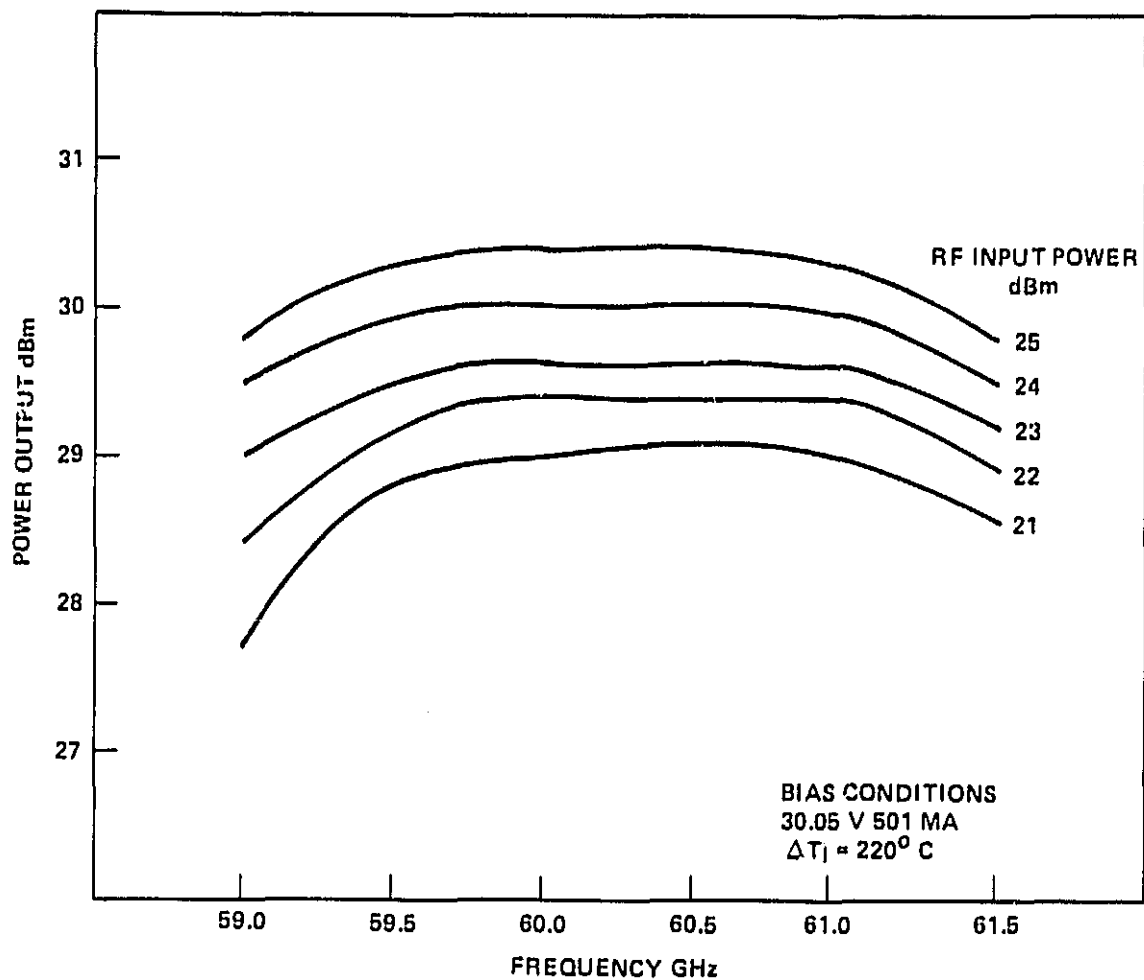


Figure 6.0-2 V-band power combiner amp #1.

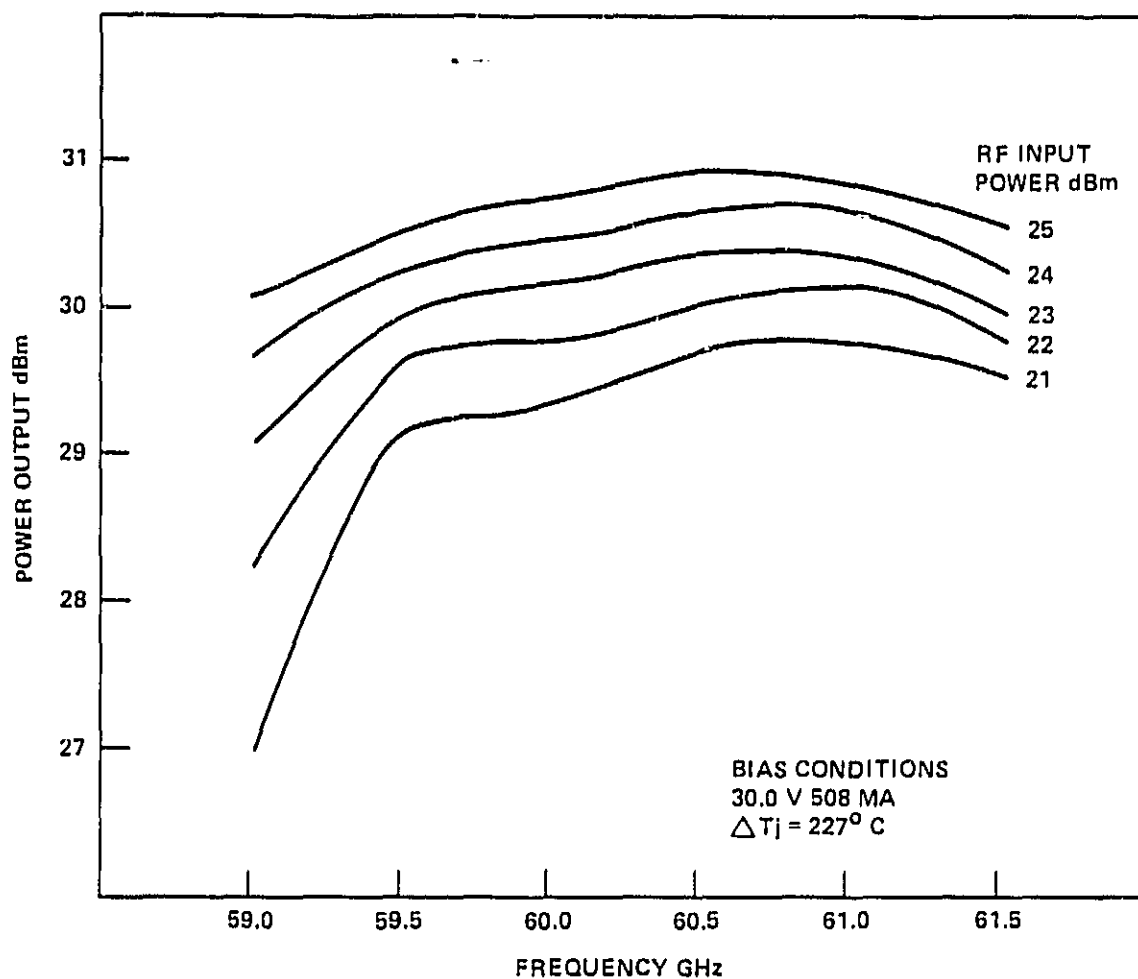
V-BAND POWER COMBINER  
AMPLIFIER #2

Figure 6.0-3 V-band power combiner amplifier #2.

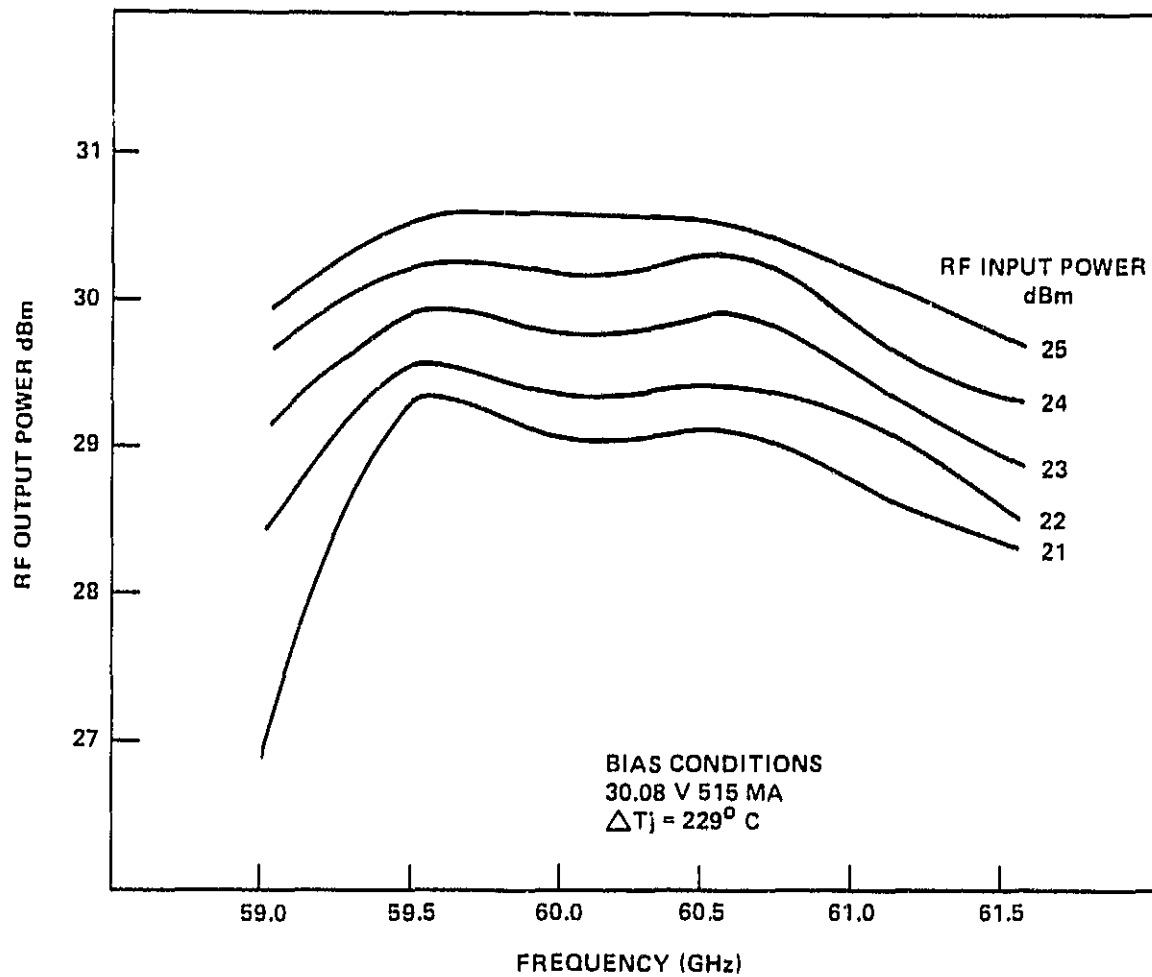


Figure 6.0-4 V-band power combiner amplifier #3.

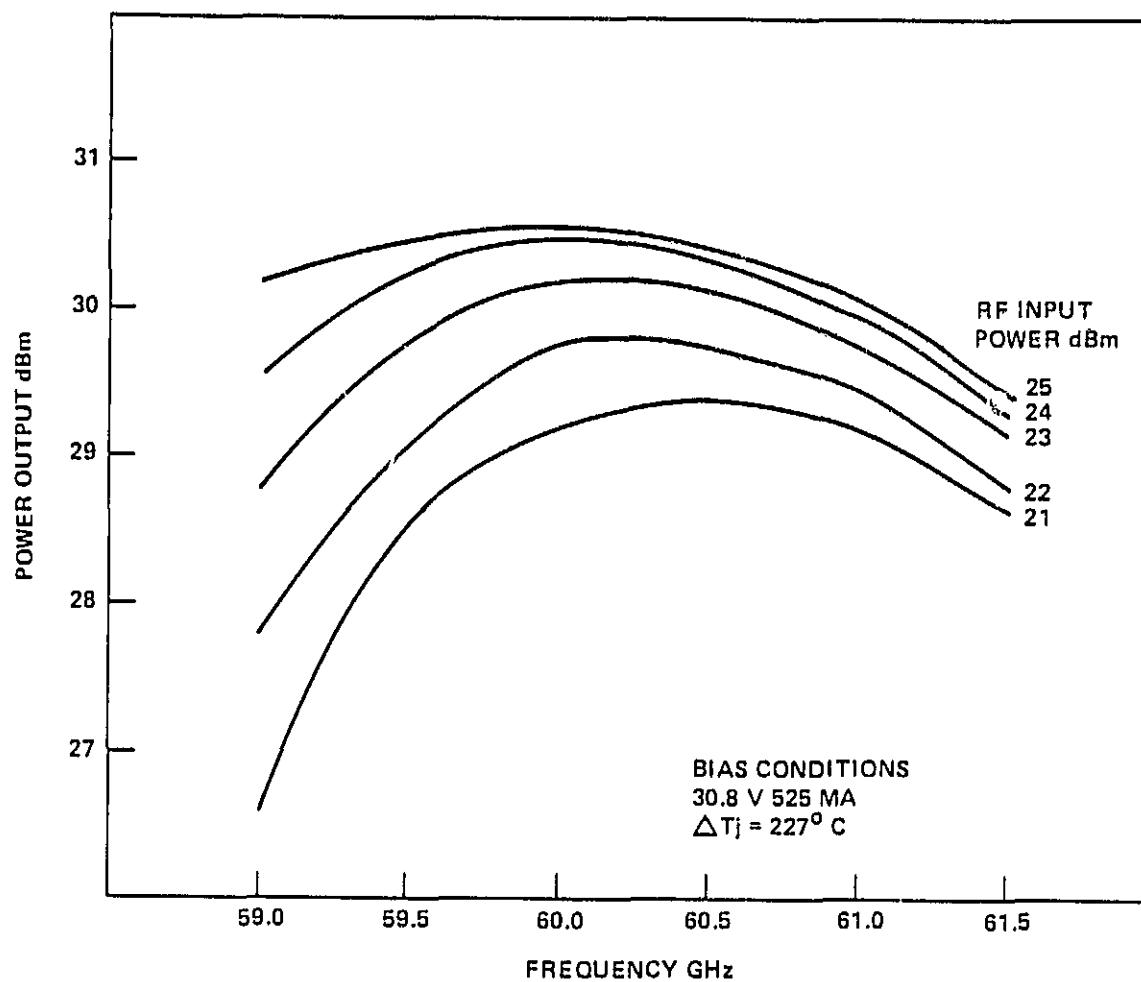


Figure 6.0-5 V-band power combiner amplifier #4.



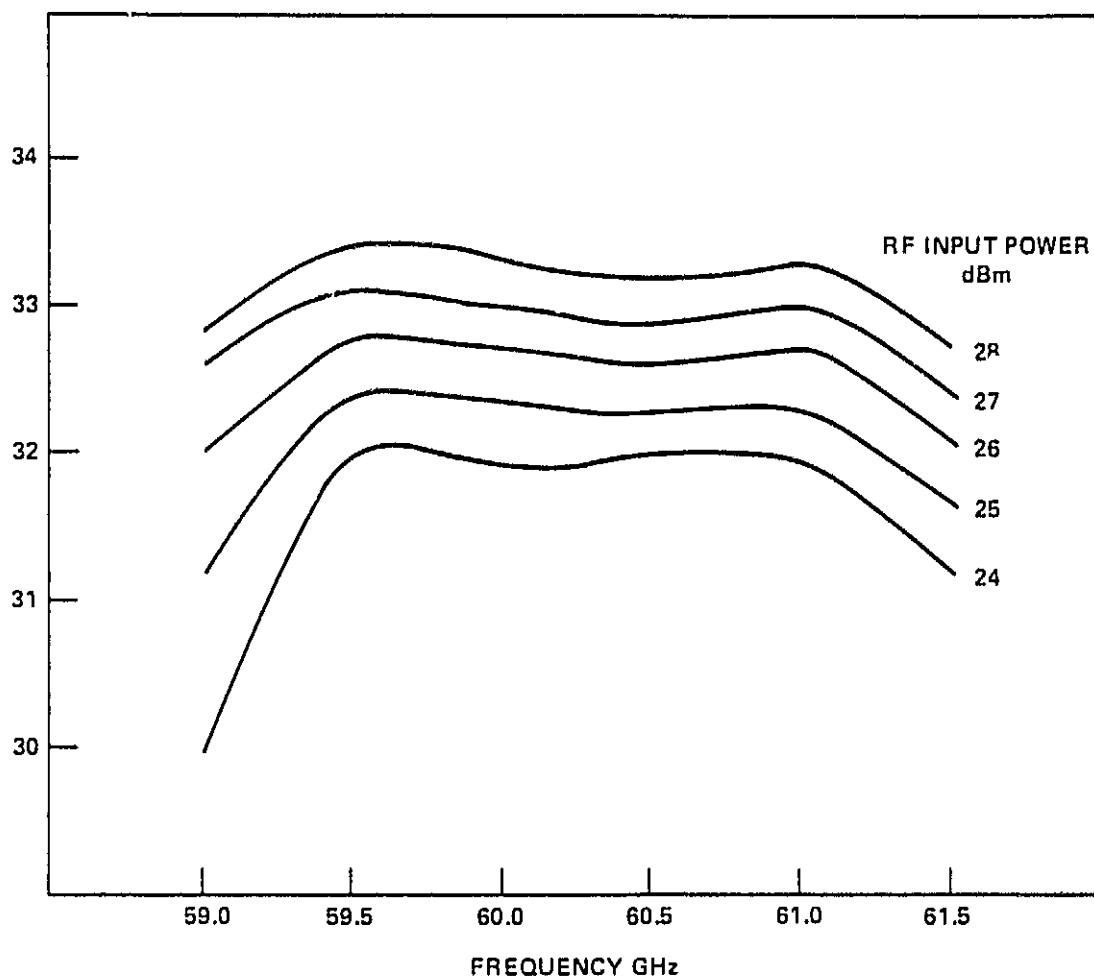


Figure 6.0-6 V-band power combiner amp 1 and 2 two diode module.

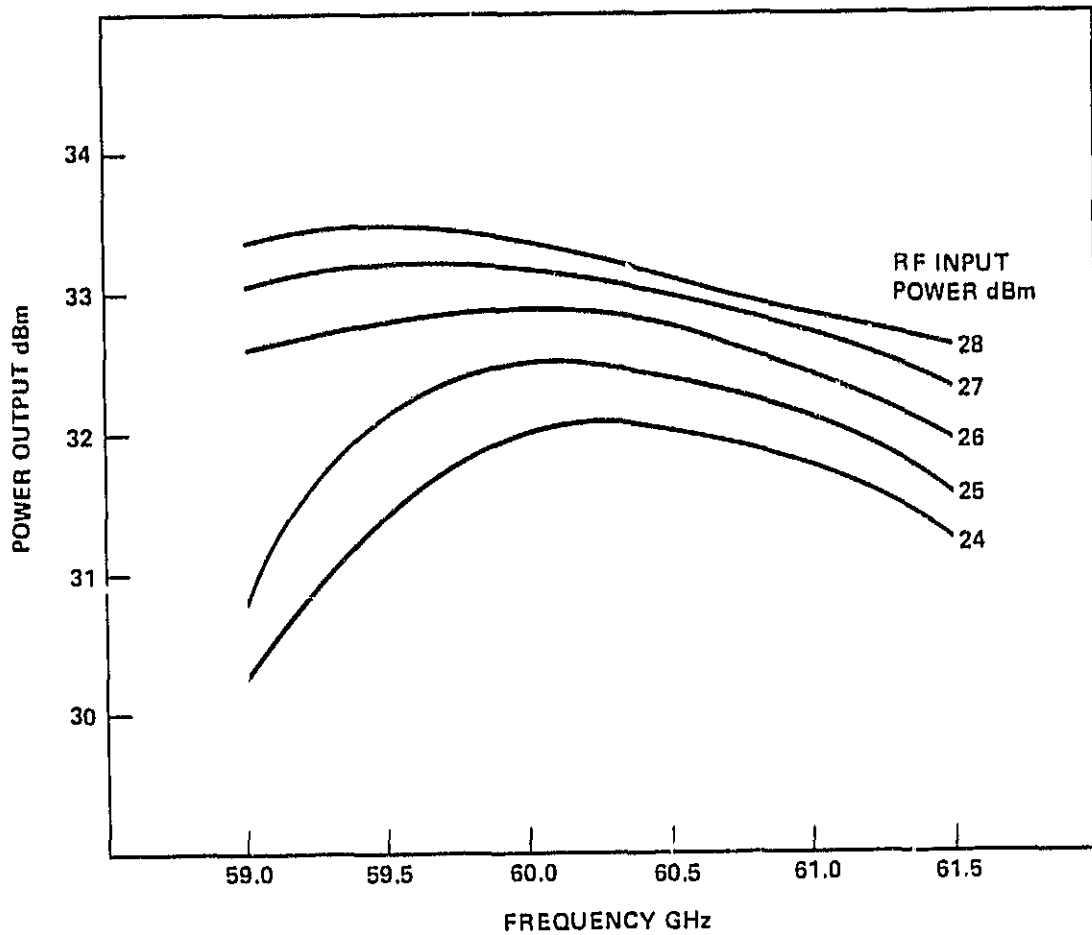


Figure 6.0-7 V-band power combiner amplifier #3 and 4 two diode module.

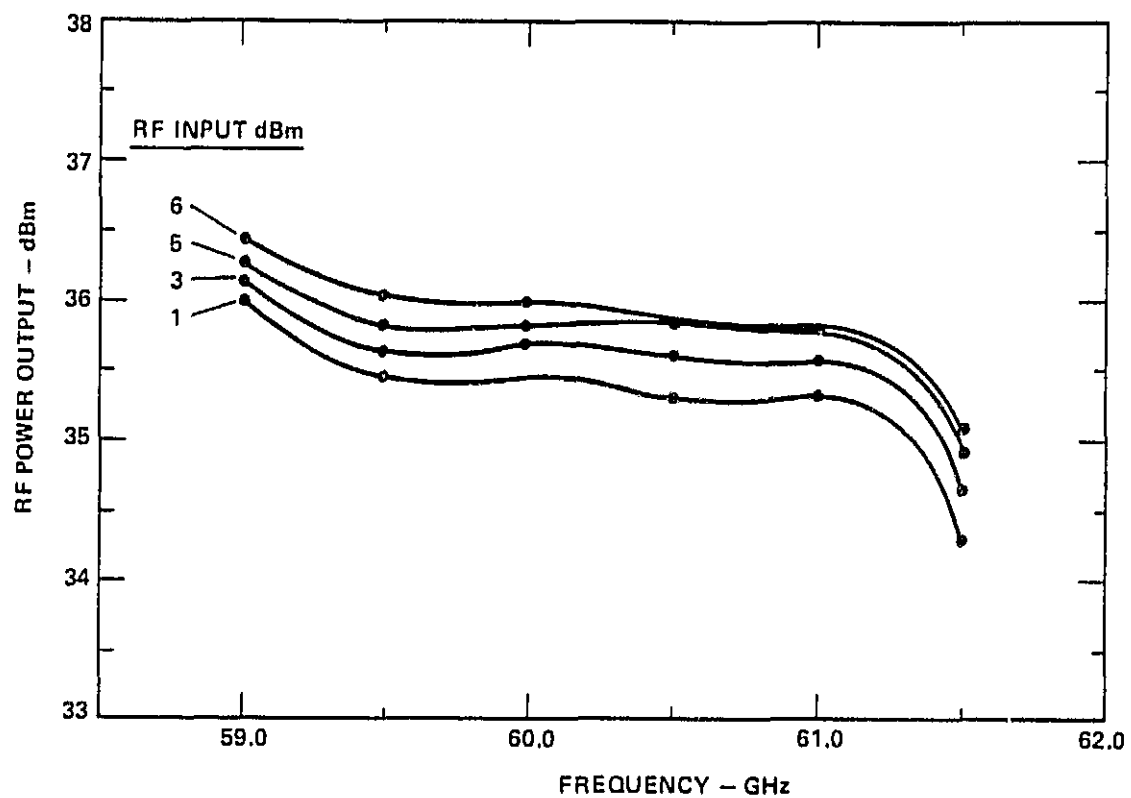


Figure 6.0-8 Four-watt V-band transmitter response.

6.0-5, was from a leveled high power sweeper, while the input drive for the four-module output stage was from the transmitter driver chain, which had a sharp rolloff at 61.2 GHz. The output stage was, in fact, very broadband and had very flat output power over a much broader bandwidth than Figure 6.0-8 indicates. Unfortunately, because of insufficient drive power and the time available to develop another higher power driver chain, the exact 3 dB bandwidth of the amplifier output stage was never determined.

A two-diode power combiner used in the fifth stage was the next hardware to be developed. Figure 6.0-9 shows the output power versus frequency of the two-module combiner used in the fifth stage. The diodes used in the fifth stage were identical to those in the output stage. The circuits, however, were slightly different. To provide more dynamic input range, a slightly higher impedance, reduced-height waveguide circuit was employed. This circuit did indeed provide the wider range of linear operation, but at the expense of diode efficiency. Each of the two amplifier modules produced only 850 mW nominal at 500 mA. This stage was originally tested for 5.0 dB gain but eventually was retuned and driven into gain saturation (~3dB gain), for reasons explained later in this section.

The next stage constructed was the third stage. Figure 6.0-10 is a graph of the output power versus frequency of the single-diode amplifier. To operate at the medium power level, the area of the diode junction is reduced to 1.5 pF. The circuit is otherwise the same as that employed in the output stage. This stage originally was tuned for 9.5 dB gain but was later retuned for gain saturation at 8 dB gain.

The low-power first stage was the next stage to be constructed. This stage uses circuit elements identical to those used in the output stage, but again the junction area of the diode is further reduced (1.2 pF  $C_{jo}$ ) to maintain efficient operation at the lower power levels. Originally tuned for 10 dB gain, this stage had about 3 dB power variation across the band.

When these first four stages were integrated, the transmitter chain produced 34.0 to 35.5 dBm output, with 6 dBm drive. However, the input drive could not be varied by more than  $\pm 0.25$  dB without generating noise at the output.

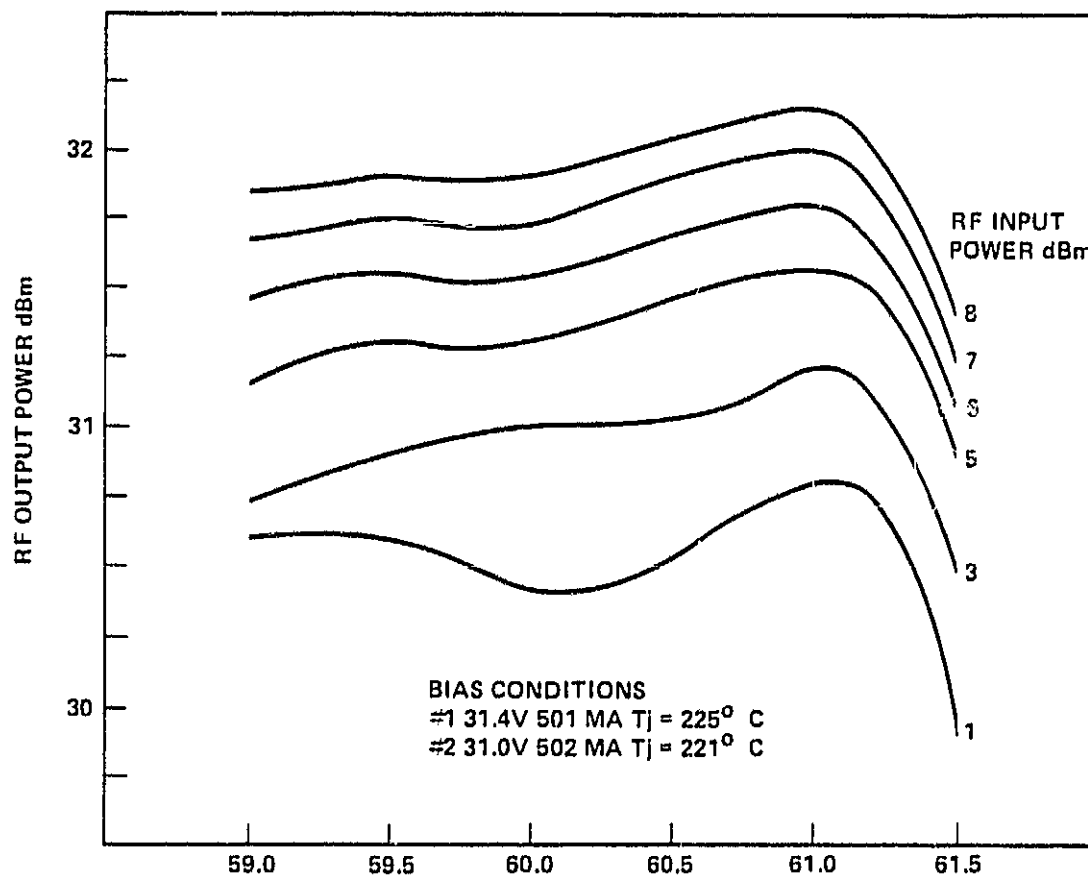


Figure 6.0-9 Driver fifth stage two diode power combiner.

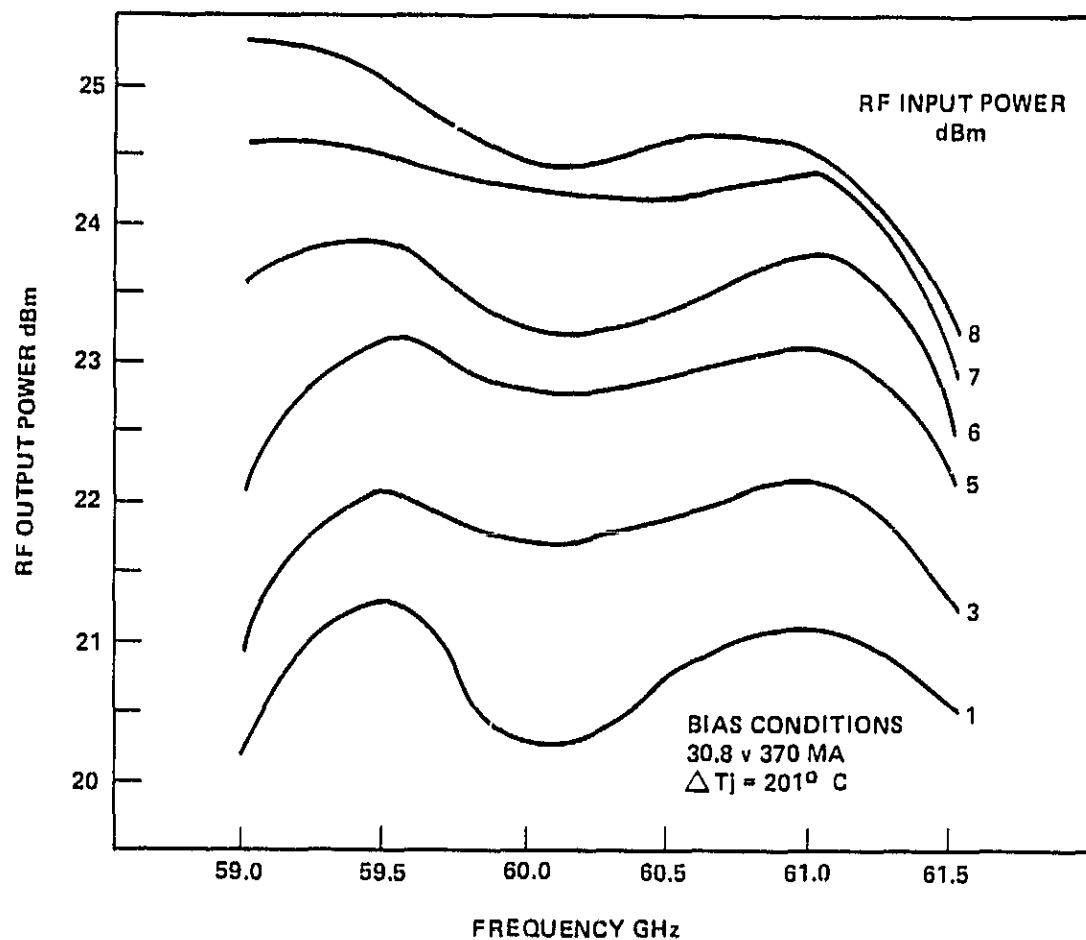


Figure 6.0-10 Driver third stage.

The power variation in the first stage seemed to be the most serious problem. After considerable effort trying to retune this stage, the gain was finally dropped to 7 dB, where the output power variation was reduced to less than  $\pm 0.25$  dB. Another 3 dB gain stage (Stage 2) was added to the driver chain to make up for the reduced gain of the first stage. This relieved some of the restrictions on maintaining a constant leveled input power. Now, input power could be varied from +4.5 dBm to +6 dBm without noise appearing in the output. Figures 6.0-11 and 6.0-12 show a graph of output power versus frequency of the first and second stage. The circuits and diodes in both stages are identical.

To provide even higher dynamic range to the input drive and to raise the output to 36.0 dBm, another medium-power amplifier was added to the transmitter driver chain. This stage became the fourth stage and was tuned for 6 dB gain. The circuit and diode were identical to those in the third stage. Figure 6.0-13 is a graph of output versus frequency of the fourth stage. This added gain allowed us to drop the gain of the third and fifth stage and to operate the third, fourth and fifth stages at gain compression. Operating the amplifier at gain compression results in a much flatter output response and allowed us to vary the input drive from +6 dBm to -3 dBm with a noise-free output. The output power with the transmitter operating into a waveguide pad produced more than 36.0 dBm from 59.0 to 61.2 GHz with 6 dBm drive.

With the transmitter operating with six stages the final task was to procure an output isolator with sufficiently low VSWR and insertion loss so as not to degrade the overall transmitter performance. Our initial attempts were mostly to tune the existing terminated circulators and isolators for minimum insertion loss and return loss. This effort did not eliminate the noise in some parts of the output frequency band. Our early suspicions were that the ferrite devices were overheating and therefore changing their return loss characteristics. By pulsing the transmitter input at low duty cycles, effectively reducing the average power applied to the ferrite, the noise and spurious responses indicated that heating was not the problem. Finally, a relatively low-loss Faraday rotation isolator was selected and laboriously retuned to reduce the in-band return loss to  $>26 \pm 0.25$  dB. Each module

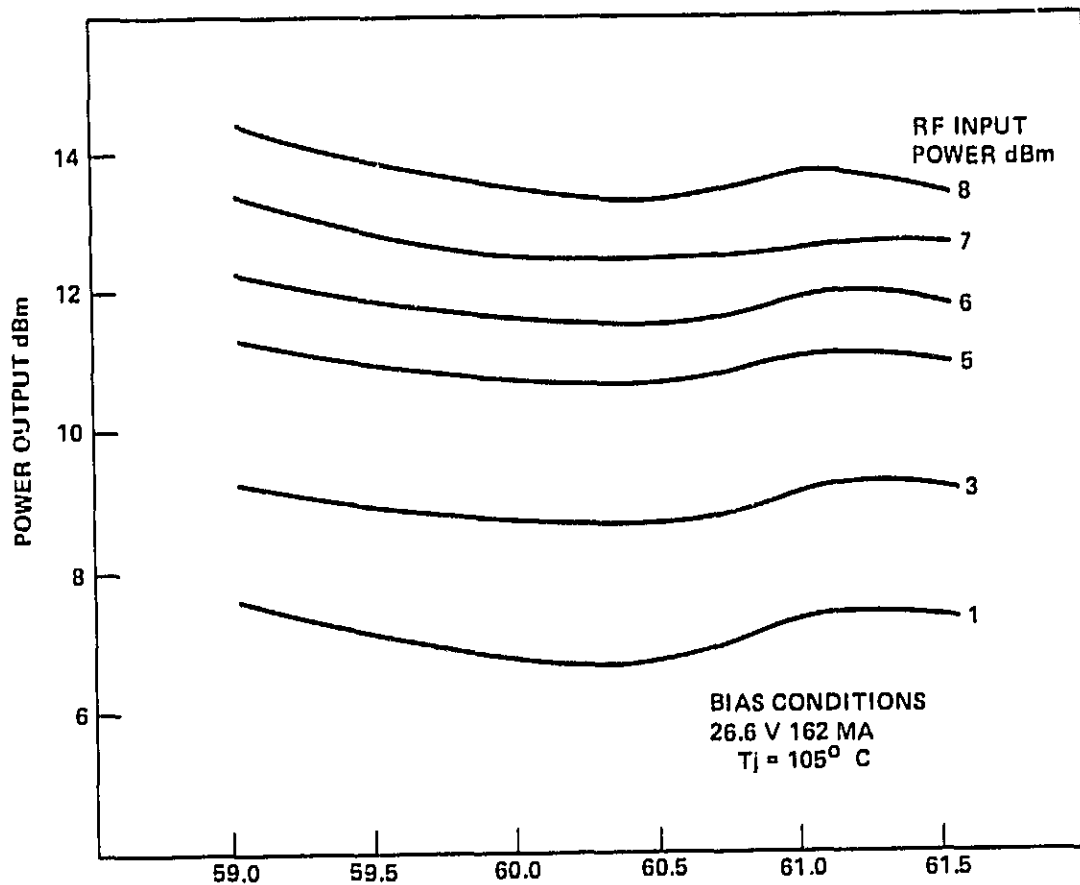


Figure 6.0-11 Driver first stage.



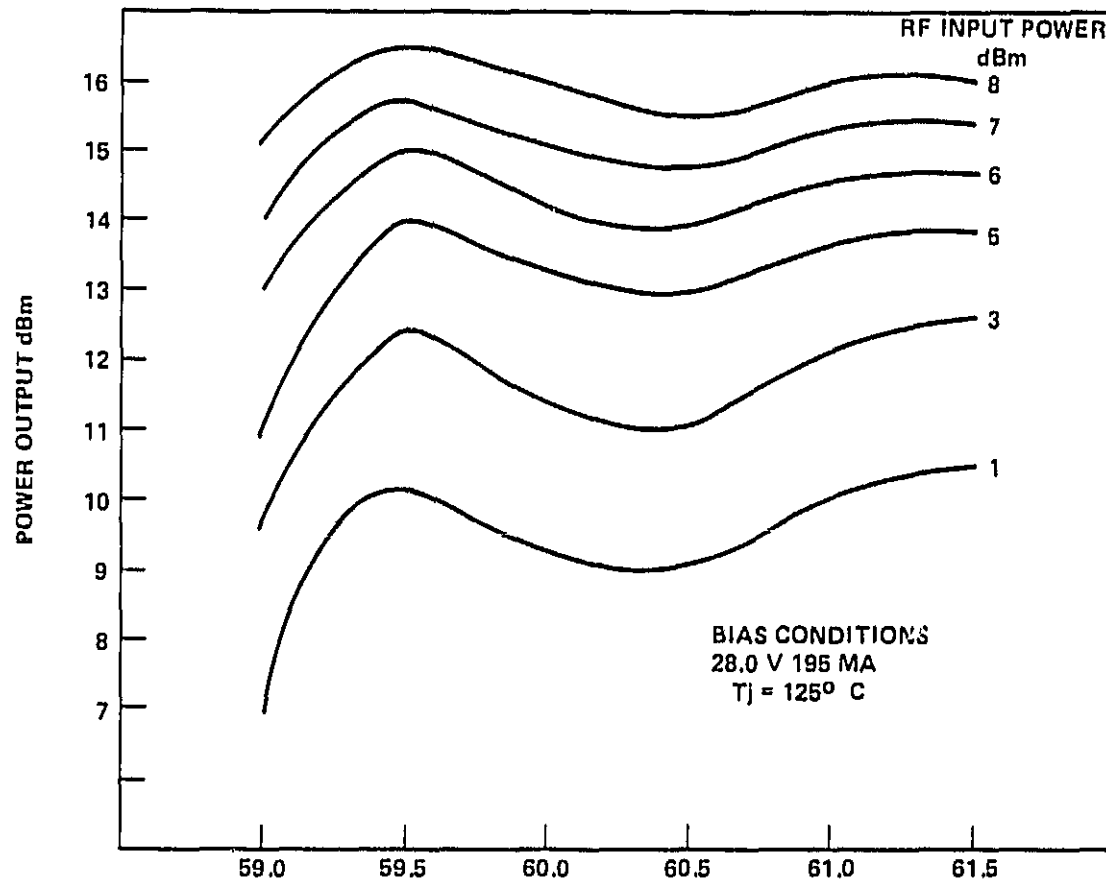


Figure 6.0-12 Driver second stage.

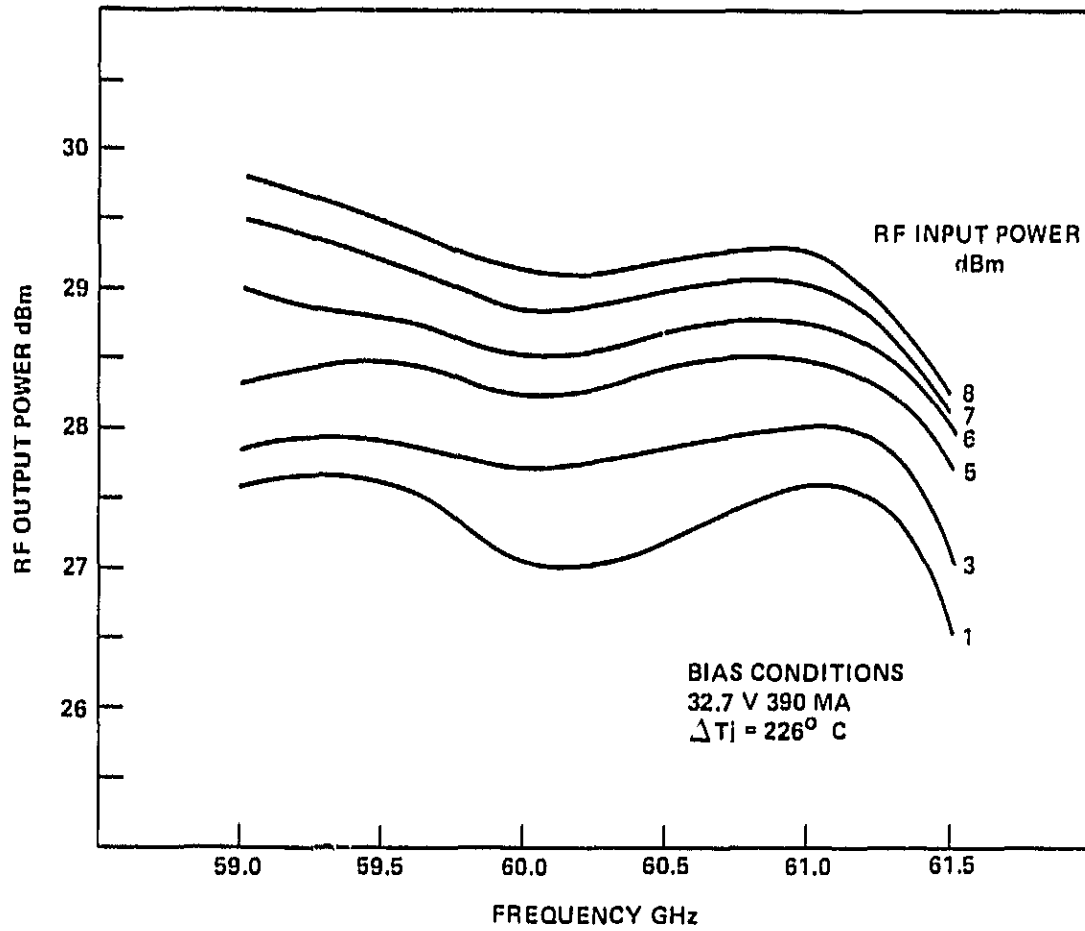


Figure 6.0-13 Driver fourth stage.

of the output stage originally tuned using the waveguide pad as the load were now retuned using the isolator as the load. With this task completed, all four modules were operated simultaneously and successfully. The approximate 0.7 dB loss of the isolator and the retuning of the output stages reduced the final transmitter output to 35.25 dBm with 6 dBm drive. Figure 6.0-14 is a graph of output power versus frequency of the final transmitter. Figure 6.0-15 shows the final transmitter configuration.

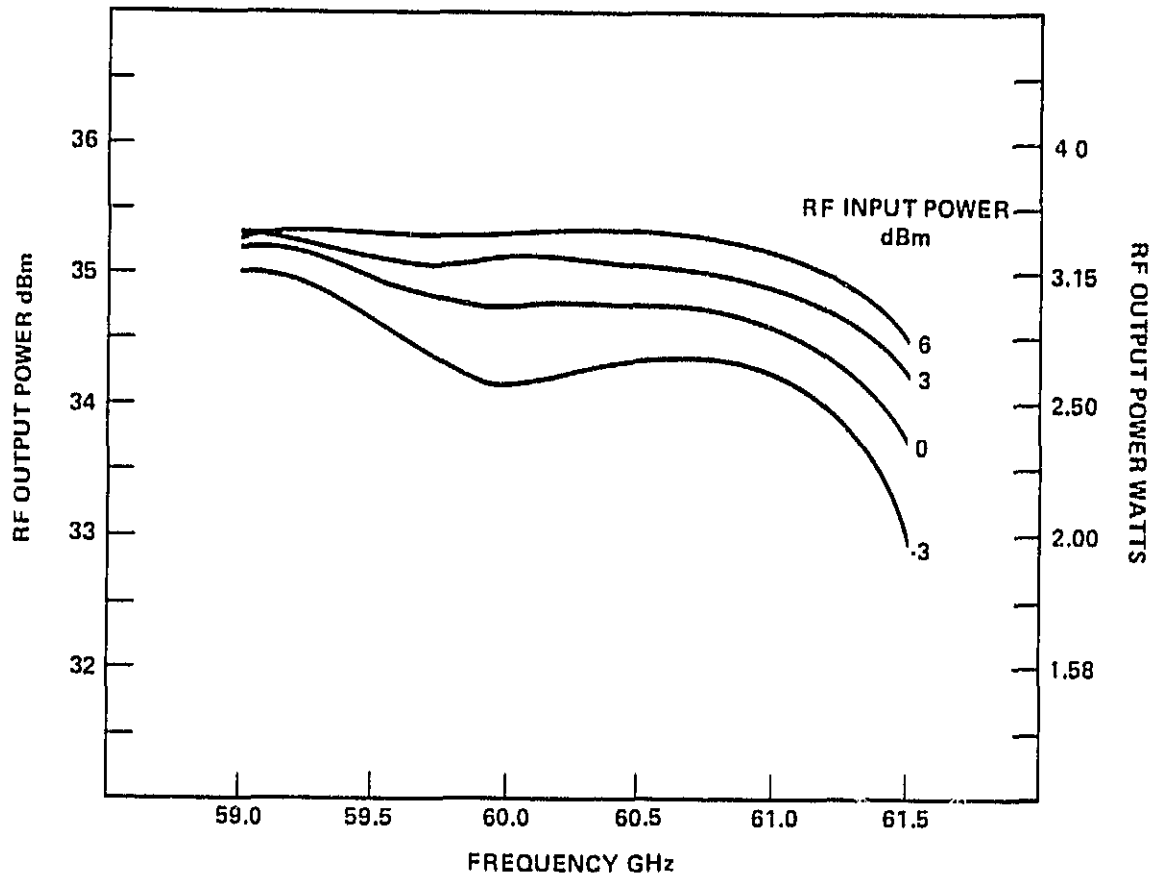


Figure 6.0-14 V-band transmitter output.

E4151

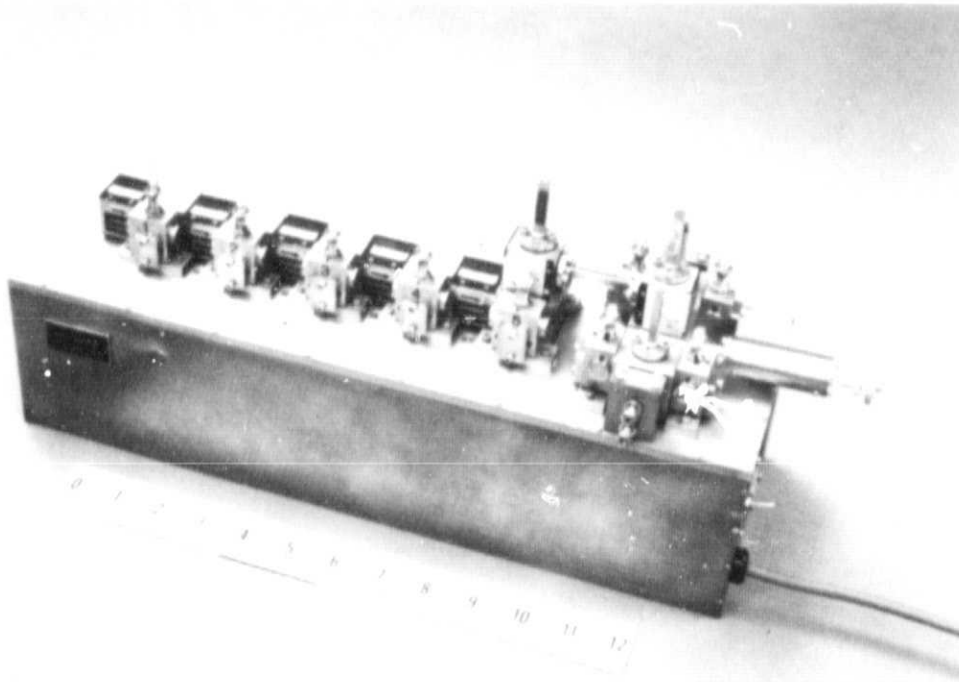


Figure 6.0-15 V-band transmitter with 4 watt output power across a 2.5 GHz band, and 30 dB gain.

## 7.0 STUDY OF CONSTANT-VOLTAGE VERSUS CONSTANT-CURRENT IMPATT BIASING

A sub-task of this program was to study the effects of constant current vs constant voltage biasing methods for IMPATT devices. This study indicates that some basic conclusions may be drawn from our work: The same types of generally advantageous effects are observed for the constant-voltage bias scheme as have been reported in the work by Dahlman on X-band GaAs IMPATT amplifiers. However, these advantages are displayed to lesser degree by far in the case of the 60 GHz silicon IMPATT amplifier. In fact, the extent of the advantage is so small that there is little actual practical advantage to constant-voltage biasing for the 60 GHz silicon IMPATT case. It is believed that the extent of the effects or advantages to constant-voltage biasing over constant-current biasing are largely related to the DC-to-RF conversion efficiency of the device. The reported 8 GHz GaAs IMPATTs have an efficiency of 18 to 20 percent as compared to the 6 to 7 percent efficiency of the 60 GHz silicon IMPATTs. Efficiency is one parameter which relates the degree of coupling between the DC bias conditions and the RF amplitude condition of the IMPATT. Some of the data from the study of the two biasing schemes for a 1-watt nominal, 3 dB gain, V-band, stable amplifier stage employing a silicon double-drift IMPATT on diamond heatsinking is shown in Figures 7.0-1 and 7.0-2.

For the two biasing schemes, the same quiescent (i.e., under no applied RF input power) biasing conditions on the IMPATT were used (31.5 volts, 490 milliamps) and the exact same amplifier is used in the evaluation without any retuning when the bias conditions are shifted. Figure 7.0-1 shows, for conditions of constant-voltage biasing, the bias current versus RF input drive to the amplifier for three different frequencies. There is an approximately 14 percent increase in bias current indicated, compared with 200 to 300 percent reported by Dahlman for GaAs IMPATTs at 8 GHz. Figure 7.0-2 shows gain versus RF power input for three frequencies and for both types of bias conditions. At large signal levels, an increase of about 0.3 dB gain is indicated for the constant-voltage case. Figure 7.0-3 shows the power output versus frequency of the amplifier under constant-current conditions. A maximum output of 1.25 watts at 3 dB gain was achieved with this device.

G11805

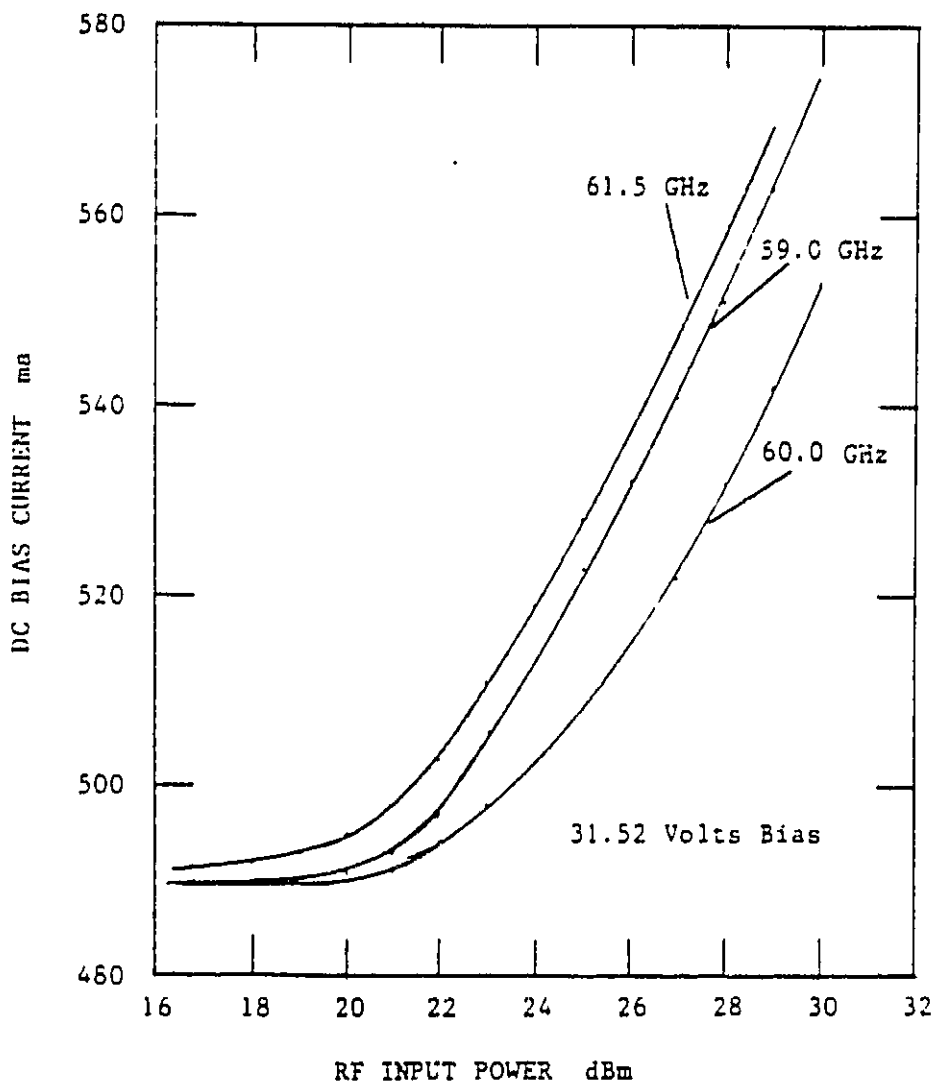


Figure 7.0-1 DC bias current versus RF input drive power for a constant-voltage biased V-band, stable, silicon double drift IMPATT amplifier stage. Nominal large-signal gain of the amplifier is 3 dB.

G11806

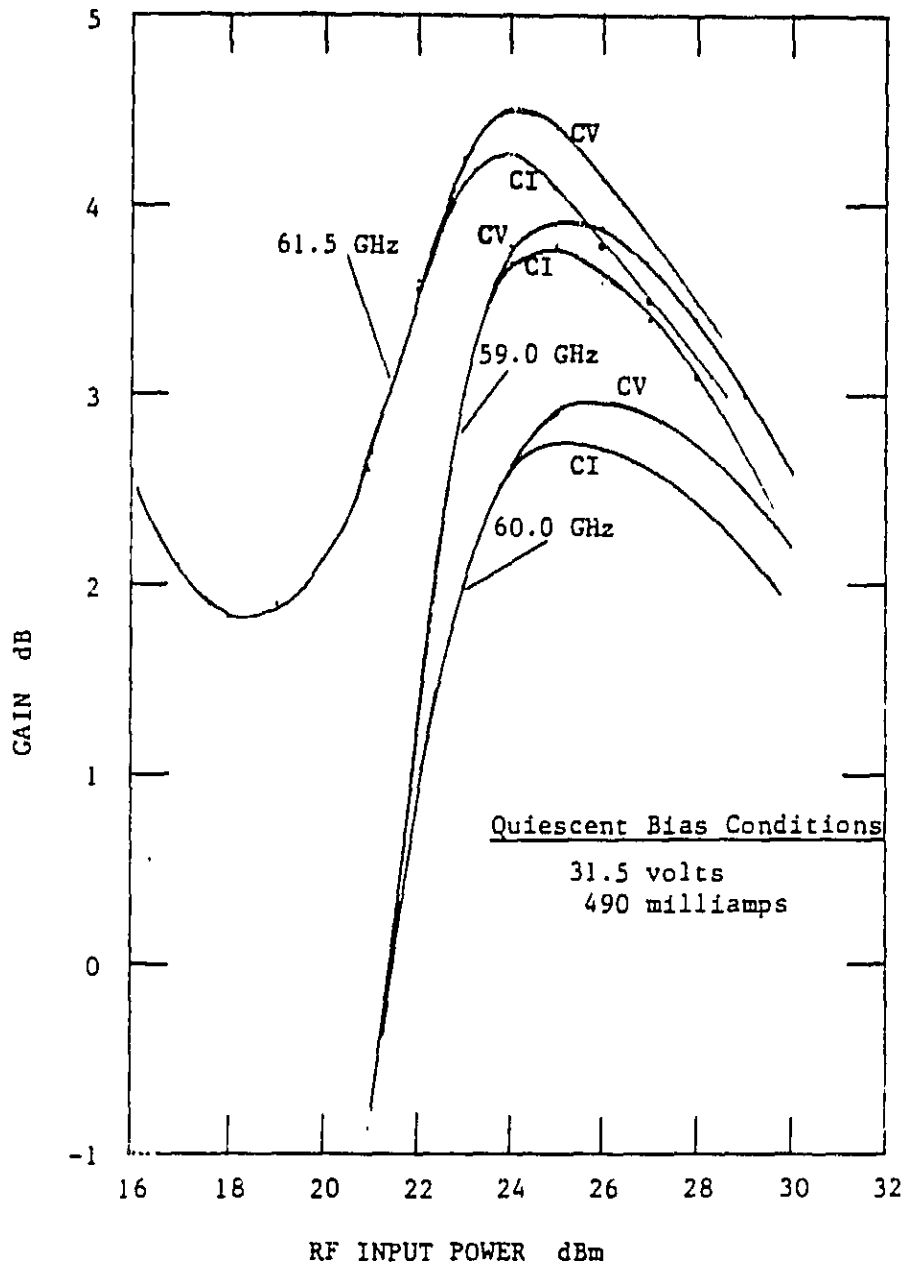


Figure 7.0-2 Gain versus RF input drive power for three frequencies and for both constant-voltage (CV) and constant-current (CI) conditions of biasing for a V-band, stable, silicon double-drift IMPATT amplifier stage.



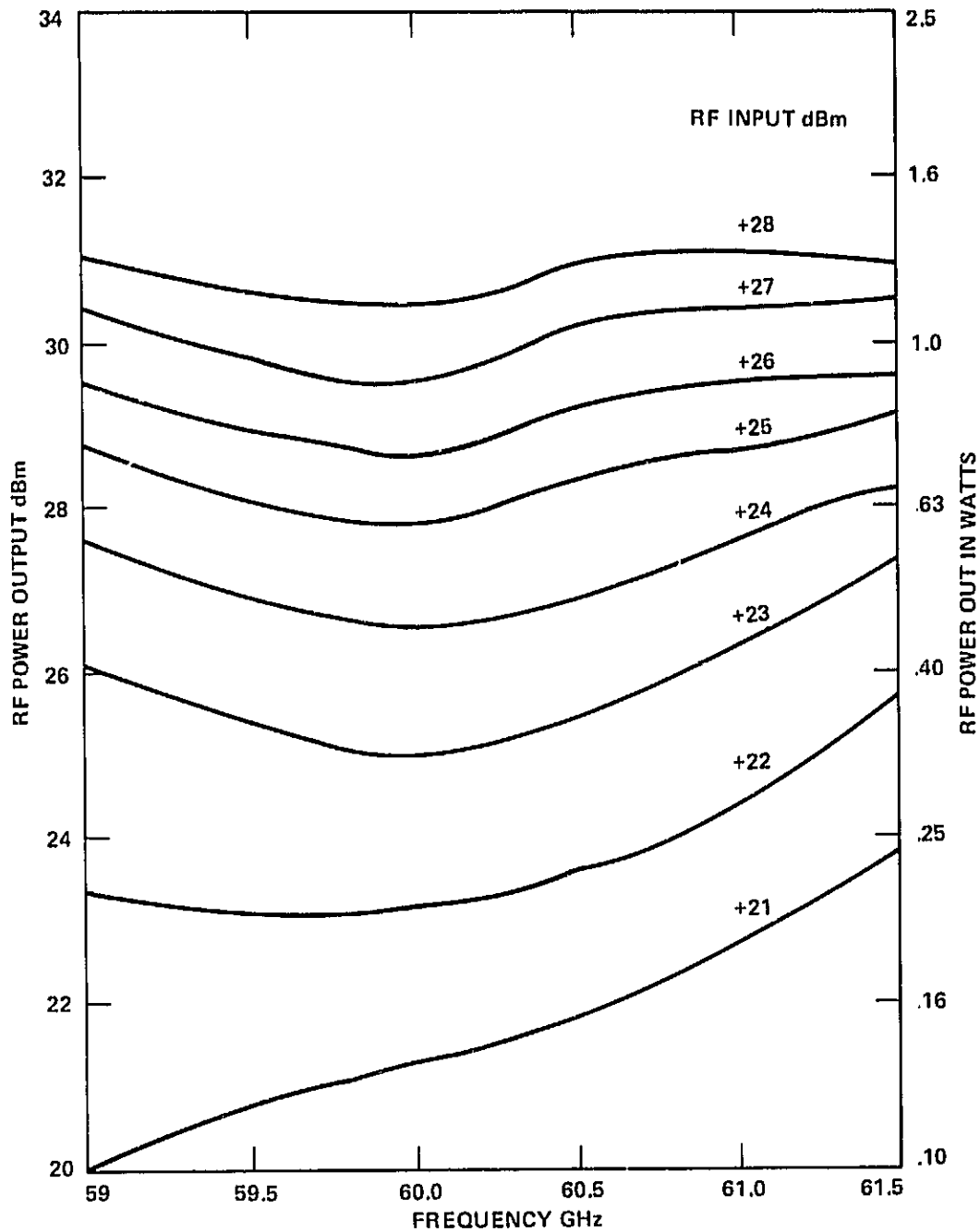


Figure 7.0-3 RF output power versus frequency  $F_o$  -constant current 1 watt V-band stable amplifier.

Any attempt to drive the amplifier with higher input levels resulted in noisy output.

Figure 7.0-4 shows the same amplifier output versus frequency under constant-voltage bias conditions. A maximum output of 1.6 watts at 3 dB gain was achieved with a 30°C added junction temperature rise ( $\Delta T = 242^{\circ}\text{C}$ ). This added rise in junction temperature is due to the inherent tendency of the constant-voltage amplifier to demand more bias current with increasing drive levels. Figure 7.0-5 is a photograph of the amplifier and dual bias source.

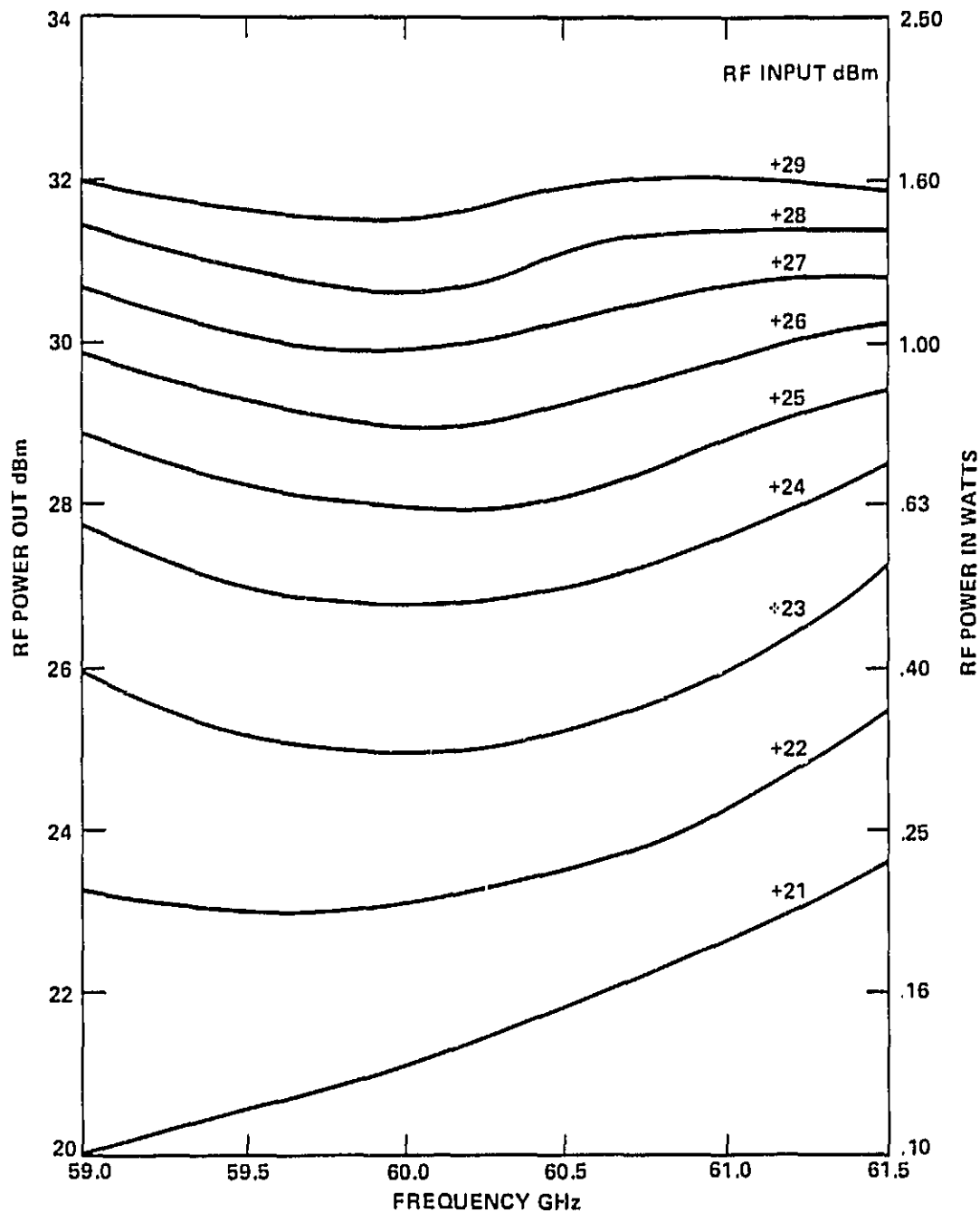


Figure 7.0-4 Power output versus frequency for constant voltage 1 watt stable V-band amplifier.

E4152

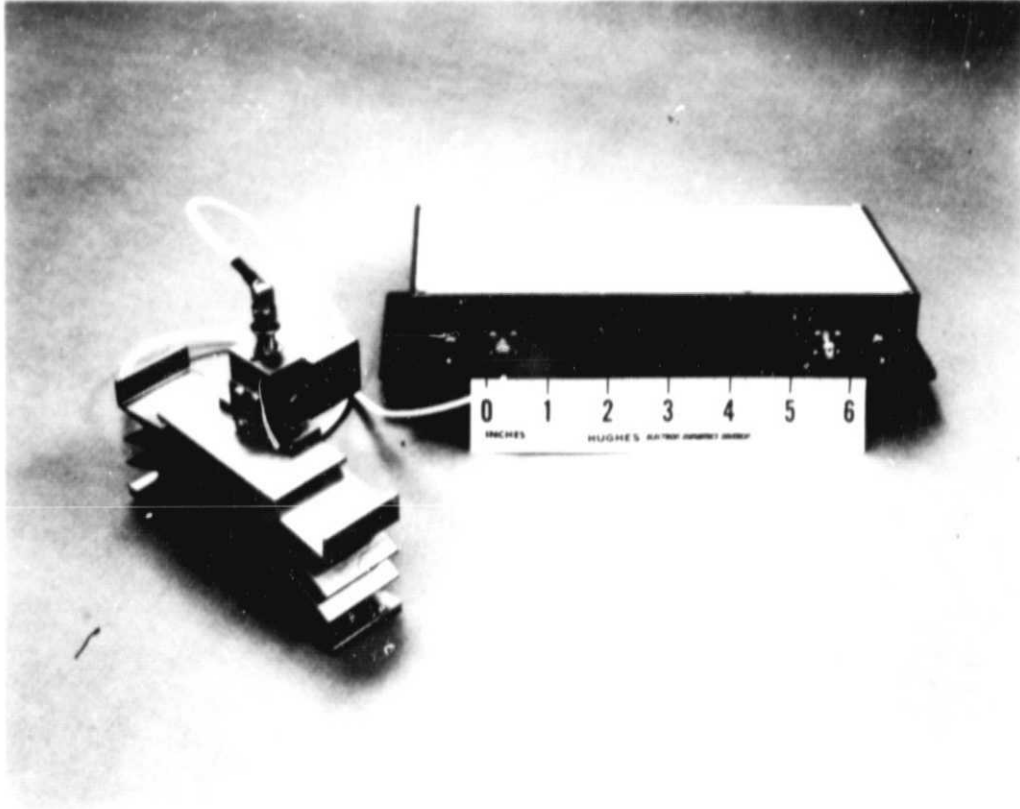
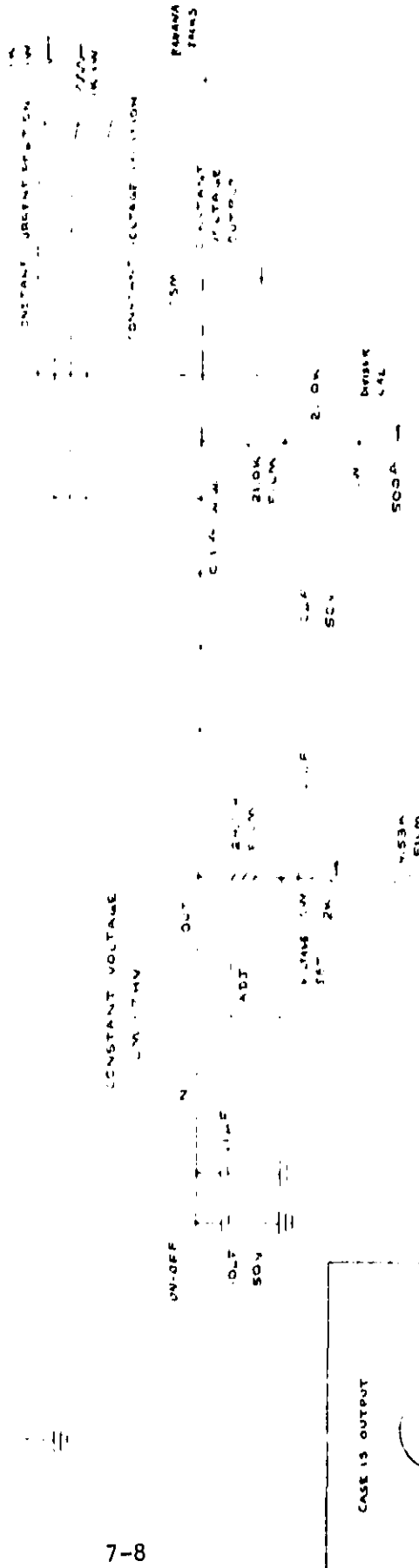


Figure 7.0-5 A high power ( $>1$  watt) stable IMPATT amplifier capable of operating in either the constant-voltage or constant-current mode by switching the bias supply into either states.

[illegible]

## 8.0 SUMMARY AND RECOMMENDATIONS

### 8.1 SUMMARY

A high-power broadband transmitter has been developed at V-band for future communication requirements. This transmitter consists of six stages of IMPATT amplifiers utilizing state-of-the-art double-drift silicon IMPATT diodes. The output high-power stages required power combining two and four of the high-power single diode modules. Both injection locked and stable amplifier modes of operation were investigated. A new mode, the triggered oscillation mode, was discovered during the course of the program. This mode has some unique features that make it extremely attractive for high-power broadband applications. Other significant achievement on the program include:

1. Development of a 1.0 watt stable amplifier with greater than 2.5 GHz bandwidth. This marks the first time a high-power broadband stable IMPATT amplifier was ever been demonstrated utilizing double-drift IMPATT diodes.
2. Demonstration of a 1.0-watt, 2.5 GHz bandwidth amplifier operating in an injection locking mode. This is the first time that such wide bandwidth was ever achieved with injection locked oscillators having a gain greater than 10 db.
3. Combining of four of the IMPATT modules using a compact high-performance Magic Tee hybrid coupler approach. More than 4 watts of output power were achieved over a 2.5 GHz bandwidth with a combining efficiency greater than 90 percent.
4. A theoretical analysis that defines the required performance of the circulators and hybrid couplers used in the reflection amplifiers. No such analysis was performed prior to this program, and the data was obtained in the past by empirical means at best.
5. A study and experimental comparison of the IMPATT reflection amplifier operating under constant voltage and constant current conditions.

The results of this effort semi-qualitatively verifies the slight advantage of constant-voltage over constant-current operation for silicon IMPATT diodes.

6. Development of a ten-channel regulator/power supply. Each channel has its own protection circuit against overvoltage, shorted load and line oscillations. Circuits also were provided to detect failure and monitor operating conditions of each amplifier.

At the end of the program, a transmitter meeting program goals, together with a 10-channel power supply was delivered to the NASA Goddard Space Flight Center. The transmitter provides nominally 4.0 watts output power over a 2.5 GHz bandwidth and has a gain of 30 db. A single-diode stable IMPATT amplifier capable of operating either in the constant-voltage or the constant-current mode also was delivered.

## 8.2 RECOMMENDED FUTURE WORK

During the course of the amplifier development, several problems were encountered. Though solutions were found that allowed us to proceed with and complete the program successfully, some of the problems are more basic in nature. Because of the limited duration of this program, a more detailed study of these problems was not possible. However, we believe that the successful resolution of these basic problems not only will benefit future amplifier programs but will advance the technology of reflection amplifiers as a whole. We recommend the following future tasks:

1. Circulator/Isolator - Much of the effort on the transmitter program focused on the tuning and selection of a suitable circulator for use in the reflection amplifiers and in the input/output port of the high-power combiner. The difficulty, as was explained in Section 3.2 of this report, is the requirements on the low return and insertion losses over a broad bandwidth. Commercial circulators and terminated circulators of the turnstile type typically have return losses of -20 db or higher and insertion losses of 0.5 db or higher over a 3 GHz bandwidth. Isolators of the Faraday rotation type

have a broader band, but the insertion loss is typically greater than 2 db. There is an urgent need for a reproducible low insertion loss ( $\sim 0.25$  dB), low return loss ( $\sim -25$  dB) broadband ( $\sim 10\%$  BW) circulator/isolator for use with the IMPATT amplifiers. The analysis in Section 3.2 defines this requirement.

2. Injection Locked Amplifier - The amplifiers developed on this program are either the stable or the triggered oscillator mode. For stable amplifiers, the gain is inherently low under large signal conditions. As injection locked oscillators have much higher gain than stable amplifiers, fewer stages are required to achieve the required gain. For a specific application such as the communication system considered here, injection locked oscillators will be the ideal solution.

Injection locked oscillators have been developed under the present program. A bandwidth greater than 2.5 GHz has been achieved from a single-diode oscillator with output power exceeding 1.0 watt and a gain greater than 10 dB, compared to the 3 dB gain from stable amplifiers. Reproducibility of the ILO, however, presents a major problem that prevented its being used in the transmitter program. The difficulty is mostly in the circulators which presented a high return loss to the oscillator and caused spurious oscillator noise and breakup in the band. With the development of the circulator defined in Task 1, the ILOs should be investigated further for this specific application.

3. Characterization of the Triggered Oscillator - The advantages of the triggered oscillator were described in Section 4.3. This is a new mode of operation, for which only a small amount of data exists, other than what was derived from this program. To explore the full capability of the triggered oscillator, the device needs to be characterized fully in terms of criteria of operation, transfer characteristics, noise and gain.
4. High Efficiency IMPATT Diodes - The diodes used on this program are silicon double-drift flat-profile IMPATT diodes. The efficiency



of these diodes is typically 5 to 7 percent. For high-power transmitters, the low diode efficiency translates into large prime power requirement and heat-removal problems. High-efficiency devices need to be developed. The candidate for high efficiency, high-power solid state sources are GaAs and Silicon Read IMPATT diodes. These two devices are being developed under several DOD and NASA sponsored programs at various laboratories, but the work needs to be expanded.

5. FET Amplifiers - For low-power stages, small-area IMPATT diodes have to be used. Below a certain input power level (e.g.. -10 dBm), the fabrication of a small IMPATT diode and the tuning of a broadband low-power amplifier become increasing difficult. A logical candidate to fill this need is the GaAs field effect transistor amplifier. Hughes is developing millimeter-wave FET amplifiers under an IR&D project. Preliminary results include a three-stage FET amplifier with gain greater than 10 dB covering greater than 4 GHz bandwidth. Further development of the millimeter-wave FET amplifiers and their integration with the high-power IMPATT amplifier should provide a practical transmitter of reduced size, lower noise figure and improved performance.